Digitized Theses

Digitized Special Collections

2009

Investigation, design, and integration of insert gradient coils in magnetic resonance imaging

Rebecca E. Feldman

Investigation, design, and integration of insert gradient coils in magnetic resonance imaging

(Spine title: Consideration of insert gradient coils in MRI)
(Thesis format: Integrated article)

by

Rebecca E. <u>Feldman</u>

Graduate Program in
Medical Biophysics

Submitted in partial fulfillment
of the requirements for the degree of
Doctor of Philosophy

School of Graduate and Postdoctoral Studies
The University of Western Ontario
London, Ontario, Canada

October 2009

THE UNIVERSITY OF WESTERN ONTARIO
SCHOOL OF GRADUATE AND POSTDOCTORAL STUDIES

CERTIFICATE OF EXAMINATION

Supervisor

Examiners

_____

_____
Brian Corneil, PhD

Advisory Committee

_____
Maria Drangova, PhD

_____

_____
Nicola de Zanche, PhD

_____

_____
Martin Zinke-Allmang, PhD

The thesis by

Rebecca E. Feldman

entitled

Investigation, design, and integration of insert gradient coils in magnetic resonance imaging

is accepted in partial fulfillment of the
requirements for the degree of
Doctor of Philosophy

Date _____

_____
Chair of Thesis Examination Board

ii

Abstract

Diffusion-weighted magnetic resonance imaging utilizes the magnetic gradients of the system to de-phase protons undergoing diffusion with respect to the overall magnetization. Areas of the image with reduced signal when compared to an un-weighted image represent where protons have undergone diffusion. The stronger the gradient applied during diffusion-weighting, the larger the signal loss due to diffusion, and the larger the b-value differentiating the diffusion coefficients. However, the maximum gradient strength during image acquisition is limited by both the original strength of the signal and peripheral nerve stimulation.

Nerve stimulation is induced because the changing magnetic fields of the gradient pulse sequence induce electric fields that cause stimulation. The stimulation threshold can be measured either in terms of the pulse sequence parameters of maximum gradient strength and slew rate, or in terms of the induced electric field and the duration of the electric field pulse.

A finite-difference simulation was used to approximate the electric field induced inside a visible man model. The effect of varying the size, resolution, and position of the model inside the simulation was investigated with the wire pattern from a customized head/neck gradient coil. For accurate simulations, it was most important to ensure that the resolution of the model was sufficient to capture the air cavities of the sinus and trachea.

The peripheral nerve stimulation thresholds of a planar gradient coil were determined from human experiments. While the electrical stimulation threshold parameters did not vary significantly from previous studies, the minimum gradient change and slew rate required to cause stimulation were significantly higher for the planar gradient than for reported thresholds of cylindrically designed gradient systems.

Several non-cylindrical localized gradient designs were investigated for diffusion-weighted contrast as a fourth gradient, in addition to the three imaging axes. Both resistive and inductive merits were investigated. Of these, inductive values proved to be the limiting factor when designing coils sized to perform in a full body MRI system. Optimal merit and gradient strength were obtained from a butterfly design, and planar coils provided localized strength over a larger region.

A butterfly coil was constructed with hollow copper wiring and powered to produce diffusion weighting during MRI. Diffusion contrast b=1300 s/mm^2 was obtained using the insert with significant time and signal to noise ratio improvements.

Keywords: butterfly coil, magnetic resonance imaging, electric field, gradient coil, inductive merit, nerve stimulation threshold, optimization, peripheral nerve stimulation, planar gradient, resistive merit, scalar potential, simulation, stimulation, vector potential, optimization.

Co-Authorshp

This thesis contains material from the manuscript: Feldman RE, Hardy CJ, Aksel B, Schenck J, Chronik BA. Experimental determination of human peripheral nerve stimulation thresholds in a 3-axis planar gradient system. 2009 *Magn. Reson. Med.*, 62(3):763-770, 2009. The manuscript was reproduced in Chapter 3 and was written by Rebecca Feldman. All theoretical modeling, computer simulations, coil construction and design, data acquisition an analysis, and imaging was performed by Rebecca Feldman with the exception of the tasks listed in the following paragraph.

William Handler provided some of the libraries and functionality used in the implementation of the electric field simulations in Chapter 2. Chris Hardy and Bulent Aksel, from GE, facilitated the peripheral nerve stimulation experiments from Chapter 3. They designed and built the planar gradient system used in the nerve stimulation experiments. Josh De Bever provided valuable advice and strategies regarding the development and structure of the software used for the gradient coil optimization in Chapter 4. Finally, for Chapter 5, Tim Scholl assisted in the construction of the butterfly gradient and in the electrical and cooling connections for that butterfly coil. Doug Hai built the switch box used during the pulse sequence to hold the current to the insert at 0. Jamu Alford configured the gradient amplifiers to drive the insert inside the gradient, and programmed the LabView driver required to control the pulse sequence.

for my parents

Acknowledgements

The completion of this thesis was due to immense support and inspiration taken from a multitude of people, all of whom have become very dear in my life. I take great pleasure in being able to thank them here, and I hope they recognize their effect on my life and my work.

Firstly, thanks to my supervisor, Blaine Chronik, who has provided me with equal parts freedom and guidance, both academically and personally. He provided the rich environment that this thesis developed in, and I am extremely grateful for having worked under his supervision.

Dr. Tim Scholl and Dr. William Handler were essential to the completion of the work showcased in this thesis. They provided day to day assistance and managed to kick start me when I got stuck. Will is a master of the computers, and Tim was a wizard in the machine shop.

The final part of my project depended on electronics that were developed by Jamu Alford. He was wonderfully patient in assisting and instructing me on the use of those components, and the discussions I had with him in the final months of my project kept me motivated to write.

A special thank you must go to students past and present, Kyle Gilbert, James Odegaard, Chad Harris, Geron Bindseil, and Dustin Haw. I could not have asked for better people to share an office with. They have been both inspiration and welcome distraction.

I am forever indebted to my friends and colleagues who helped me edit and pointed

out the flaws in the document and Helen Stewart who stood watch as I removed the comma-splices.

And further, I acknowledge the support of my family, who have loved and supported me throughout my life and my career. They have been role models, at turns both motivational and inspirational.

Finally, I also thank my advisory committee, Drs. Dick Drost and Brian Rutt, who provided insight and prospective throughout this process. I am grateful to the University of Western Ontario Department of Medical Biophysics, OGSST, and NSRC for the support I have received, in terms of facilities, funding, and opportunities.

Contents

List of Tables

List of Figures

List of Symbols

α – ratio of length to F

β – ratio of half width (radius) to F

χ – susceptibility

Δ – duration between diffusion pulses

$\Delta B"$ – local inhomogeneities in magnetic field

ΔG - change in linear magnetic gradient

ΔG_{stim} – change in linear magnetic gradient required to cause stimulation

ΔG_{min} – minimum change in linear magnetic gradient required to cause stimulation

ΔG_{max} – maximum gradient excursion

Δk_x – minimum spatial frequency in the x-direction

Δk_y – minimum spatial frequency in the y-direction

Δt – dwell time;

δ – duration of diffusion pulses

∂ – diffusion length

ε – length of single step in a random walk

ϵ – permitivitty

ϕ - phase

Φ – scalar potential

φ – azimuthal angle

Φ_n – scalar potential in voxel n

γ – gyromagnetic ratio

ζ – ratio of thickness to F

η – gradient efficiency

$\vec{\kappa}$ – coefficient relating the slew rate of a gradient coil to the electric field induced in the system.

μ_o – permeability of free space

μ – permeability

π – pi = 3.14159265358979323846

$\rho(\vec{r})$ – proton-density of sample

ρ_c – resistivity of copper

σ – conductivity

τ_d– duration of a single step in a random walk

τ – duration of electric field pulse; duration of slewed magnetic field

τ_c – chronaxie time

$\Upsilon(T_1(\vec{r}))$ – spin-lattice relaxation function of sample

ω – angular frequency

ω_o – Larmor frequency of magnetization at magnetic field B_o

Ω – acceleration factor

A – constant relating the strength of the received signal to the terms of the signal equation

$\vec{A}$ – vector potential

Λ – cross-sectional area of wire

ADC – apparent diffusion coefficient

$\vec{B}$ – magnetic Field

B_o – magnitude of static, magnetic field

B_z – component of magnetic field in z-direction

B_1 – RF field

b – b-value $[s/mm^2]$

D - diffusion coefficient

$\vec{dl}$ – current element

DWI – diffusion weighted imaging

E_{stim} – magnitude of electric field threshold of stimulation

E_r – nerve rheobase

E_{Ai} – component of the field due to vector potential in the x-direction

E_{Aj} – component of the field due to vector potential in the y-direction

E_{Ak} – component of the field due to vector potential in the z-direction

$\vec{E}_{tot}$ – total electric field

$\vec{E}_A$ – total electric field due to vector potential

$\vec{E}_\Phi$ – total electric field due to scalar potential

FOV – field of view

FDTD – Finite Difference Time Domain

F – focus of gradient system

G – linear gradient of magnetic field

G_{slice} – linear gradient of magnetic field in the direction of slice selection

G_{phase} – linear gradient of magnetic field in the direction of phase encoding

$G_{readout}$ – linear gradient of magnetic field in the direction of signal readout

$G_{diffusion}$ – gradient of magnetic field engage for diffusion-weighting

$\hbar$ – Plank's constant

$\vec{H}$ – boundary condition

I - nuclear spin (1/2 for a hydrogen nucleus)

$\hat{i}$ – unit vector in the x-direction

$\imath$ – current

it – iteration

$\vec{J}$ – current density

$\hat{j}$ – unit vector in the y-direction

j – $\sqrt{-1}$

$\hat{k}$ – unit vector in the z-direction

k – boltzmanns constant

kg – kilograms

ℓ – length of wire

$\vec{M}$ – sample magnetization

M_o – initial magnetization

M_x – magnitude of magnetization in the x-direciton

M_y – magnitude of magnetization in the y-direction

M_z – magnitude of magnetization in the z-direciton

M_R – resistive merit

M_L – inductive merit

MRI – magnetic resonance imaging

m – meters

NA^+ – sodium ion

NMR – Nuclear Magnetic Resonance

$\hat{n}$ – unit vector of the normal to the surface

$\vec{N}$ – representation of the normal to the surface in the convergence algorithm

N_x – x-component of normal to the surface

N_y – y-component of normal to the surface

N_z – z-component of normal to the surface

n – index of current of voxel

PNS – peripheral nerve stimulation

RF – radio frequency

R – distance between two points

$\vec{r}$ – position

$\hat{r}$ – direction of vector between source point and field point

R_c – electrical resistance

resid – the residual of the application of Lapalce's equation to the distribution of simulated scalar potential

SR – slew rate

SR_{min} – minimum slew rate required to cause stimulation

S_{NMR} - received signal from NMR excitation

SNR – Signal to noise ratio

t – time

T - Temperature

T_1 – spin-lattice relaxation

T_2^* - total transverse relaxation

T_2' - transverse relaxation due to reversible inhomogeneities

T_2 - spin-spin relaxation

TR – repetition time for a pulse sequence

TE – echo time for a pulse sequence

T_n – type of tissue represented by voxel

V – sample volume

V_s – voltage of signal in the receive coil from precessing magnetization in the sample

W – width of coil

x – coordinate on the x-axis

x' - coordinate of source-point on the x-axis

y – coordinate on the y-axis

y' – coordinate of source-point on the y-axis

z – coordinate on the z-axis

z '– coordinate of source-point on the z-axis

Chapter 1

Introduction and Background

Magnetic resonance imaging (MRI) is a versatile tool that detects the changing magnetic field from excited protons precessing about a powerful main magnetic field [1]. The strength of acquired signal is dependent not only on the number of protons in the sample [2] but also on other parameters such as relaxation constants [3], and other weightings that can be applied with gradients of magnetic field or contrast agents. Diffusion-weighted imaging is a contrast mechanism that depends on the application of gradients [4]. The following thesis demonstrates a method of diffusion-weighting that utilizes a novel fourth gradient axis, in addition to the three main imaging axes. Because strong, switched, magnetic fields have the potential to cause peripheral nerve stimulation in living subjects, this thesis also investigates the electric fields produced by localized gradients and the nerve stimulation thresholds of such gradients.

This chapter is intended as a brief introduction to the concepts presented in this thesis. The first section contains an overview of the principles of MRI, followed by a discussion of the theory behind diffusion-weighted imaging. Next, gradient-induced electric fields are described and the mechanism by which these fields cause peripheral nerve stimulation is discussed. Finally there is a brief overview of the thesis. The following discussion is not intended to be a comprehensive description of the entire

field behind MRI, and several good textbooks [3] [5] [6] would provide more detail regarding the concepts presented here.

1.1 Magnetic Resonance Imaging

1.1.1 NMR - Nuclear Magnetic Resonance

Nuclear Magnetic Resonance (NMR) measures the electromagnetic signal produced by precessing nuclear magnetic spins. The proton of a hydrogen atom (spin $\frac{1}{2}$), is most frequently probed, although other elements such as xenon [7] and carbon-13 [8] can also be used.

The net magnetization of the sample is proportional to magnetic field and approximately proportional to susceptibility.

$$\vec{M} = \frac{\chi}{\mu_0} \vec{B} \tag{1.1}$$

In Equation 1.1, $\vec{M}$ is the net magnetization; χ is the susceptibility, μ_o is the permeability of free space and $\vec{B}$ is the applied magnetic field.

Individual spins tend to align either parallel or anti-parallel to the field, in almost equal proportions, with a slight energy advantage to aligning parallel to the field. An excess of about one spin in a million will align with the field as opposed to against the field. This minute difference is enough to produce a detectable magnetization.

A signal is produced when the magnetization induced by a static field is excited by a perpendicular magnetic field (B_1) oscillating at the Larmor frequency (ω) defined by Equation 1.2.

$$\omega = \gamma B \tag{1.2}$$

In Equation 1.2, γ is the gyromagnetic ratio and B is the magnitude of the large static magnetic field.

The excited magnetization will experience a torque, and accelerates perpendicular to both the magnetization ($\vec{M}$) and magnetic field (B_o). Due to this torque, and assuming no relaxation from the excited state, the magnetization will begin to precess as described in Equations 1.3, 1.4, and 1.5 at the Larmour frequency ω_o defined by B_o.

$$M_x(t) = M_x(0)cos(\omega_o t) \tag{1.3}$$

$$M_y(t) = -M_x(0)sin(\omega_o t) \tag{1.4}$$

$$M_z(t) = M_z(0) \tag{1.5}$$

In Equations 1.3, 1.4, and 1.5, M_x is the component of the magnetization in the x-direction. Similarly, M_y and M_z are the components of the magnetization in the y- and z- directions and t is the time after the initial excitation. The precessing magnetization will induce an electric field; a receive coil located in that field (as shown in Figure 1.1) will detect an alternating current.

The gyromagnetic ratio for hydrogen is 42.577 MHz/T, and most MRI systems operate at magnetic field strengths between 1-10 T. This means that the frequency of both the received and excitatory signals must be radio frequencies, on the order of 100 MHz. The electromagnetic coils designed to transmit and receive at these frequencies in an MR system are therefore called radio frequency (RF) coils.
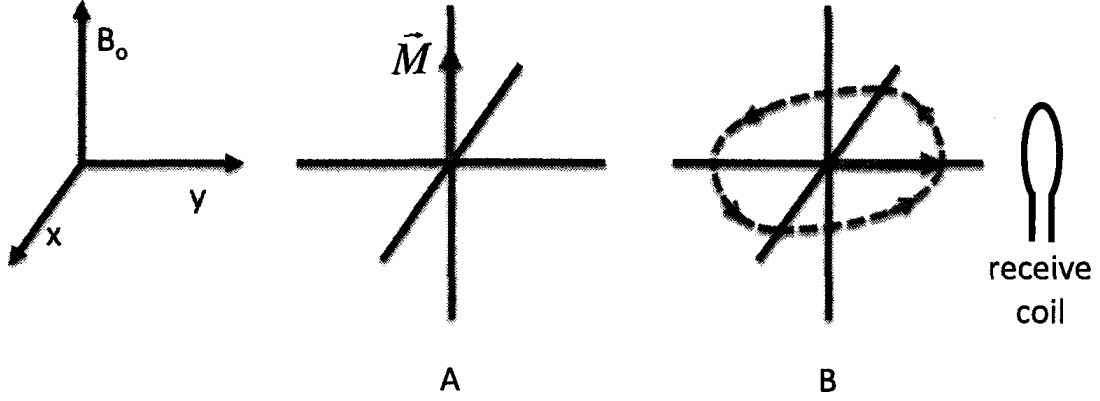
Fig. 1.1: (A) The net magnetization vector is initially aligned with the B_o field. (B) During excitation, the magnetization is tipped into the x-y plane. The component of the magnetization in the x-y plane then precesses about the B_o. The precessing magnetization induces a field that can be detected by a nearby receive coil.

By the principle of reciprocity [9], the signal (S_{NMR}) received by an RF coil, given in Equation 1.6, is proportional to the electromagnetic field (EMF) induced by the coil.

$$S_{NMR} = -\frac{d}{dt} \int_{sample} \vec{M}(r,t) \cdot \vec{B}_1(r) d^3r \tag{1.6}$$

The received signal is the dot product of the magnetization in the sample and the magnetic field of the coil, summed over the entire sample. The magnitude of the EMF is proportional to the time rate of change of M_{xy} (the frequency of oscillation in Equations 1.3 - 1.5) and the magnitude of B_o. As shown in Equation 1.7, the net signal is proportional to the frequency of oscillation and the field strength. However, the frequency is linearly dependent on field strength (Equation 1.2), so the signal is actually proportional to the field strength squared.

$$S_{NMR} \propto \omega_o B_o = \gamma B_o^2 \tag{1.7}$$

1.1.2 Bloch Equations

In Equations 1.3, 1.4, and 1.5, the assumption was made that the magnetization remained perpetually excited in the transverse plane. However, once excited, the magnetization does not precess indefinitely [10], but begins to relax back to its initial state. A phenomenological description of this behavior is given by the Bloch equation in Equation 1.8 [11].

$$\frac{d\vec{M}}{dt} = \vec{M} \times \gamma\vec{B} - \frac{M_x\hat{i} + M_y\hat{j}}{T_2^*} - \frac{(M_z - M_o)\hat{k}}{T_1} \tag{1.8}$$

In Equation 1.8, $\hat{i}$, $\hat{j}$, and $\hat{k}$, are the unit vectors in each of the x-, y-, and z-directions. T_2^* and T_1 are relaxation constants that describe the decay of the magnetization in the transverse plane and the regrowth along the z-axis.

The solution to the Bloch equation is given in Equations 1.9, 1.10, and 1.11.

$$M_x(t) = M_x(0)cos(\omega_o t)e^{\frac{-t}{T_2^*}} \tag{1.9}$$

$$M_y(t) = -M_x(0)sin(\omega_o t)e^{\frac{-t}{T_2^*}} \tag{1.10}$$

$$M_z(t) = M_o(1 - e^{\frac{-t}{T_1}}) \tag{1.11}$$

T_1 and T_2 relaxation, shown in Figure 1.2, along with proton-density weighting, are the most common contrast mechanism for MRI imaging [12]. The relaxation constant T_1, spin-lattice relaxation, represents relaxation back to resting state. T_1 is on the order of 100's of milliseconds. As the field magnitude increases, in general, the T_1 for a particular tissue increases [13].

T_2^* is de-phasing due to local inhomogeneities in magnetic field. T_2^* is considered to be composed of T_2' and T_2 effects. T_2' effects, illustrated in Figure 1.3, are local
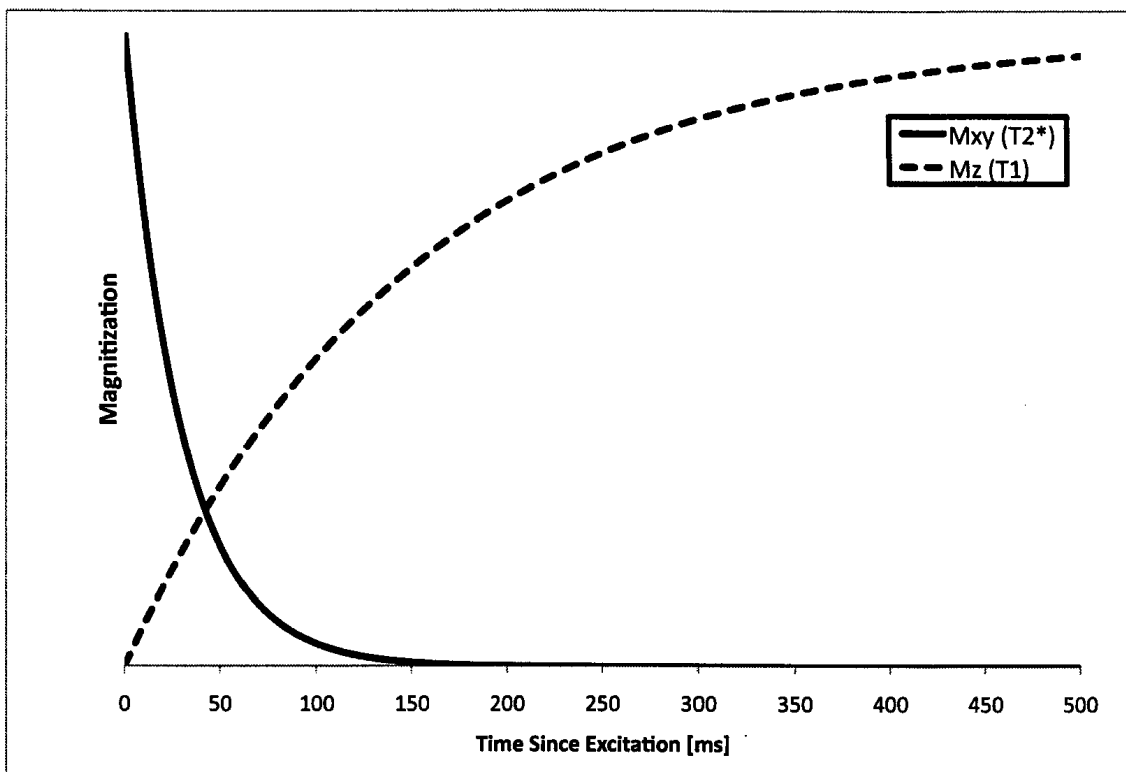
Fig. 1.2: After excitation, transverse magnetization quickly decays, while magnetization along the z-axis regrows more slowly.
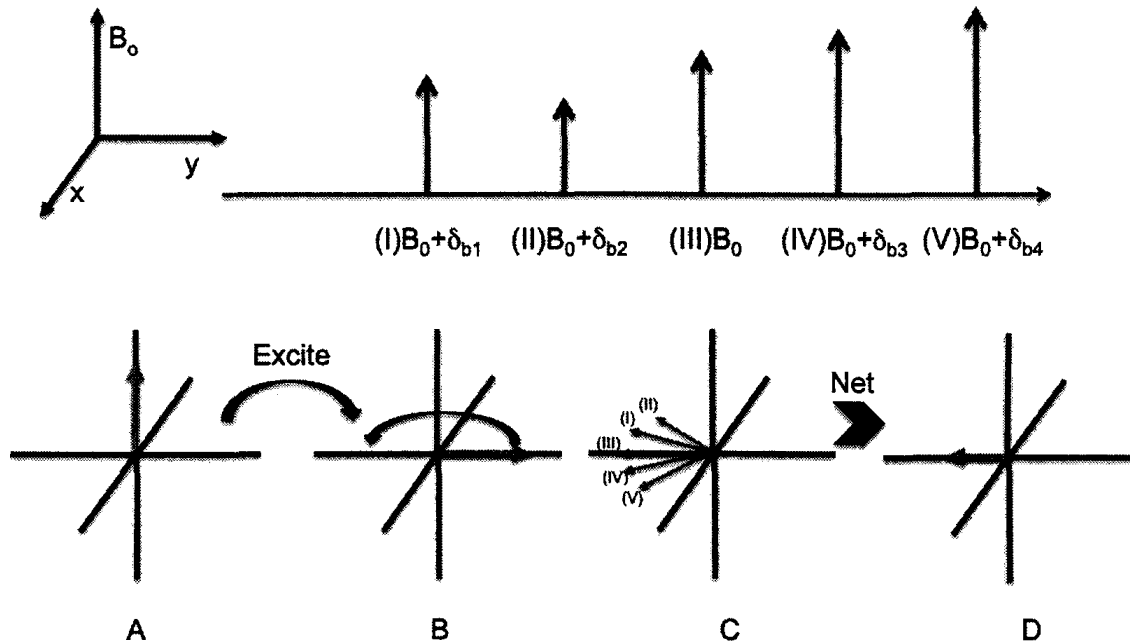
Fig. 1.3: (A) A net magnetization is excited into the transverse plane. (B) As it precesses some of the spins see a smaller magnetic field (II) and precess more slowly. Others see a larger magnetic field (V) and precess more quickly. (C) After the spins have been allowed to de-phase slightly, (D) the net relaxation is something less than the initial magnetization.

in-homogeneities which are consistent and can be reversed with careful manipulation of the magnetization. T_2, on the other hand, is spin-spin relaxation [5], which is irreversible. The spin-spin relaxation is due to interactions with adjacent protons and the fluctuating magnetic fields produced by these spins. The total de-phasing T_2^* can be calculated from T_2 and T_2' using Equation 1.12.

$$\frac{1}{T_2^*} = \frac{1}{T_2} + \frac{1}{T_2'}$$

(1.12)

T_2 is much shorter than T_1, on the order of 10's of milliseconds. As the magnitude of the field increases, T_2^* tends to decrease [13].

1.1.3 Gradient coils

T_1 and T_2 relaxations provide information regarding the composition of the sample. However, to get an image, both information from different segments of the sample and knowledge of the location of the source of each data point is required. In MRI this is done by the manipulation of gradients so as to control the phase and frequency of the signal coming from each position. The full signal equation is given in Equation 1.13 [2].

$$V_s(t) = A\omega_o B_o \frac{\gamma^2 \hbar^2 I(I+1)}{3kT} e^{-j\omega_o t} \int dV \rho(\vec{r}) \Upsilon(T_1(\vec{r})) e^{(-\frac{t}{T_2^*})}$$

$$\cdot e^{j2\pi[\frac{\gamma}{2\pi} \int_o^t dt' G(\vec{r},t)]\cdot\vec{r}} \quad (1.13)$$

$$\cdot e^{j2\pi[\frac{\gamma}{2\pi} \int_o^t dt' \Delta B''(\vec{r},t')]}$$

In Equation 1.13, j is the square root of -1; $V_s(t)$ is the voltage induced in the receiver coil; A relates the actual electromagnetic field to the acquired signal; $\hbar$ is Planck's constant; I is the proton's spin (1/2 for hydrogen); k is the Boltzmann constant and T is the sample temperature in kelvin. $\rho(\vec{r})$ is the proton density of the sample; $\Upsilon(T_1(r))$ is an exponential function that relates the signal decay to tissue type and position. The signal is also affected by any deviation in the magnetic field from perfect homogeneity, thus $G(\vec{r}, t)$ is the applied linear gradient and $\Delta B(\vec{r}, t)$ is the unintentional in-homogeneities.

If gradients are intentionally applied, like in Figure 1.4, it is possible to receive a signal that is positionally dependent and interpretable.

A linear gradient, illustrated in Figure 1.5, applied during signal acquisition will produce a signal whose frequency is linearly dependent on position. A Fourier transform of that signal will produce different magnitudes from each position with a unique
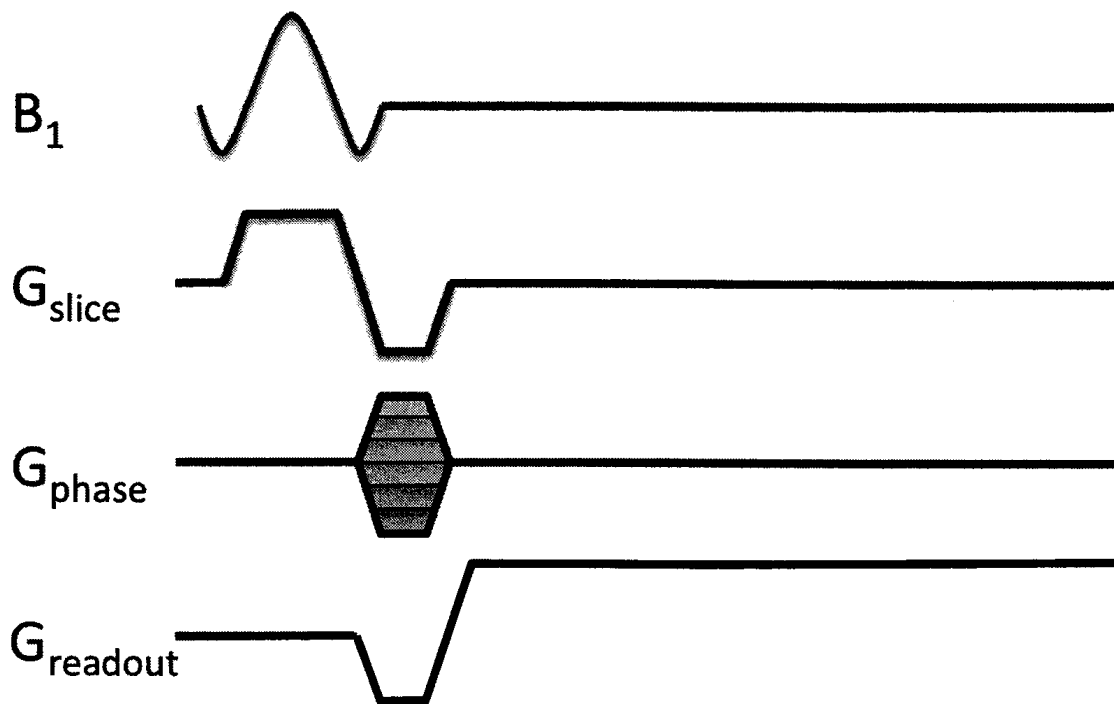
Fig. 1.4: A basic pulse sequence with linear gradients applied in 3 orthogonal directions. The signal is excited by the RF coil (B_1). Simultaneously a slice-select gradient (G_{slice}) is applied. This exposes the spins to a range magnetic fields, but only a single RF frequency is transmitted. Thus, only in the slice where the applied frequency is the Larmour frequency for the spins is magnetization excited. Next, a phase encode gradient (G_{phase}) is applied to alter the phase of the spins linearly in an orthogonal direction. Finally, the readout gradient, (G_{read}) is applied during signal acquisition so that the frequency of the received signal is proportional to the position in the third dimension.
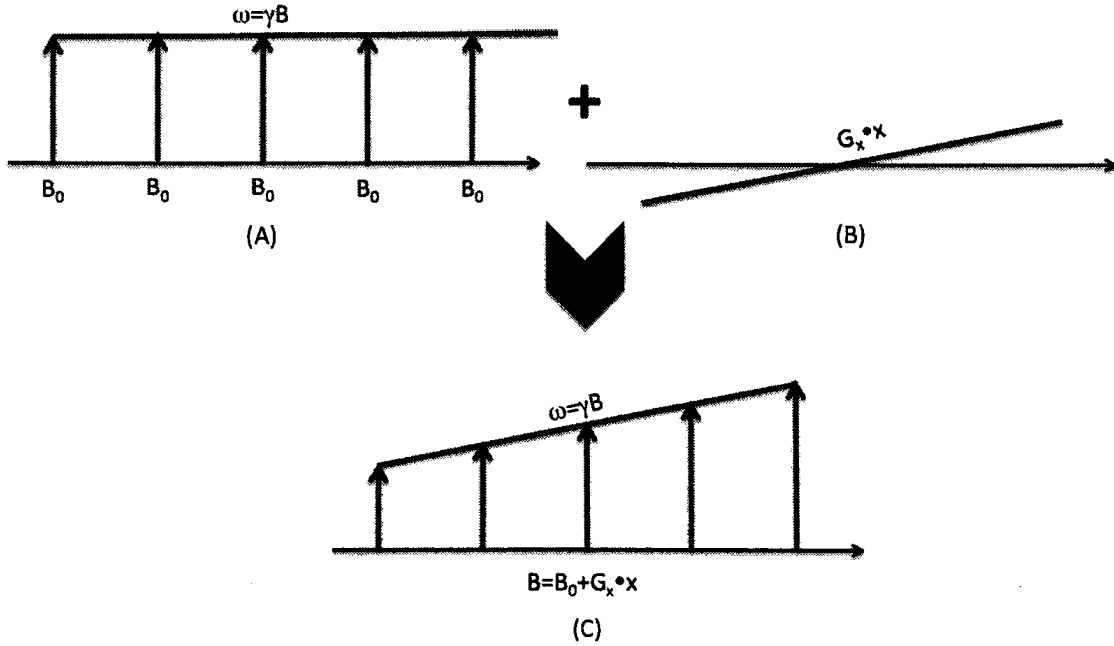
Fig. 1.5: A homogenous field (A) is added to the linear gradient (B), to produce a net field during signal acquisition (C) that allows the frequency of the received signal to be dependent on position.

frequency.

Within the signal equation, frequency encoding is represented by manipulation of the term $e^{j2\pi[\frac{\gamma}{2\pi}\int_o^t dt' G(\vec{r},t)]\cdot\vec{r}}$. If we assign a variable k_x to a portion of this equation, and assume a magnetic field with a linear gradient in the x-direction is applied for time t, as shown in Equation 1.14, we get a description of the spatial frequency [2].

$$k_x(t) = \frac{\gamma}{2\pi} \int_0^t dt' G_x(t') = \frac{\gamma}{2\pi} G_x \cdot t \qquad (1.14)$$

In Equation 1.14, k_x is the spatial frequency of the image along the x-direction. Spatial frequency is a description of how often the image is sampled and determines the level of detail in the image. Higher values of k_x, farther out in k-space, result in a finer resolution in real space. The smallest value for k defines the largest region sampled or the field of view (FOV), calculated in Equation 1.15, for the image.

$$FOV = \frac{2\pi}{\gamma G_x \Delta t} = \frac{1}{\Delta k_x} \qquad (1.15)$$

In Equation 1.15, Δk_x is the sampling step size and it corresponds to the smallest k_x overall, or the lowest spatial frequency and the largest area sampled. The largest area should correspond to the desired field of view for the image.

The readout gradients are applied while signal is being acquired. A second method of position encoding adds positional-dependent phase to the spins and then acquires the data. A gradient is applied to the sample so that magnetization in some areas precesses more rapidly than in others. After the application of the gradient pulse concludes, the spins resume then precessing in tandem and maintain their relative separation in phase. The distance between a full rotation of phase is the spatial frequency, as shown in Figure 1.6 [2]. The resulting profile gives information in a second dimension, the phase-encode direction. In Equation 1.16, the step size of the spatial frequency encoding in the phase-encoded direction is given [2], this is very similar to the equation for the frequency encode direction.

$$\Delta k_y(t) = \frac{\gamma}{2\pi} G_y \cdot \Delta t \qquad (1.16)$$

The third dimension is resolved by only exciting a single slice of the sample. In principal, excitation occurs when the spins experience an orthogonal magnetic field oscillating at the Larmor frequency. If a gradient is applied during the excitation, then the total magnetic field at a point becomes dependent on position. Basically, a single slice of the sample is exposed to the frequency it requires for excitation. Due to the magnetic field gradient, the remainder of the sample sees a RF field oscillating either too quickly, or too slowly to cause excitation.
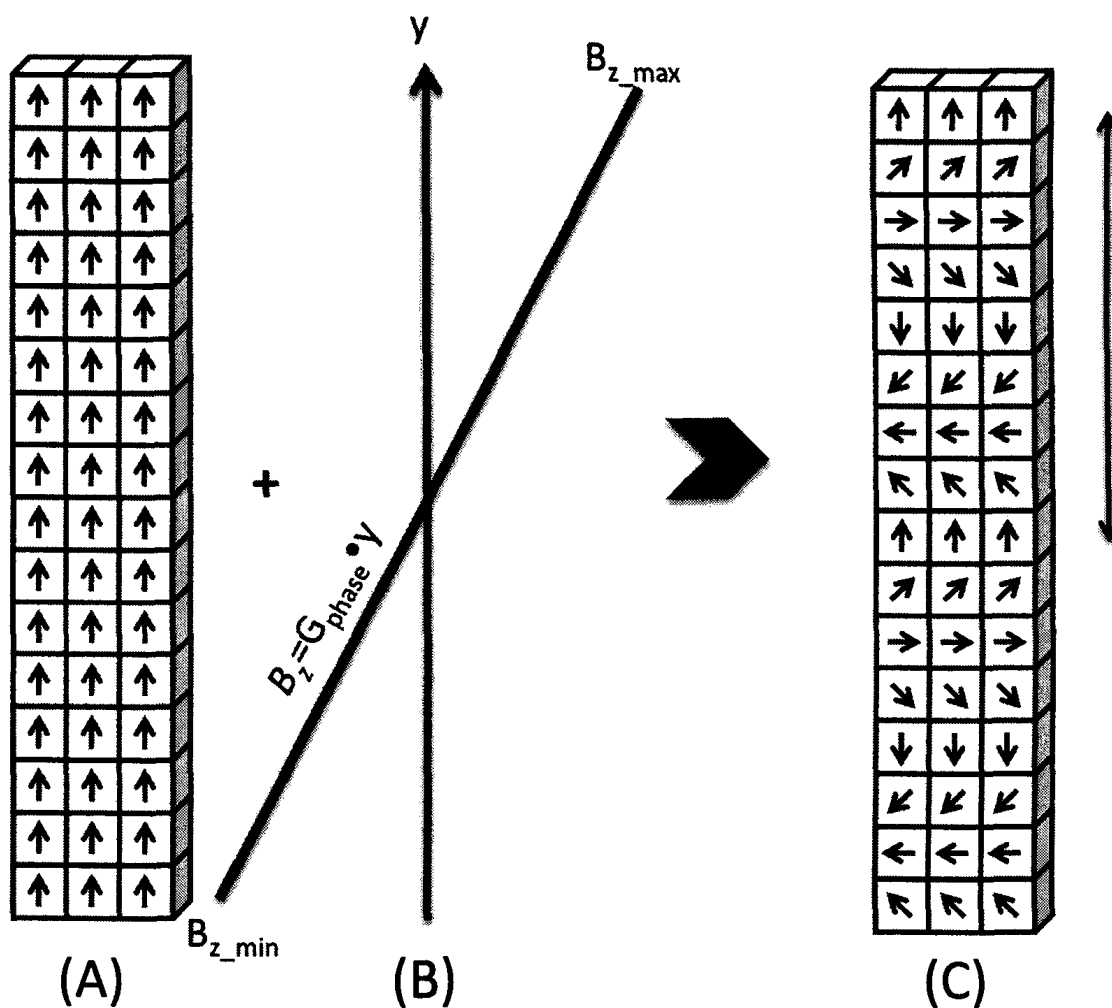
Fig. 1.6: (A) An excited sample with in-phase magnetization is exposed to a (B) magnetic field gradient, after a time the gradient is removed, and (C) the spins have de-phased. The arrow indicates the spatial sampling period for the gradient pulse in a predictable manner.

The pulse sequence diagram shown in Figure 1.4 also illustrates that the gradients do not switch on and off instantaneously. They require some time to ramp up. The rate at which they ramp is a parameter called the slew rate (SR), and is defined in Equation 1.17 [14].

$$SR = \frac{\Delta G}{t}$$ (1.17)

In Equation 1.17 ΔG is the change in gradient amplitude and t is the time over which the change took place.

1.2 Diffusion

Diffusion is the movement of matter due to random molecular motion [15]. In the body O_2 diffuses from the alveoi in the lungs into the blood stream and from the blood stream to inter- and intra-cellular spaces. Other molecules, such as water, also diffuse in and out of cells [16]. This random movement is described by application of Fick's law to diffusion to a random walk to produce Equation 1.18 for diffusion length.

$$\partial = 2\sqrt{Dt}$$ (1.18)

In Equation 1.18, ∂ is the diffusion length, D is the diffusion coefficient for the molecule in the medium, and t is the time allotted to the diffusion. Because the movement is random, Equation 1.18 only gives the magnitude of the vector travelled by the diffusing molecule and not the direction.

1.2.1 Diffusion in imaging

Diffusion can be measured in imaging by determining how much of the signal loss is due to random phase accrued by the motion of molecules. In DWI phase is imbued

intentionally by a gradient G. If the gradient is applied while diffusion is taking place, the spin sees a different magnitude magnetic field $(B(l, \tau d))$ at each point in time (τd). An example of this is represented in Equation 1.19 [3].

$$B(l, \tau_d) = B_o + G\partial \sum_{i=1}^{l} \varepsilon_i \qquad (1.19)$$

In the 1-dimensional system of Equation 1.19, ∂ is the diffusion length of the random walk and ε is indicative of the direction of that walk, either $+1$ or -1; l is the number of steps in the random walk. The phase accrued by a hydrogen atom undergoing that random walk is given in Equation 1.20.

$$\phi = - \sum_{l=1}^{N} \gamma \tau_d \Delta B(l\tau_d)$$

$$= -G\partial \gamma \tau_d \sum_{l=1}^{N} \sum_{i=1}^{l} \varepsilon_i \qquad (1.20)$$

$$(1.21)$$

Assuming that the sample is fully mixed and in equilibrium, then the mean change in phase in the sample at any time is going to be 0. On average, the molecules with a net positive phase will be countered by the molecules that have randomly acquired a net negative phase. However, the root mean square of the phase accrual, in Equation 1.22, will not be 0.

$$< \phi^2 >= \frac{1}{3} \frac{G^2 \partial^2 \gamma^2 t^3}{\tau_d} \qquad (1.22)$$

From Equation 1.13, the signal equation, the phase acquisition can be inserted into the exponential expression to obtain Equation 1.23, relating the magnetization to the magnetic field inhomogeneities.

$$M \propto M_o e^{-\frac{<\phi^2>}{2}} = M_o e^{\frac{1}{6}\frac{G^2\theta^2\gamma^2 t^3}{\tau_d}} \tag{1.23}$$

Applying Ficks law to Equation 1.23 and simplifying results in Equation 1.24.

$$M \propto M_o e^{-\frac{<\phi^2>}{2}} = M_o e^{\frac{1}{3}\gamma^2 G^2 D t^3} = M_o e^{-bD} \tag{1.24}$$

In the simple scenario developed in Equations 1.19 to 1.23, where a single gradient is applied for a fixed period and the amount of de-phasing is measured after the gradient application, the b-value can be calculated from Equation 1.25 [3].

$$b = \frac{1}{3}\gamma^2 G^2 t^3 \tag{1.25}$$

Any signal loss beyond that is not diffusion but some other de-phasing effect such as T2*. To counteract the effect of reversible de-phasing by gradients, it is common to apply a pulse sequence as shown in Figures 1.7 and 1.8: a gradient is applied so that the protons are given a phase and allowed to diffuse and after some period of time, the opposite gradient is applied. In this case, the net phase acquisition for stationary molecules is 0, but a hydrogen proton that underwent some displacement will not re-phase entirely. The resulting signal loss can be measured to determine the diffusion coefficient. The b-value for this pulse sequence is given in Equation 1.26 [17].

$$b = \gamma^2 G^2 \delta^2 |\Delta - \frac{1}{3}\delta| \tag{1.26}$$

A diffusion coefficient, D measured using a signal loss over a known b-value is known as the apparent diffusion coefficient (ADC). The actual value of the ADC can be affected by the duration of time allowed for diffusion (Δ, and other pulse sequence parameters and may not be the actual diffusion coefficient for the tissue.
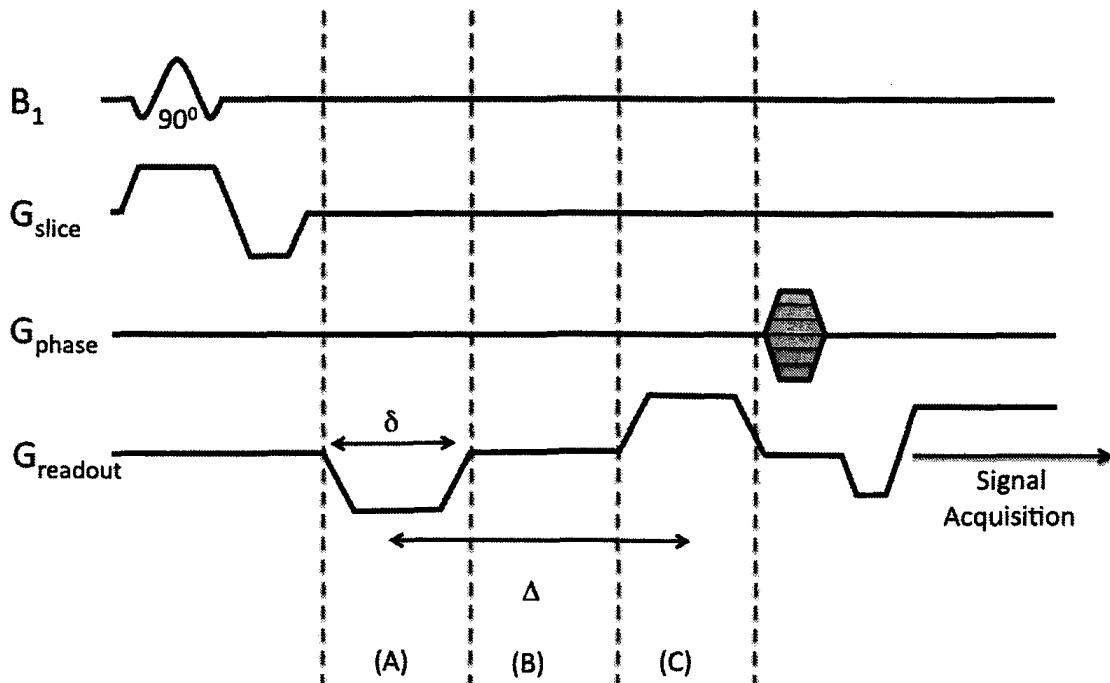
Fig. 1.7: The spins are given a phase and allowed to diffuse (A). After some period of time (B), the opposite gradient is applied (C). The net phase accrual for stationary molecules is 0, however any proton that underwent some displacement will not re-phase entirely. The resulting signal loss can be measured to determine the diffusion coefficient.
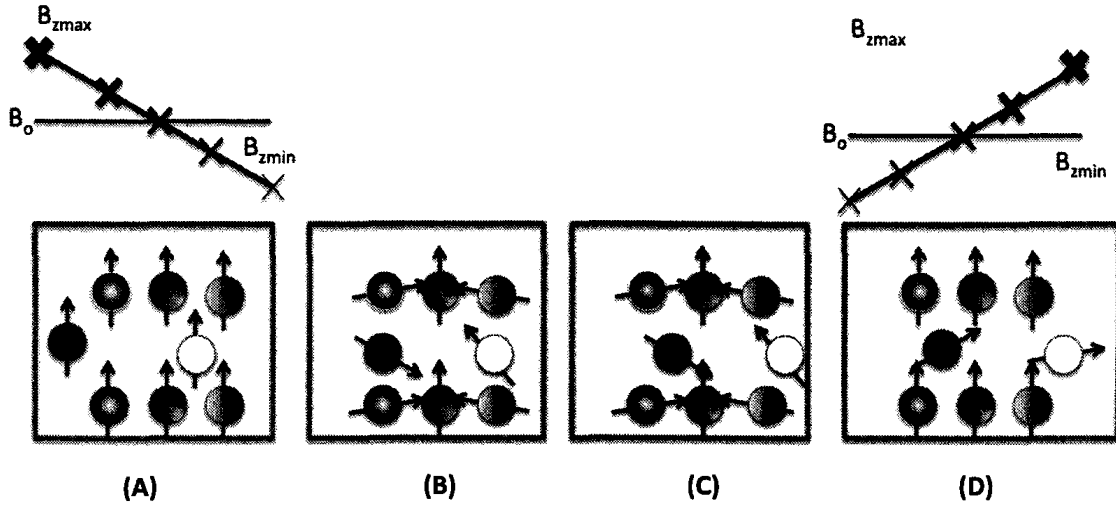
Fig. 1.8: Diffusion during a DWI pulse sequence. A gradient is applied (A). The protons are given a phase (B) and allowed to diffuse (C). After some period of time, the opposite gradient is applied (D). The net phase accrual for stationary molecules is 0, however any proton that underwent some displacement will not rephase entirely, the resulting signal loss can be measured to determine the apparent diffusion coefficient.

1.3 Electric Fields in MRI

Powerful magnets are used to excite the MRI signal, provide position information, and manipulate the contrast. With the exception of the main magnetic field, these electromagnets are switched on and off, inducing electric fields. Equation 1.27 describes the electric field in a system that is due to both the vector and scalar potentials [18].

$$\vec{E}_{tot} = \vec{E}_A + \vec{E}_\Phi = -\frac{\partial \vec{A}}{dt} - \vec{\nabla}\Phi \tag{1.27}$$

In Equation 1.27, $\vec{E}_{tot}$ is the total electric field; $\vec{E}_A$ is the field due to the vector potential ($\vec{A}$) and $\vec{E}_\Phi$ is the field due to the scalar potential (Φ).
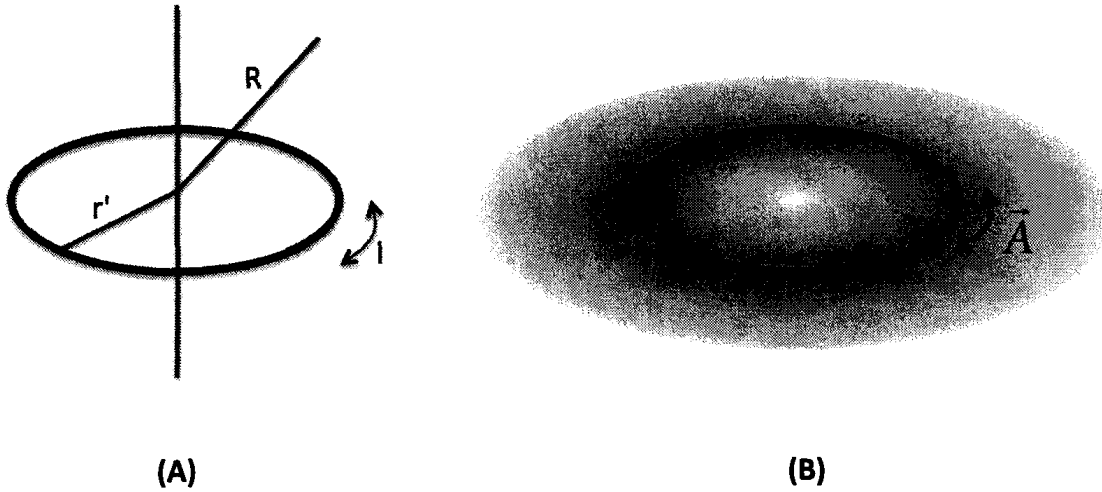
Fig. 1.9: Current flows through a closed loop (A) producing a magnetic field perpendicular to the plane of the loop and a vector potential (B).

1.3.1   Vector potential

The vector potential is due to the magnetic field as shown in Figure 1.9. A loop of current carrying wire will produce a vector potential that may be calculated with Equation 1.28 [19].

$$\vec{A}(x,y,z,t) = \frac{\mu}{4\pi} \int_V \frac{\vec{J'}(x',y',z',t')e^{-jkR}}{R}dV' \tag{1.28}$$

Where

$$R^2 = (x-x')^2 + (y-y')^2 + (z-z')^2 \tag{1.29}$$

and

$$k^2 = \omega^2 \mu\epsilon(1 + \frac{\sigma}{j\omega\epsilon}). \tag{1.30}$$

In Equation 1.28, $\vec{J}$ is the current density applied to the loop and R is the distance from the spatial vector potential point (x,y,z), to the source point (x',y',z') as shown

in Equation 1.29. In the term e^{-jkr}, k defined by Equation 1.30. In Equation 1.30, σ is the conductivity; ϵ is the permittivity of the medium and ω is the frequency.

The magnitude of the field due to the vector potential is determined by the frequency of the currents oscillation, as well as the amplitude the current.

1.3.2 Scalar Potential

Scalar potential is the contribution of static charge to the electric field. The field produced by a charged particle is given in Equation 1.31 [19].

$$\Phi(x, y, z) = \frac{1}{4\pi(\sigma + j\omega\epsilon)} \int_V \frac{\rho(x', y', z', t)e^{-jkR}}{R} dV' \qquad (1.31)$$

In Equation 1.31, ρ is a scalar representing the amplitude of the charge at each point. The scalar potential is calculated by summing over the field produced by each charge.

The field is calculated from the scalar potential using Equation 1.32.

$$\vec{E}_\Phi = -\vec{\nabla}\Phi = -\vec{\nabla}(\frac{1}{4\pi(\sigma + j\omega\epsilon)} \int_V \frac{\rho(x', y', z', t)e^{-jkR}}{R} dV') \qquad (1.32)$$

1.3.3 Quasi-static approximation

Calculation of the electric fields can be complicated. The phase of the waveform at every point in the field can be a confounding factor in an attempt to model the field. Additionally, the field decays inside a medium because the electric field induces currents that tend to cancel out the main field. The magnitude of this skin depth effect depends on the permittivity of the medium and the frequency of the field [20].

If only the electric fields produced by the gradient coils in a human body or smaller object are considered, then the fields are oscillating at a frequency on the order of kHz. The skin depth for those frequencies, in tissue, are on the order of 10 m, and the wavelength of a kHz sine wave is even longer than 10 m. Over the 1 m, or so, of a human body both the field decay and phase of the waveform can be neglected. Finally, if we can ignore the capacitive effects of the medium and model the system as purely resistive, then all complex notation is removed from the equation and what is left is the quasi-static approximations shown in Equations 1.33 and 1.34 [18].

$$\vec{A}(x,y,z,t) = \frac{\mu}{4\pi} \int_V \frac{\vec{J'}(x',y',z',t')}{R} dV' \tag{1.33}$$

$$\vec{E}_\Phi = -\vec{\nabla}(\frac{1}{4\pi(\sigma + j\omega\epsilon)} \int_V \frac{\rho(x',y',z',t)}{R} dV') \tag{1.34}$$

$$\tag{1.35}$$

This quasi-static approximation is the basis of the simulations performed in Chapters 2 and 3.

1.4 Peripheral Nerve Stimulation

1.4.1 The Action Potential

In the human body, the propagation of electrical impulses communicate, among other things, muscle and sensory stimulation [21]. The electric fields produced by a gradient coil are of interest because they can activate the nerves fibers involved in ways that can be interpreted as sensation.

Action potentials (Figure 1.10) are produced along a nerve membrane when a stimulus causes depolarization to exceed a stimulation threshold. The resting potential
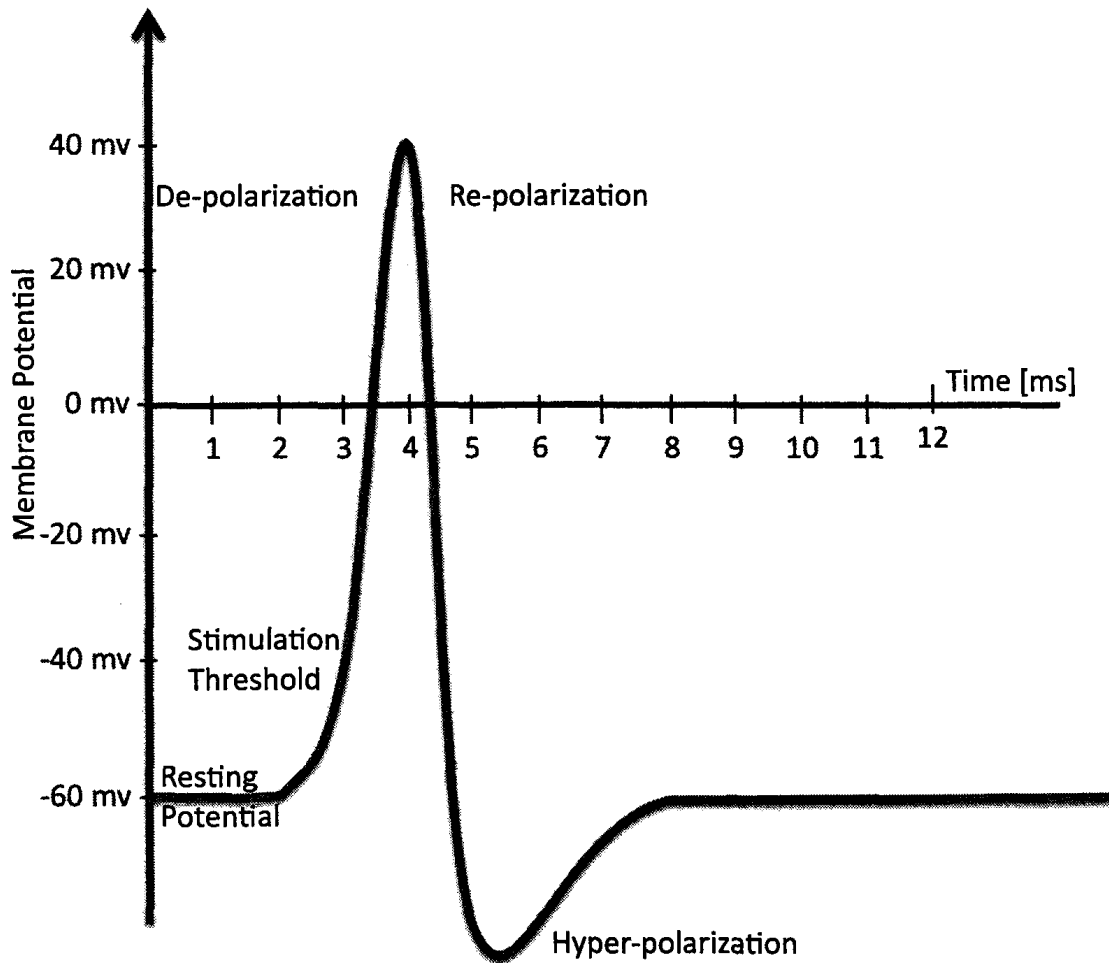
Fig. 1.10: The membrane starts at a resting potential. When the membrane potential exceeds a stimulation threshold, an action potential occurs. The potential rapidly depolarizes to a peak voltage around 40 mV. Membrane voltage decreases during re-polarization, and falls below the original resting potential. Gradually, the membrane potential increases from hyper-polarization levels to return to its resting potential.
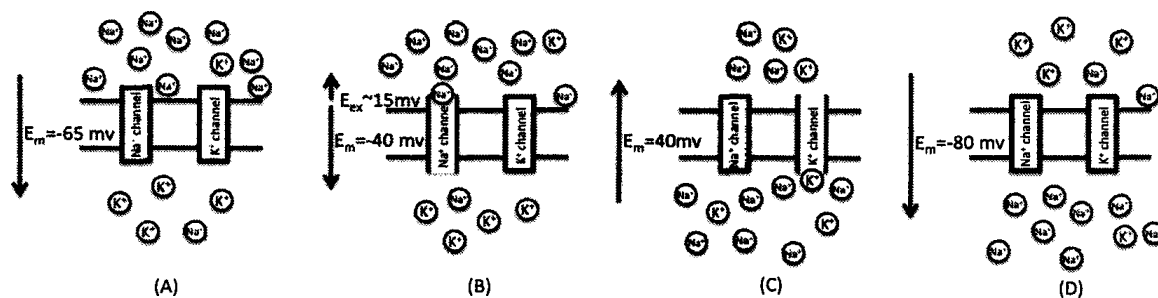
Fig. 1.11: The initial resting potential for the membrane potential is -65 mV. There is an external concentration of sodium ions and an internal concentration of potassium ions (A). If an electric field depolarizes the membrane beyond a threshold, sodium ion channels (B) open allowing a flood of positive ions into the cell. As the membrane potential reaches a peak, the sodium channels inactivate and the potassium channels open (C), causing an out-flowing of positive ions and the re-polarization of the cell. Eventually, the ion channels close (D), leaving the cell hyperpolarized. Eventually the resting potential is re-established

for a nerve membrane is about 65 mV (between 60 and 70 mV) [22], with the interior negative to the exterior. A disruption of the resting potential (such as an electric field, a synapse, or a depolarization of the membrane by a sensory receptor) can cause the membrane potential to rise. When the potential exceeds a threshold, an all-or-nothing response is triggered. Voltage-gated ion channels in the membrane open (Figure 1.11) and Na^+ moves with the concentration gradient (and initially with the electrical gradient) into the cell. The movement of the ions further depolarizes the membrane.

The action potential peaks around positive 40 mV, at which time the sodium-ion channels are inactivated and the potassium ion channels are fully open. This allows the potassium ions out of the nerve and begins the re-polarization of the membrane. Potassium ions exit the cell, again along both a concentration and electrical gradient, and the membrane re-polarizes. Eventually, the potassium channels close, but by this time the membrane potential has passed, the initial -65 mV resting potential and is
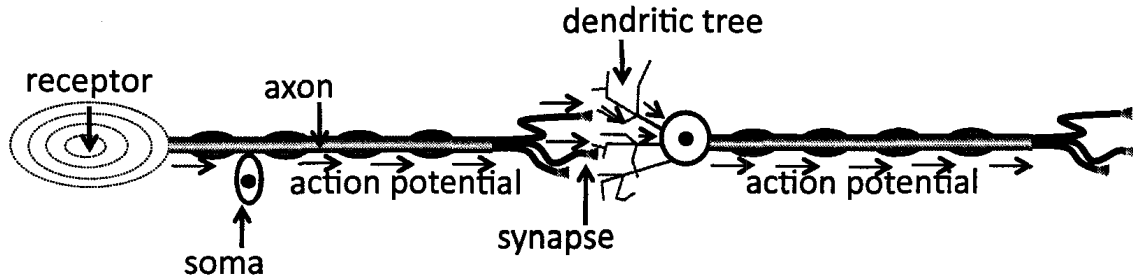
Fig. 1.12: A receptor causes the depolarization of the nerve membrane, initiating an action potential. The signal travels down the axon, and causes the release of transmitters at the synapse between nerve cells. If enough dendrites in the next nerve are excited, another action potential is propagated down the nerve or ganglion and eventually reaches the brain.

hyperpolarized. The absolute refractory period is a time during which ion-channels are closed and cannot be re-activated. Eventually, the initial ion concentrations are resumed and the membrane returns to its resting potential.

1.4.2 Signal Propagation

A signal propagates along an axon as sections of the nerve fiber's membrane are excited, depolarize, and, through depolarization, create a potential difference across the membrane that depolarizes the next section of membrane. (Figure 1.12). The signal can be propagated from one nerve fiber to another across a synapse and eventually reach its target.

An action potential can be induced in a nerve by the brain in order to activate muscles or other processes, or, conversely, receptors in the body can cause a nerve to signal in order to report sensory stimulation to the brain. Any nerve can also be excited by an externally applied electric field. Rapidly switched magnetic gradients induce electric fields in the body, with the resulting action potentials interpreted as sensations of tingling, pinpricks, pressure, or muscle contractions.

1.4.3 Stimulation Thresholds

Each nerve membrane has a stimulation threshold on the order of tens of milli-volts. However, for a signal reaching the brain to be interpreted as sensation, or for an EMF to induce a muscle twitch, axons must be stimulated together and at suffi-cient frequencies to simulate sensation. The thresholds for stimulation are described empirically in Equation 1.36 by the electric field required to cause stimulation (E_{stim}) and the duration of the pulse (τ) [23].

$$E_{stim} = E_r(1 + \frac{\tau_c}{\tau})$$ (1.36)

In Equation 1.36, E_r is the nerve rheobase, the minimum field required to cause stimulation, and is expected to be between 5-20 V/m [22]; τ_c is the chronaxie time. A pulse at the duration of the chronaxie time is on the order of 500 μs, and requires the minimum amount power to cause stimulation. This curve is illustrated in Figure 1.13.

Although RF coils operate at high frequencies and amplitudes, their very high frequency prevents the RF fields from causing stimulation. The duration of the ap-plication of the pulse is on the order of picoseconds, so the magnitude of field required to initiate an action potential is higher than can be reasonably generated by existing technology. At radio frequencies the greater concern is power deposition in tissue and heating [24].

On the other hand, the electric field pulse duration for a gradient coil is on the order of 1000 μs, which is near the chronaxie time. Thus, stimulation can be achieved with a minimum of power. Given the frequency of gradient operation it is unsurprising that one of the first physiological limitations for gradient applications is PNS.
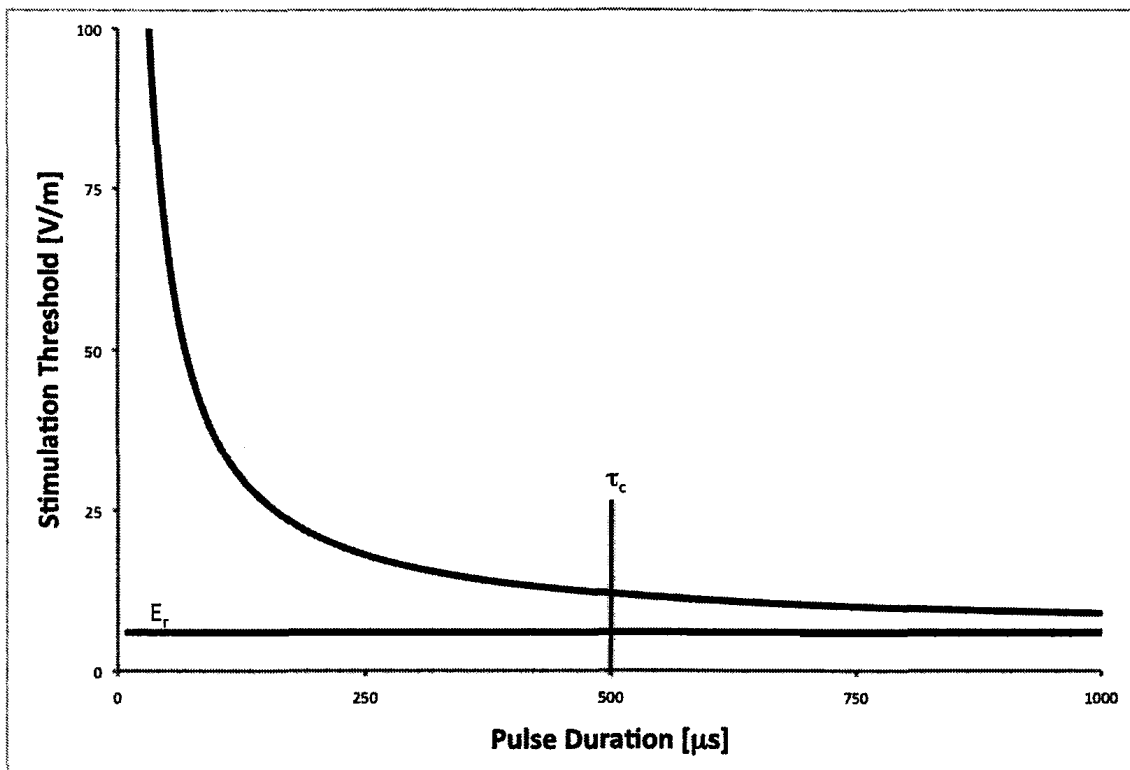
Fig. 1.13: The curve represents the minimum electric field required to cause stimulation. For an infinitely long pulse, the field required to cause stimulation is the minimum rheobase. As the duration of the pulse decreases, the magnitude of the required field increases.

1.5 Thesis Overview

This thesis describes the consideration, design, construction, and implementation of a localized gradient coil for diffusion weighted imaging, as well as investigating the stimulation due to electric field for localized gradients.

1.5.1 Simulation of Electric Fields

In the second chapter, the electric fields due to a customized head/neck gradient system were simulated with the Visible Man Model. The simulations were done to assess the relationship between gradient slew rate and induced electric fields. This chapter describes how the resolution, position, and size of the model was varied in order to determine the variation in induced electric field that might be expected from subjects of different sizes and in different positions. Nerve rheobase was estimated from the combination of simulation results and experimental data from a gradient system built to the same specifications as the simulation. The pairing of simulation and stimulation experiment is only possible in a limited number of cases where the precise wire pattern for the coil used in the stimulation experiment is known.

A version of the simulation results from this chapter was presented as a poster at the ISMRM 17th annual Scientific Meeting (2009), held in Honolulu, Hawaii.

1.5.2 PNS Experiments

The third chapter describes peripheral nerve stimulation experiments performed on a planar gradient coil for localized cardiac imaging. The planar design was similar to one of the localized gradient designs considered in the following chapter. The strong gradients possible using the localized coil and a non-cylindrical geometry suggested that a strong customized gradient system could be used for other applications, and that a non-cylindrical geometry may provide an advantage for some designs.

A modified version of this chapter has been published as a paper in the journal Magnetic Resonance in Medicine (September 2009).

1.5.3 Gradient Optimization

A design study was performed on several non-cylindrical gradient geometries. The optimal designs for butterfly, planar, half-cylindrical, and reduced radius cylindrical gradients were determined. The design studies optimized for both resistive and inductive merit and selected for strong gradients at reduced resistance or inductance. The gradient efficiencies for these designs were determined and the designs were profiled for a maximum inductance of 800 μH, a minimum wire spacing of 3 mm, with dimensions constrained to fit within a 60 cm diameter.

A version of the simulation results from this chapter were presented as a poster at the ISMRM 14th annual Scientific Meeting (2006) in Seattle, Washington.

1.5.4 Construction, Integration, and Imaging

A butterfly coil was constructed and powered during a diffusion-weighted MRI sequence. The apparent diffusion coefficients for a phantom were determined using several b-values applied by the whole body gradients. Then the insert gradient was profiled based on the b-values induced in a homogenous phantom. Finally, diffusion-weighted images were obtained using the butterfly insert for diffusion weighting and images were compared to images obtained using a full body gradient for a range of b-values.

References

[1] Curry TS; Bowdey JE; Murry RC. *Christensen's Physics of Diagnostic Radiology.* Lea and Febiger, Philadelphia, 1990.

[2] Nishimura DG. *Principles of Magnetic Resonance Imaging.* Stanford University, 1996.

[3] Haacke EM; Brown RW; Thompson MR; Venkatesan R. *Magnetic Resonance Imaging: Physical Principals and Sequence Design.* Wiley-Liss, 1999.

[4] Bammer R. Basic principles of diffusion-weighted imaging. *European Journal of Radiology*, 45(3):169–184, 2003.

[5] Callaghan PT. *Principles of nuclear magnetic resonance microscopy.* Oxford University Press Inc., New York, 1991.

[6] Bernstein MA; King KF; Zhou XJ. *Handbook of MRI pulse sequences.* Elseviere Academic Press, Burlington, 2004.

[7] Ruppert K; Brookeman JR; Hagspiel KD; Mugler JP 3rd. Probing lung physiology with xenon polarization transfer contrast (xtc). *Magnetic Resonance in Medicine*, 44(3):349–357, 2000.

[8] Gordon RE. Magnets, molecules, and medicine. *Physics in Medicine and Biology*, 30(8):741–770, 1985.

[9] Scott CG. *NMR imaging of current density and magnetic fields.* PhD thesis, University of Toronto, 1993.

[10] Cowan B. *Nuclear Magnetic Resonance and Relaxation.* Cambridge University Press, New York, 1997.

[11] Block FA. Nuclear induction. *Physical Review*, 70:460–474, 1946.

[12] Mansfield P; Harvey PR. Limits to neural stimulation in echo-planar imaging. *Magnetic Resonance in Medicine*, 29:746–758, 1993.

[13] Gomori JM; Grossman RI; Yu-Ip C; Asakura T. Nmr relaxation times of blood: dependence on field strength, oxidation state, and cell integrity. *Journal of Computer Assisted Tomography*, 11(4):684–90, Jul-Aug 1987.

[14] Havel WJ; Nyenhuis JA; Bourland JD; Foster KS; Geddes LA; Graber GP; Waninger MS. Comparison of rectangular and damped sinusoidal db/dt waveforms in magnetic stimulation. *IEEE Transactions in Magnetics*, 33(5):4267–4271, 1997.

[15] Brogiloli D; Vailati A. Diffusive mass transfer by nonequilibrium fluctuations: Fick's law revisited. *Physical Review E*, 63:1–4, 2001.

[16] Maton A; Hopkins J; Johnson S; LaHart D; Quon-Warner M; Wright JD. *Cells Building Blocks of Life*. Prentice Hall, New Jersey, 1997.

[17] Stejskal EO; Tanner JE. Spin diffusion measurements: spin echoes in the presence of a time-dependent field gradient. *Journal of Chemical Physics*, 42:228–292, 1965.

[18] Plonsey R; Heppner DB. Considerations of quasi-stationarity in electrophysicological systems. *Bulletin of Mathematical Biophysics*, 29:657–664, 1967.

[19] Young HD; Freedman RA. *University Physics with Modern Physics*. Addison-Wesley, 2000.

[20] Roth BJ; Cohen LG; Hallett M. The electric field induced during magnetic stimulation. *Magnetic Motor Stimulation: Basic Principles and Clinical Experience*, 43:268–278, 1991.

[21] Bower JB; Beeman D. *The Book of Genesis: Exploring Realistic Neural Models with General Neural Simulation System*. Springer Verlag, New-York, 1997.

[22] Reilly JP. *Applied bioelectricity.* Springer-Verlag, New-York, 1998.

[23] Irnich W; Schmitt F. Magnetostimulation in mri. *Magnetic Resonance in Medicine*, 33:619–623, 1995.

[24] Smith MB Collins CM; Li S. Sar and b1 field distributions in a heterogeneous human head model within a birdcage coil. *Magnetic Resonance in Medicine*, 40(6):847–856, 1998.

Chapter 2

Electric Field Simulation

2.1 Introduction

High performance gradient systems are desirable in magnetic resonance imaging (MRI) because they can be used to reduce imaging time, increase image resolution, improve image signal-to-noise ratios, or provide a combination of all three of these benefits [1]. Improvements in gradient strength can be made by increasing the capabilities of the gradient amplifier or by improving the efficiency of the gradient coil. However, simply increasing the gradient strength is not always possible, as the rapidly changing magnetic fields induce electric fields [2] [3], and in tissue these fields can cause undesirable peripheral nerve stimulation (PNS) [4] [5]. The onset of PNS represents an operational limit to gradient strength and slew rate, and this threshold is a significant consideration in the development of pulse sequences. The theory of PNS is developed by adding the effects of externally generated electric fields, present during gradient switching, to the standard physiological cable theory of action potential initiation and propagation along electrically excitable cell membranes [6] [7]. One model describes the stimulation threshold curve in terms of the magnitude and duration of the induced electric field [3]. The magnitude of the induced electric field (E_{stim}) at the stimulation threshold is related to the duration (τ) of that field as

illustrated in Equation 2.1.

$$E_{stim} = E_r(1 + \frac{\tau_c}{\tau})$$ (2.1)

In Equation 2.1, the nerve rheobase (E_r) is the minimum electric field required to cause stimulation and the nerve chronaxie time (τ_c) describes the shape of the stimulation threshold curve. For a pulse duration $\tau = \tau_c$, the stimulation threshold is twice the rheobase. Although the magnitude of the electric field stimulation threshold is theoretically independent of the positioning of the wires that comprise the gradient system [8], this model is not frequently used when evaluating the threshold of nerve stimulation caused by switched gradients because of the difficulty inherent in accurately determining the electric field experienced by the nerve.

2.1.1 Peripheral Nerve Stimulation During Gradient Operation

PNS studies in gradient systems focus on the change in magnetic field required to cause stimulation rather than the induced field. Studies report their results in terms of pulse sequence parameters or the magnetic field slew rate (dB/dt) [8] [9]. A stimulation threshold model that describes the gradient change required to produce nerve stimulation (ΔG_{stim}) in terms of MRI pulse sequence parameters [10] is Equation 2.2.

$$\Delta G_{stim} = \Delta G_{min} + SR_{min} \cdot \tau$$ (2.2)

In Equation 2.2, τ is the time over which the gradient is varied. The slope of the linear threshold curve (SR_{min}) is the minimum change in gradient amplitude per unit time required to cause stimulation. The intercept (ΔG_{min}) is the minimum change in gradient strength required to cause stimulation, regardless of the slew rate. This simple model has been experimentally verified in a number of studies [11] [12] [13].

However, the actual values of ΔG_{min} and SR_{min} vary from coil to coil [12] [9] [14] and are likely strongly affected by details of the gradient wire pattern.

A conversion from the simple linear formulation of pulse sequence parameters in Equation 2.2 to the hyperbolic electric field parameter model of Equation 2.1 requires an estimate of τ_c and E_r from the experimental model. To estimate the chronaxie time from experimental data, a conversion from the pulse sequence parameters must be done. It can be shown that the chronaxie time is the ratio of the two pulse sequence parameters ΔG_{min} and SR_{min} as in Equation 2.3.

$$\tau_c = \frac{\Delta G_{min}}{SR_{min}} \tag{2.3}$$

The chronaxie time for a nerve is expected to be the same across different experiments, regardless of the gradient coil causing the stimulation. However, the chronaxie time for different nerves change depending on the nerve diameter [15].

2.1.2 Gradient Induced Electric Fields

In order to calculate rheobase, the electric field generated by slewing the magnetic field of the gradient coil must be known. The electric field will be proportional to the slew rate, as shown below in Equation 2.4; however, the proportionality constant $(\vec{\kappa}(\vec{r}))$ will be dependent on the individual wire pattern of the gradient system under investigation and position of the subject with respect to the system.

$$\vec{\kappa}(\vec{r}) \cdot SR_{min} = \vec{E}_{tot} \tag{2.4}$$

To calculate $\vec{\kappa}$, an estimate must be made of the electric field pattern induced in the system by the time-varying magnetic field. The electric field in the system is a combination of the electric field due to the changing magnetic field, the vector

potential ($\vec{A}$) and the field due to the distribution of charged particles, the scalar potential (Φ.) These two components combine linearly to produce the total electric field ($\vec{E}_{tot}$) from Equation 2.5.

$$\vec{E}_{tot} = \vec{E}_A + \vec{E}_\Phi = -\frac{\partial \vec{A}}{dt} - \vec{\nabla}\Phi \qquad (2.5)$$

The vector potential calculated directly from the current wire pattern for any arbitrary current density ($\vec{J}$), assuming the quasi-static approximation, [16] is shown in Equation 2.6.

$$\vec{A}(x,y,z,t) = \frac{\mu}{4\pi} \int_V \frac{\vec{J'}(x',y',z',t')}{R} dV' \qquad (2.6)$$

In Equation 2.6, μ is the permeability of free space; x, y, and z indicate the location of the field point and $\vec{J}(x',y',z',t)$ refer to source points, essentially defining the wire pattern. R is the distance between the field and source points given by Equation 2.7.

$$R^2 = (x - x')^2 + (y - y')^2 + (z - z')^2 \qquad (2.7)$$

The scalar potential in Equation 2.8 is calculated directly from the electric charge density ($\rho(x,y,z)$).

$$\Phi(x,y,z) = \frac{1}{4\pi(\sigma + j\omega\epsilon)} \int_V \frac{\rho(x',y',z',t)}{R} dV' \qquad (2.8)$$

In Equation 2.8, σ is the conductivity, and ϵ is the permittivity of free space. However, unlike the wire pattern (source points) for a gradient coil, the charge densities in the system are not precisely known, so the solution to the scalar potential has to be determined using Laplaces equation (Equation 2.9), and a quasi-static boundary condition (Equation 2.10.)

$$\nabla^2 \Phi = 0 \tag{2.9}$$

$$\frac{d\Phi}{d\hat{n}} = \hat{n} \cdot \vec{E_A} \tag{2.10}$$

In Equation 2.10, $\hat{n}$ is the unit vector perpendicular to the surface of the boundary between conductive and non-conductive material and $\vec{E_A}$ is the electric field due to the vector potential.

Studies have been undertaken of the electric fields induced in subjects by movement in the static magnetic field surrounding an MR system [17] [18], and some electric field modeling of subjects in a switched gradient have been reported using other methods, such as modeling the vector potential alone, or finite-difference (FDTD) modeling [19]. The calculation of scalar electric field can be accomplished without the quasi-static approximation, by a FDTD method. However, in FDTD the spatial resolution of the final simulation is limited by the temporal resolution. Given the relatively low frequency of a gradient pulse, the processing of an entire wavelength is computationally intensive at a reasonable spatial resolution. In this study a quasi-static approach was used to investigate the electric fields generated during the operation of a customized head gradient with a simulated human subject [20] for comparison with real nerve stimulation data. In addition, the effect of model size and resolution was investigated.

2.2 Method

2.2.1 Simulation

The electric field was calculated as the sum of two parts, the field due to the vector and the scalar potential. The vector potential was calculated from a discretized set of source points that represented the wire pattern for each axis of the gradient

coil. Each source point was represented by a spatial location, (x, y, z), as well as a length, $\vec{dl}$, which was expressed in Cartesian component form as (dx, dy, dz). The field contributions from each source point were summed to produce the vector potential $(\vec{A}(x, y, z))$. Taking the derivative of $\vec{A}$ with respect to time, as in Equation 2.5, yielded the vector potential contribution to the electric field $(\vec{E}_A(x, y, z))$. This process was repeated until the electric field was found for all points at the desired resolution.

2.2.2 Visible Man Model

The conductive human body was modeled using the Visible Man data set [20] to define the boundaries where charge accumulation produced the scalar potential. The electric field due to the scalar potential $(\vec{E}_\Phi(x, y, z)$) was estimated using Laplaces Equation (Equation 2.9), and a boundary condition (Equation 2.10). The boundary condition depended on both $\vec{E}_A(x, y, z)$, and the shape of the boundary, as defined by a representation of the normal to the surface $(\vec{N}(x, y, z))$ in component form (N_x, N_y, N_z). The normal to the surface was determined by analyzing the boundary between tissue and air on the Visible Man data set. The procedure for determining the direction of the normal is outlined in the appendix. An approximation of the scalar potential was obtained by iterating through the convergence algorithm, also outlined in the appendix. The electric field due to scalar potential was then calculated from Equation 2.4 and the total electric field was estimated by combining the contributions of both the scalar and vector potential according to Equation 1.27.

2.2.3 Gradient Coil Wire Pattern

All electric field simulations assumed a current slew rate (dI/dt) of 6283 A/s. This corresponded to the maximum slew rate for a 1-kHz-sinusoidal waveform with an amplitude of 1 A.

Axis	x-axis	y-axis	z-axis
Diameter [cm]	32.5	35.5	38.5
η [mT/m/A]	0.40	0.35	0.37
L at 1 kHz [μH]	780	820	870
R at 1 kHz[mΩ]	227	290	210

Table 2.1: Characteristics of a localized gradient designed specifically for the head and neck region. Information on the z-gradient axis is provided only for completeness. Only the x- and y- gradient axes were simulated.

In this study, the electric fields generated by a gradient coil designed specifically for the head and neck region [21] were considered. The gradient coil was comprised of three discrete axes, which produced a linear gradient of the z-component of magnetic field (B_z) in each of the x-, y-, and z- directions. For the simulation, each axis was represented by an array of more than 23,000 source points that approximate the wire pattern. The characteristics of the gradient axes are given in Figure 2.1. Information is provided for all 3 gradient axes designed and constructed for the customized coil. However the z-axis was not simulated in this study as it was not used in the nerve stimulation experiment. Information on the z-gradient axis is provided only for completeness. The constructed gradient coil had an inner diameter of 32 cm and an outer diameter of 42 cm. The average minimum field of view for this gradient set was 7.9 cm and the imaging region was located at the edge of the coil. Figure 2.1 illustrates this gradient coil and imaging region (shaded) for both a) neck, and b) brain imaging mode.

2.2.4 Investigation of Position-Dependent Induced Electric Field

Simulations were undertaken on a Visible Man model with 3-mm resolution (except where noted). The model was simulated in two physical positions. In the first position (Figure 2.1A), the shoulders were situated at the edge of the gradient coil,
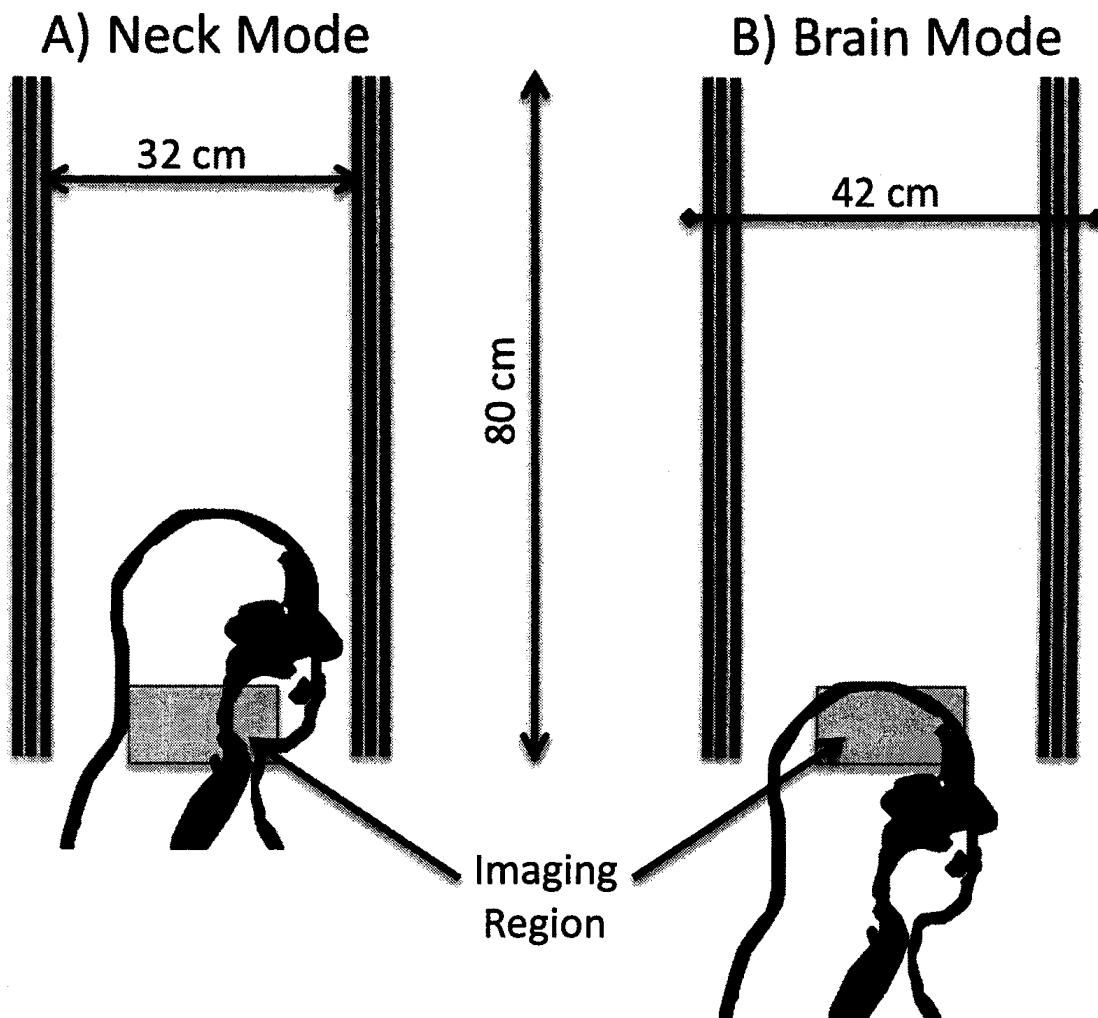
Fig. 2.1: Relative size and position of imaging region for a subject in the head/neck gradient coil for a) neck mode (with the neck in the imaging region) and b) brain mode (with the brain in the imaging region.). The inner diameter of the coil is 32 cm (shown in A) and the outer diameter of the coil is 42 cm (shown in B).

corresponding to a distance of 90.95 cm between the geometric centre of the gradient coil and the geometric centre of the model (the geometric centre of the model is illustrated in Figure 2.2). In this position, labeled neck mode, the neck was in the centre of the coil's imaging region. In the second position (Figure 2.1B) the nose was aligned with the edge of the coil, corresponding to a displacement of 104.45 cm between the centre of the coil and the centre of the Visible Man. In this position, labeled brain mode, the brain was centered in the imaging region. The electric field in and around the full-sized model of the Visible Man was simulated in both neck and brain modes at highest resolution using 3-mm isotropic voxels.

2.2.5 Investigation of Resolution-Dependent Induced Electric Field

The resolution of the model was adjusted by grouping adjacent voxels. A lower resolution of 6-mm x 6-mm x 6-mm was achieved by grouping a cube of 8 adjacent voxels. Likewise, the resolution was adjusted to 9-mm x 9-mm x 9-mm by grouping a cube of 27 adjacent voxels. The resulting larger voxels were categorized as either conductive or non-conductive according to the constituent set of 3-mm-sided voxels. The electric field in and around the full-sized Visible Man was simulated for 3-mm, 6-mm, and 9-mm sided voxels positioned in neck mode.

2.2.6 Investigation of Model-Size-Dependent Induced Electric Field

To simulate the effects of the variation in human head volumes, the size of the Visible Man model was adjusted by scaling the model in relation to the dimensions of the gradient coil. The full-sized model was 187.8 cm tall (z-axis), 58.8 cm wide (x-axis), 34.2 cm deep (y-axis), and each voxel was 3-mm, isotropically. The dimensions of the model when it was reduced in size by 10% and 20% (producing 90% and 80%
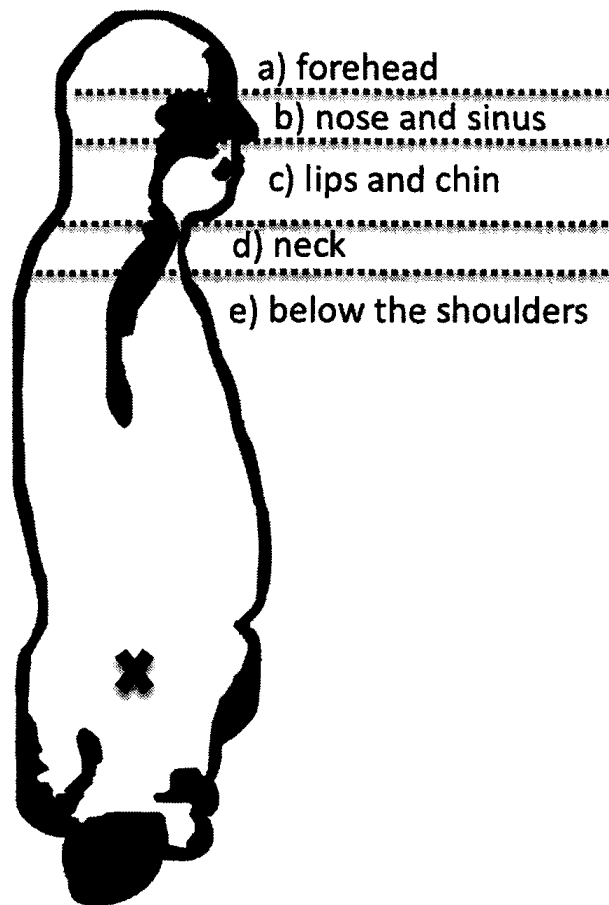
Fig. 2.2: Regional division of Visible Man Model used for analysis of peak electric field location. The five regions are a) forehead, b) nose and sinus, c) lips and chin, d) neck, and e) below the shoulders. The **X** marks the geometric centre of the Visible Man Model when the legs are included.

Scale	100%	90%	80%
z-axis(height) [cm]	187.8	169	150.2
x-axis(width) [cm]	58.8	52.9	47
y-axis(depth) [cm]	34.2	30.6	27.4
voxel-side-length [mm]	3	2.7	2.4

Table 2.2: Characteristics of scaled Visible Man Model for 100%, 90% and 80% of the model size.

scaled models) are shown in Table 2.2. The 90% model was positioned with its centre 83.8 cm from the coil centre to maintain the neck in the coils imaging region. The 80% model was positioned with its centre 76.7cm from the middle of the coil. The electric field in and around the model, positioned in neck mode, was simulated for the full-sized, 90%, and 80% model.

From each of the simulations, the maximum calculated electric field was determined. The peak electric field was obtained for each of the five sub-regions: a) the forehead, b) the nose and sinus, c) the lips and chin, d) the neck, and e) the region below the shoulders). Figure 2.2 illustrates the division into regions on the Visible Man model. The peak calculated electric fields for these regions were compared to the number of subjects reporting stimulation in each of these areas during experimental determinations of nerve stimulation thresholds.

The maximum induced electric field from each simulation was combined with the experimentally determined SR_{min} from previously performed peripheral nerve stimulation experiments for both neck and brain mode positions [22]. From this information, and using Equations 2.1 and 2.4, the nerve rheobase was estimated.

2.3 Results

2.3.1 Simulation of the Gradient Coil

Figure 2.3 shows a) the z-component of the magnetic field, b) the gradient efficiencies, and c) the empty-coil electric field of the customized head/neck gradient coil wire pattern. The efficiencies of the x-, y-, and z-gradient axes are 0.42 mT/m/A, 0.35 mT/m/A and 0.37 mT/m/A respectively, with the peak positive and negative magnetic fields located near the x- and y- edges of the coil, and the z-component of the magnetic field is 0 in the middle of the system. The linear gradient imaging region for this coil was designed to be located along the end of the coil ($z=$ 29 cm). Finally, the electric fields were calculated assuming a 1-ampere, 1-kHz sinusoidal current waveform (6283 A/s) for each axis. The peak electric fields were located close to the surface of the wires where the changing magnetic fields were the strongest.

2.3.2 Model Resolution

The effect of model resolution on the estimated electric field driven by a 6283 A/s changing current is illustrated in Figure 2.4. The first set is a sagittal slice through the sinuses and trachea of the Visible Man at 3-mm isotropic resolution. The second set shows the same slice at 6-mm isotropic resolution, where some of the sinus detail has disappeared. The 9-mm isotropic resolution map illustrates a marked reduction of sinus detail to the point that the sinus passage tissue had merged with the tissue in the head. The peaks in the fields disappeared as the resolution was decreased. In the region behind the eyes and in the forehead, there were decreases in both peak and average electric field magnitude. The graph in Figure 2.5 quantifies the effect this has on the calculation of maximum electric field and the location of the maximum field. When driven at a $dI/dt_{max} = 6238 A/s$ (1-kHz, 1-A sinusoid) on the x- and y- axes, the gradient coil electric field simulation produced a maximum electric field
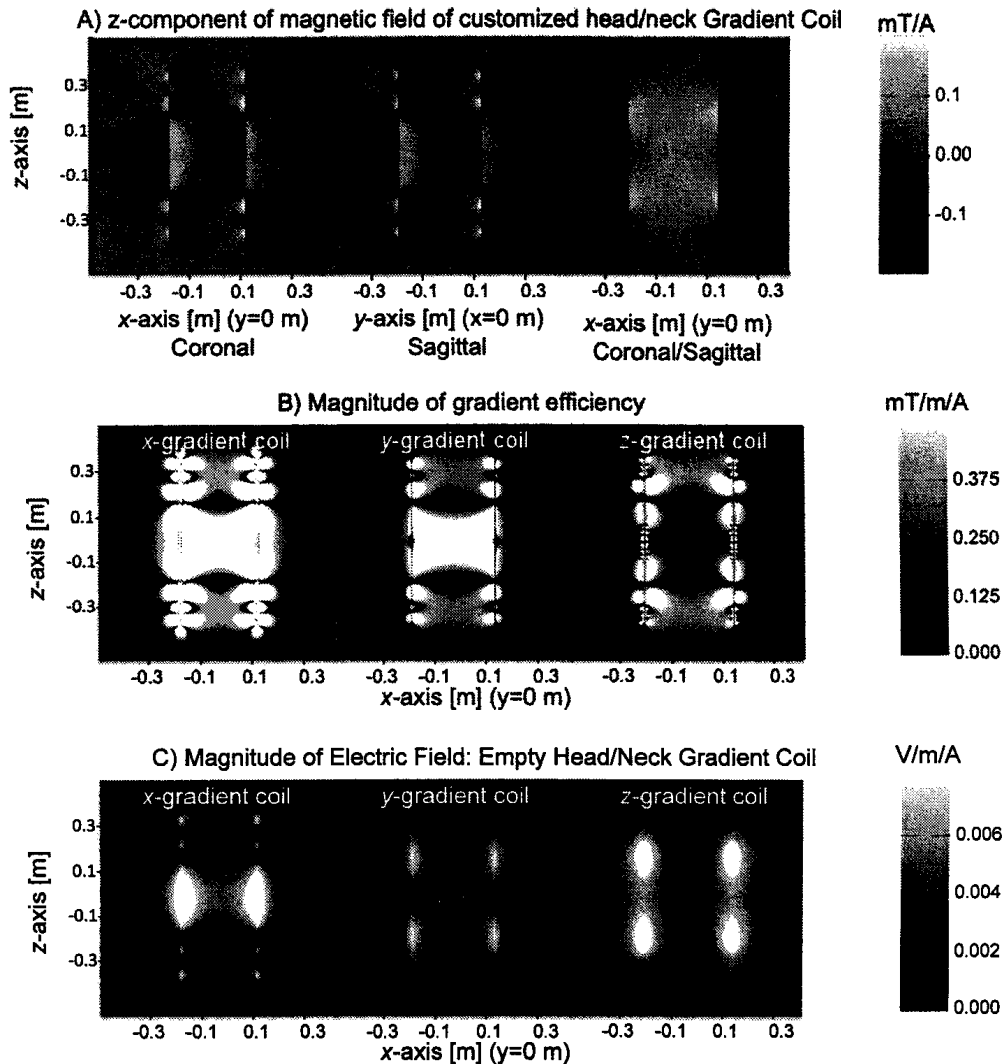
Fig. 2.3: A) z-component of the magnetic field for the customized head/neck gradient coil. Shown is the magnetic field per ampere of current for a single slice through the centre of the x-gradient wire pattern (left: coronal slice through the isocentre), the y-gradient wire pattern (middle: sagittal slice through the isocentre), and the z-gradient wire pattern (right: identical for sagittal and coronal slice). (B) The efficiency of the gradient of the z-component of the magnetic field in the x-direction (left), y-direction (middle), and z-direction (right). (C) Magnitude of the electric field produced by the head/neck gradient coil at the maximum slew rate of a 1-A-1-kHz-sinusoidal current waveform for the x-gradient axis (left), the y-gradient axis(middle), and the z-gradient axis(right).
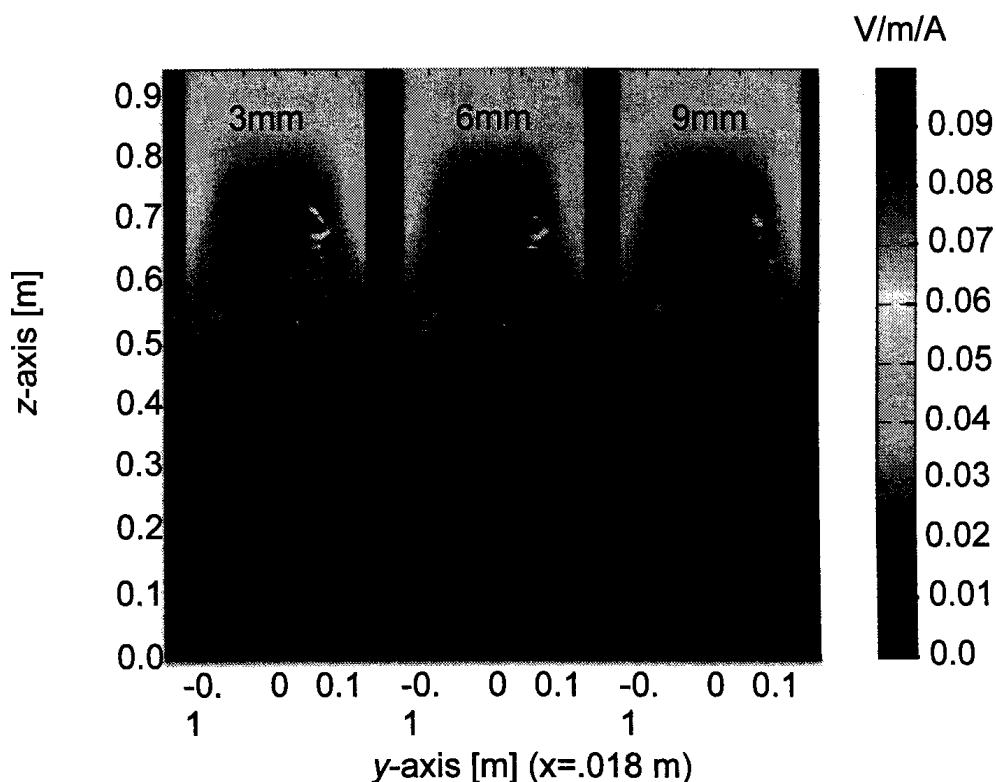
Fig. 2.4: Magnitude of the electric field produced by the head/neck gradient coil with the neck of the Visible Man Model positioned at the imaging region. The calculations were based on a 1-A-1-kHz-sinusoidal current waveform using isotropic voxel sizes of 3-mm (left), 6-mm (middle), and 9-mm (right).

of 0.178 V/m for 3-mm resolution. This maxima was located in the sinuses. For 6-mm resolution, the 0.085 V/m maximum electric field was located in forehead. The maximum was decreased to 0.080 V/m at 9-mm resolution and remained located in the vicinity of the forehead.

2.3.3 Model Size

Figure 2.7 demonstrates the effect of changing the size of the model on the maximum induced electric field, as well as the location of the maximum field on the model. The first bar in each set is the relative peak electric field for the full-sized model in neck mode, the second bar is the field for the model at 90% size, and the third bar

Magnitude of Electric Field by Region: Adjusted Model Resolution

	3 mm voxel	6 mm voxel	9 mm voxel
■ Forehead	0.128	0.085	0.080
▓ Sinus	0.178	0.049	0.042
■ Lips	0.055	0.056	0.052
■ Neck	0.096	0.069	0.039
▓ Shoulders	0.060	0.060	0.079
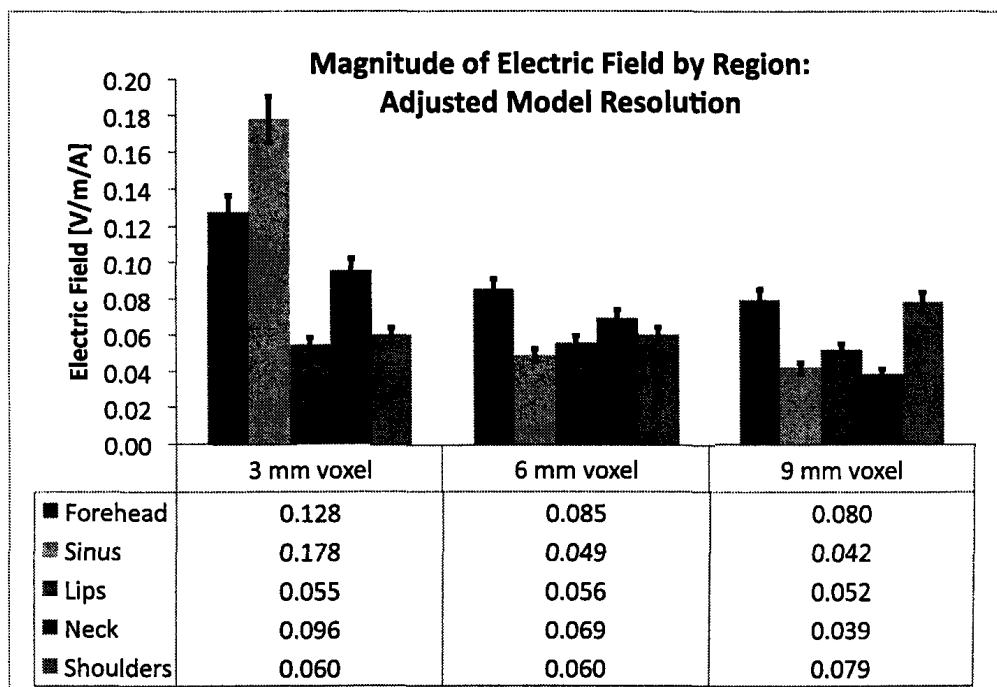
Fig. 2.5: Magnitude of the electric field produced by the head/neck gradient coil with the neck of the Visible Man Model positioned at the imaging region. The calculations were based on a 1-A-1-kHz-sinusoidal current waveform using isotropic voxel sizes of 3-mm (left), 6-mm (middle), and 9-mm (right).
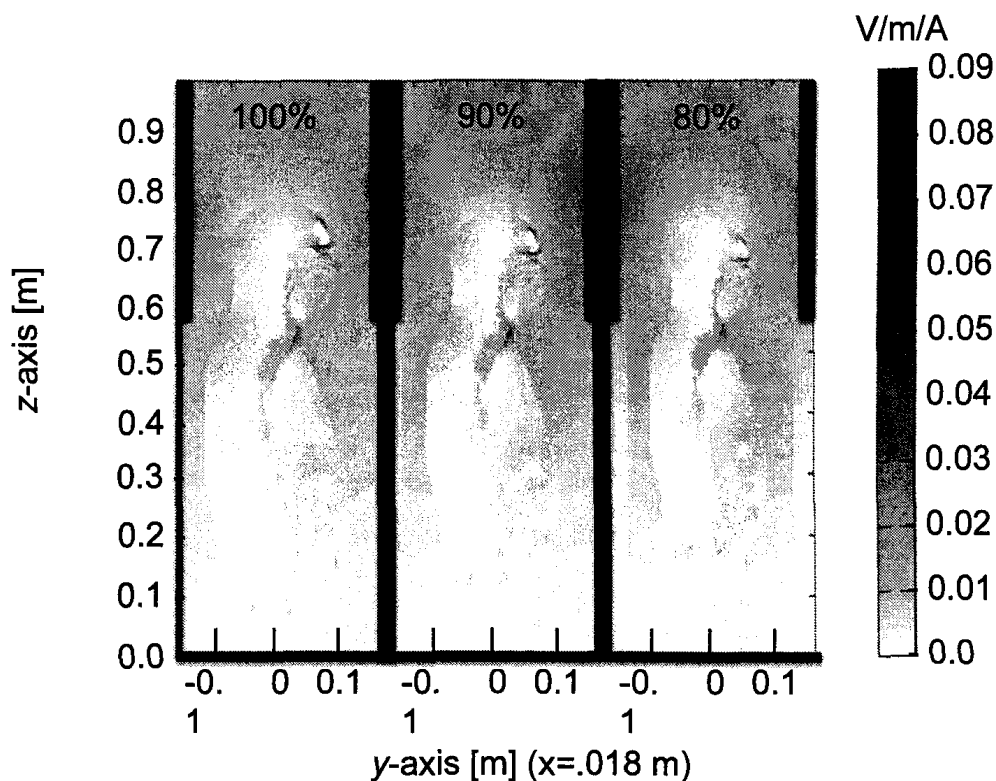
Fig. 2.6: Scaled models simulated in the electric field produced by the head/neck gradient coil. On the left is the 100% model (1.87 m height). The middle panel illustrates the electric fields for the 90% model (1.69 m height) while the final panel on the right panel displays the same results for the 80% model (1.5 m height). The models were positioned in neck imaging mode, with the chin aligned at the edge of the coil and the neck in the region of gradient linearity.

is the field for the model at 80%. Figure 2.6 demonstrates how the positioning of the model was adjusted with scaling to maintain the neck mode. Figure 2.6 also illustrates the pattern of induced electric field in all three models. The maximum electric field was 0.180 V/m at full size, 0.162 V/m at 90% and 0.142 V/m at 80%. The location of the maximum induced electric field within the model did not shift as the size of the model decreased.
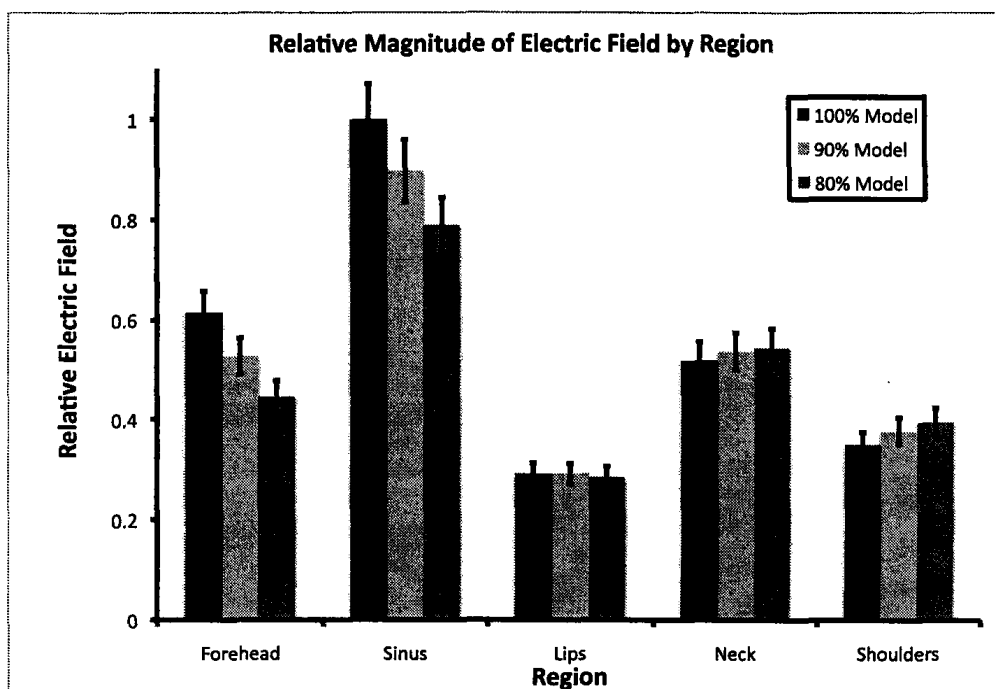
Fig. 2.7: Graph of electric field for configurations with reduced model size, normalized to the peak field in the sinuses for the 100% model size. Peak field was calculated for a 100% model (1.87m height)(left bar in each grouping), 90% model (1.69m height) (middle bar in each grouping) and 80% model (1.50m height) (right bar in each grouping). Error bars represent the range of electric fields iterated through during the simulation.

2.3.4 Model Position

The difference in electric field patterns due to model positioning is demonstrated in Figures 2.8 and 2.9. Figure 2.8 is an illustration of the electric field pattern at a current slew rate of 6283 A/s with the Visible Man Model in both neck and brain mode. Figure 2.9 details the magnitude of the maximum electric field for both regions. The maximum field in brain mode was a little higher (0.2051 V/m) than the maximum field in neck mode (0.1802 V/m). From the calculations of electric field (illustrated in Figure 2.9) and the measured aggregate stimulation threshold for both positions [22], the rheobase could be estimated. The calculated nerve rheobases were 6.09 ± 0.5 V/m in neck mode and 6.9 ± 0.6 V/m in brain mode.

2.3.5 Rheobase Calculations

The simulated current slew rate of 6283 A/s multiplied by the x- and y- gradient efficiencies resulted in a theoretical combined $x - y$ gradient slew rate of 3.34 mT/m/ms. To calculate $\vec{\kappa}(\vec{r})$ from Equation 2.4 the slew rate was combined with the results from the electric field simulation. For example, $\vec{\kappa}(\vec{r})$ for the sinus at the location of peak electric field (0.178 V/m) would be 0.0533 [V/m]/[mT/m/ms]. Given the SR_{min} of 74.1 ± 7.6 mT/m reported by Zhang et. al [12], the E_r would be 3.95 ± 0.25 V/m, assuming that the stimulation occurred in the sinus.

Finally, in an attempt to investigate the relationship between the relative magnitude of the induced electric field in the Visible Man and the stimulation locations in the subject population, the magnitude of the field in each region was plotted against the number of subjects reporting stimulation in that region during the stimulation experiments performed by Chronik et. al. [22]. The results are shown in Figure 2.10.
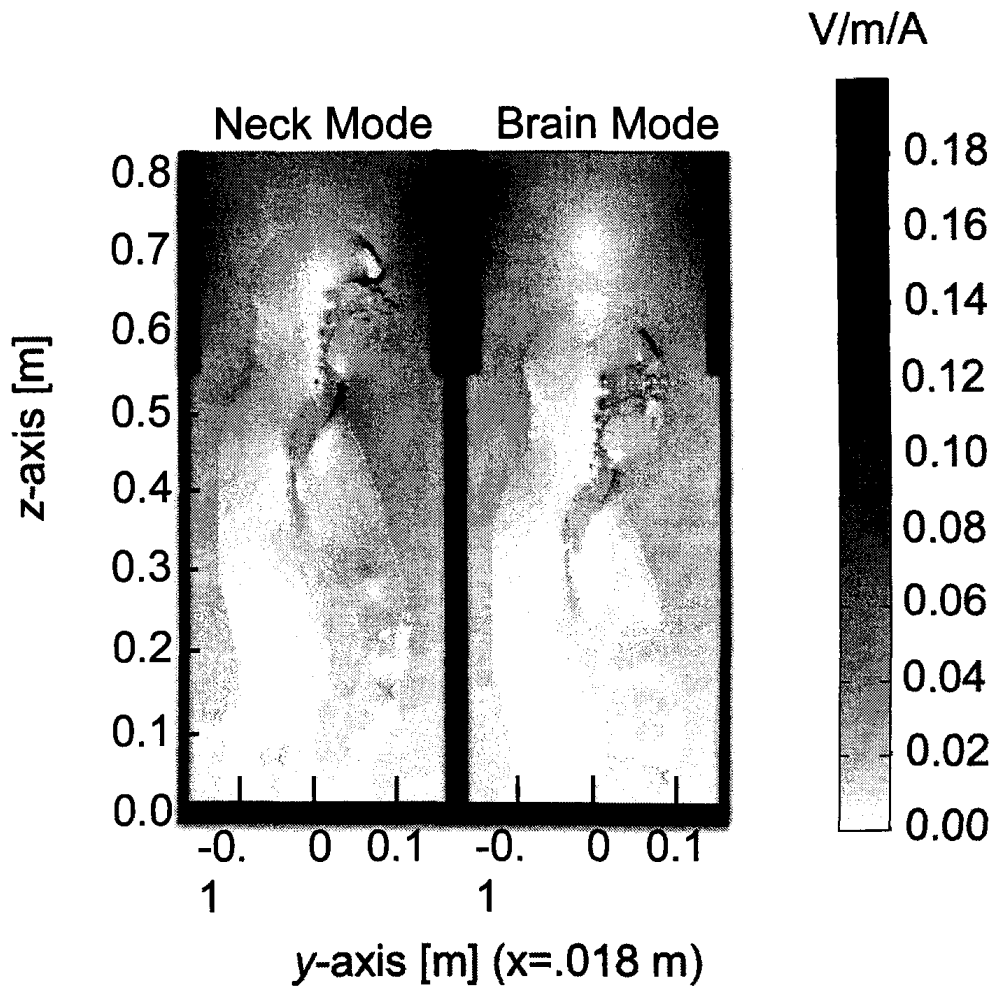
Fig. 2.8: Illustration of the effect of positioning upon electric field. The figure on the left depicts the model positioned in neck mode with the neck in the linear gradient region. The figure on the right illustrates brain mode positioning with the brain in the linear gradient region. Solid bars on the right and left of the model represent the location of the gradient coil.
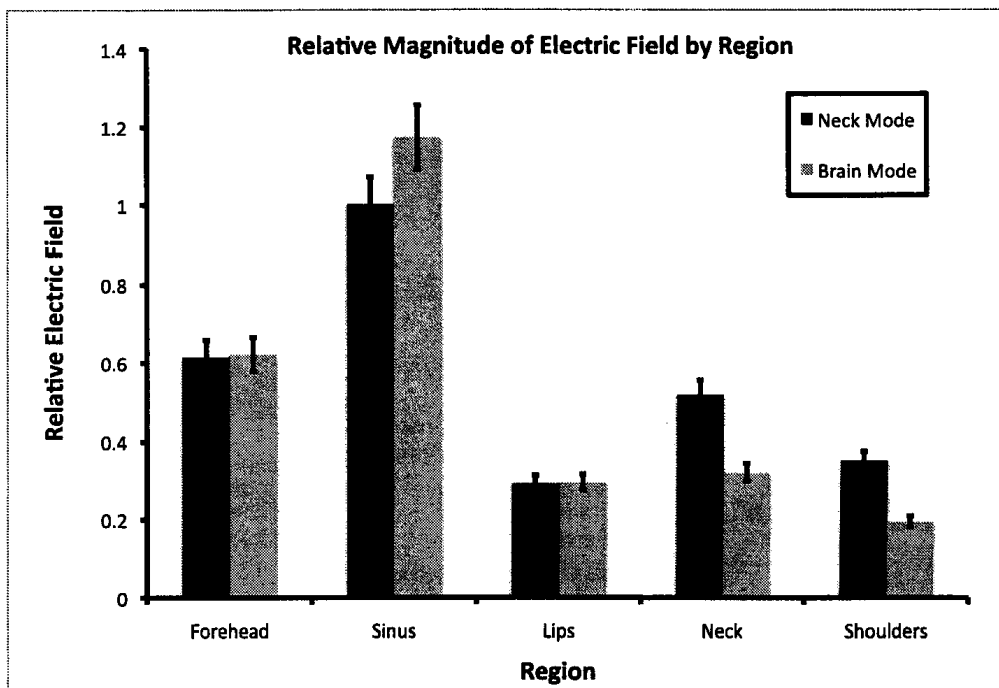
Fig. 2.9: Graph of normalized maximum electric field by anatomical region. In brain mode the model experienced higher electric fields in the forehead and sinus region and thus a higher electric field overall. In neck mode, the model experienced higher electric fields in regions more distant from the current elements such as the neck, and regions below the shoulders. The electric fields are reported as normalized to the peak electric field in the sinus region of the model in neck mode.
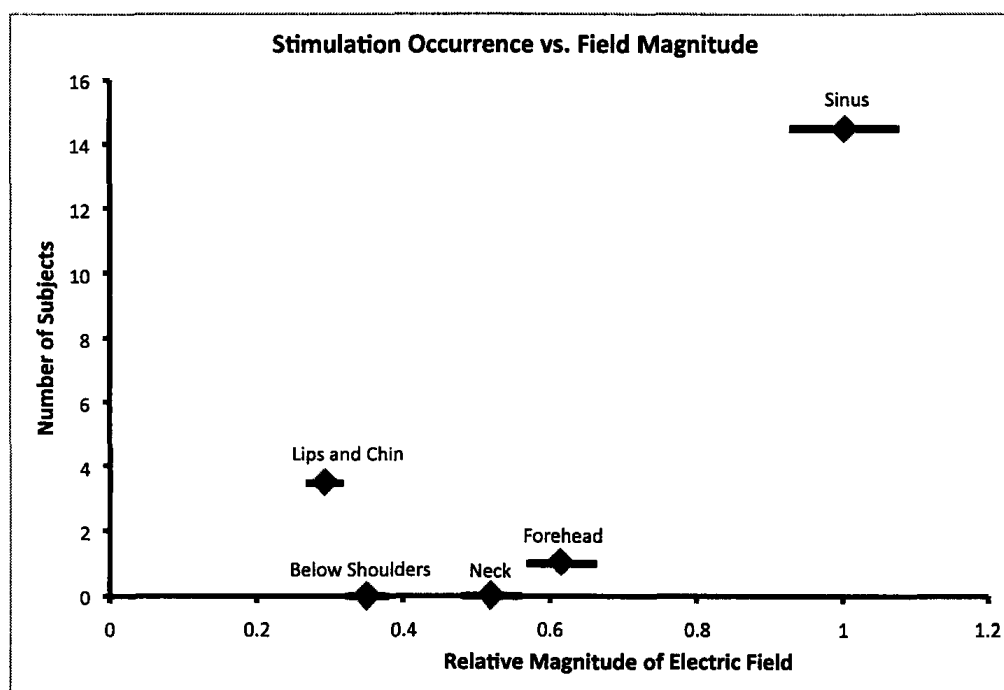
Fig. 2.10: Comparison of the relative magnitude of the peak regional field in the 3 mm model to the number of subjects reporting stimulation in that region. The electric fields are normalized against the peak electric field in the sinus region. The results plotted against the number of subjects reporting stimulation each region during an experiment. No significant trend was visible.

2.4   Discussion

Stimulation induced by this gradient system was reported to occur predominantly in the front of the head, in the vicinity of the sinuses, forehead and teeth. Qualitatively, the simulation images in Figures 2.6 and 2.8 suggested an explanation for this. Peak electric fields focused in and around the sinuses and mouth had a complicated pattern that seemed to correlate to the sharp curves of facial features and the air cavities of the sinus, mouth and trachea. With no air cavities (sinus) or surface irregularities (nose) in the posterior of the head, the amount of charge accumulation was lessened so that the minima and maxima of field were not as frequent or intense, potentially stimulating fewer nerves.

2.4.1   Minimum Resolution

The spatial irregularities in the air tissue boundary that induce peak electric fields diminished as the model resolution was decreased. From Figure 2.5 it can be seen that at 6-mm-voxel size, the magnitude of the peak field decreased by more than 50%, and at 9-mm-voxel size it decreased another 5%. More importantly, however, the location of the peak field changed with the choice of resolution. The 6-mm voxels were too large to effectively detail the complex sinus passages and internal air cavities of the human head, and even larger structures such as the trachea lost definition. So, the peaks in electric field due to those geometries were lost to the simulation, and the general location of the peak electric field changed from the sinus region to the forehead with coarser resolution. The peak field in the sinus region dropped by more than 65% with the larger voxel size.

2.4.2   Scale and Position

Figure 2.7 demonstrates that alterations in the overall size of the model accomplished by scaling did had moderate effects on electric field. The magnitude of the

field was decreased with scaling, but this was expected because the smaller model was exposed to a lower field due to the vector potential. The irregular surface boundaries of the front of the face and the sinuses, where charge accumulated, did not encounter the same magnitude of $\hat{n} \cdot \vec{E}_A$, so the net field was lessened. However the overall shape of the boundary, and thus the angle at which the field due to the vector potential intersected that boundary, remained the same. Qualitatively, the pattern of peak electric fields did not change due to scaling of the model and the peak electric field remained located in the sinus area. As well, the field due to scalar potential decreased proportionally to the amplitude of the field due to the vector potential alone when only model size was scaled. The magnitude of the field decreased about 10% for the 90% scale model and additional 11% (21% total) for the 80% scale model.

Altering the model's position affected the magnitude of the net induced electric field more than it affected the pattern of field extrema in the head, as can be seen in Figure 2.8. The change in location of the model's sinus and face boundaries from farther inside the coil towards the peak fields at the edge increased the magnitude of the peak fields by 17%. Figure 2.9 shows that, as with an alteration in model size, the location of the peak fields within the head did not change and the highest exposure remained in the sinus area.

2.4.3 Peak Fields and Stimulation

The rheobase calculations, based on the simulated electric fields, are similar to those predicted from a cable model of nerve stimulation [15]. Unfortunately, it is impossible to draw a direct correlation between the magnitude of the electric field in the Visible Man Model and the probability of stimulation. The attempt to link the two in Figure 2.10 demonstrated that although the location of peak field does correlate to the most frequent region of stimulation, no other connections can be made. Furthermore, the second and third most common locations of stimulation are not the forehead and

then the neck as might be expected from the peak fields. In experiments, the lips and teeth are the second most common location of stimulation, and buzzing in the scalp is the third [22]. This suggests that, although the simulations give some interesting and encouraging qualitative insight into peripheral nerve stimulation, quantitative prediction is still uncertain. Perhaps a greater variety of model geometries or models individualized to experimental stimulation subjects would provide the additional information required to predict stimulation, or possibly a more complex model than the nerve parameter model in Equation 2.2 is required.

2.5 Conclusions

A combination of the electric field simulation and nerve stimulation experiments permit a preliminary estimation of nerve rheobase. The simulations also suggest the most frequent site of stimulation may be the location of peak field on the Visible Man model. However, in order to predict the location of other points of stimulation, its not enough to simply locate the second highest field magnitude. Perhaps the evaluation of additional model geometries with, sufficient resolution, will allow these predictions.

References

[1] Nishimura DG. *Principles of Magnetic Resonance Imaging.* Stanford University, 1996.

[2] Schmitt F; Irnich W; Fischer H. *Physiological side effects of fast gradient switching,* volume Echo planar imaging theory, technique, and application of *215-233.* Springer –Verlag, 1998.

[3] Hoffmann A; Faber SC; Werhahn KJ; Jåger L; Reiser M. Electromyography in mri – first recordings of peripheral nerve activation caused by fast magnetic field gradients. *Magnetic Resonance in Medicine,* 43(4):534–539, 2000.

[4] Schenck JF. Safety of strong, static magnetic fields. *Journal of Magnetic Resonance Imaging,* 12(1):2–19, 2000.

[5] Schaefer DJ; Bourland JD; Nyenhuis JA. Review of patient safety in time-varying gradient fields. *Journal of Magnetic Resonance Imaging,* 12(1):20–29, 2000.

[6] Geddes LA. Accuracy limitations of chronaxie values. *IEEE Transactions in Biomedical Engineering,* 51(1):176–181, 2004.

[7] Plonsey R; Barr RC. Electric field stimulation of excitable tissue. *IEEE Transactions in Biomedical Engineering,* 42(4):329–336, 1995.

[8] King KF; Schaefer DJ. Spiral scan peripheral nerve stimulation. *Journal of Magnetic Resonance Imaging,* 12(1):164–170, 2000.

[9] Ham CLG; Engels JML; van de Wiel GT; Machielsen A. Peripheral nerve stimulation during mri: effects of high gradient amplitudes and switching rates. *Journal of Magnetic Resonance Imaging,* 7(5):933–937, 1997.

[10] Chronik BA; Rutt BK. A simple linear formulation for magnetostimulation specific to mri gradient coils. *Magnetic Resonance in Medicine*, 45(5):916–919, 2001.

[11] Chronik BA; Ramachandran M. Simple anatomical measurements do not correlate significantly to individual peripheral nerve stimulation thresholds as measured in mri gradient coils. *Journal of Magnetic Resonance Imaging*, 17(6):716–721, 2003.

[12] Zhang B; Yen YF; Chronik BA; McKinnon GC; Schaefer DJ; Rutt BK. Peripheral nerve stimulation properties of head and body gradient coils of different sizes. *Magnetic Resonance in Medicine*, 50(50-58), 2003.

[13] Harvey PR; Mansfield P. Avoiding peripheral nerve stimulation: Gradient waveform criteria for optimum resolution in echo-planar imaging. *Magnetic Resonance in Medicine*, 32(2):236–241, 1994.

[14] Hebrank FX; Gebhardt M. Safe-model – a new method for predicting peripheral nerve stimulations in mri. *Proceedings of the 8th Annual Meeting of ISMRM, Denver*, page 2007, 2000.

[15] Reilly JP. *Applied bioelectricity*. Springer-Verlag, New-York, 1998.

[16] Plonsey R; Heppner DB. Considerations of quasi-stationarity in electrophysiological systems. *Bulletin of Mathematical Biophysics*, 29:657–664, 1967.

[17] Wang H; Trakic A; Liu F; Crozier S. Numerical field evaluation of healthcare workers when bending towards high-field mri magnets. *Magnetic Resonance in Medicine*, 59(2):410–422, 2008.

[18] Liu F; Xia L; Crozier S. Influence of magnetically-induced e-fields on cardiac electric activity during mri: A modelling study. *Magnetic Resonance in Medicine*, 50(6):1180–1188, 2003.

[19] Mao W; Chronik BA; Feldman RE; Smith MB; Collins CM. Consideration of magnetically-induced and conservative electric fields within a loaded gradient coil. *Magnetic Resonance in Medicine*, 55(6):1424–1432, 2006.

[20] MI Ackerman. Viewpoint: The visible human project. *Journal of Biocommunication*, 18(2):14, 1991.

[21] Chronik BA; Alejski A; Rutt BK. Design and fabrication of a three-axis edge rou head and neck gradient coil. *Magnetic Resonance in Medicine*, 44:955–963, 2000.

[22] Chronik BA; Rutt BK. A comparison between human magnetostimulation thresholds in whole-body and head/neck gradient coils. *Magnetic Resonance in Medicine*, 46:386–394, 2001.

Chapter 3

Peripheral Nerve Stimulation Experiment

3.1   Introduction

Stronger, more rapidly switched gradient fields are desirable in magnetic resonance imaging (MRI) because they can be used to reduce imaging time, increase image resolution, improve image signal-to-noise ratios, or provide a combination of all three of these benefits [1]. Improvements in gradient strength can be made by increasing the strength of the gradient amplifier or by improving the efficiency of the gradient coil. Simply increasing the gradient amplifier strength is not always possible as the rapidly changing magnetic fields produce electric fields [2] [3], and in tissue these fields can cause undesirable peripheral nerve stimulation (PNS) [4] [5] [6] [7] [8]. This motivates the pursuit of new gradient coil configurations that allow improved gradient performance while avoiding PNS. The thresholds of human nerve stimulation of a planar gradient system, which has been shown to improve gradient strength and switching time for localized applications such as cardiac imaging [9] [10], are reported in this chapter. These results may serve to guide the design of future high performance gradient systems that minimize unwanted nerve stimulation.

Nerve stimulation due to switched gradients was predicted early in the development of MR technology [11], and later demonstrated to occur [12]. Safety agencies have issued guidelines regarding exposure to time varying magnetic fields [13] [14].

3.1.1   Peripheral Nerve Stimulation Models

A few models have been developed to describe and predict nerve stimulation, including an exponential model [15] and a hyperbolic model [16]. The hyperbolic model leads to a simple, linear formulation of stimulation thresholds in terms of gradient strength and slew rate [17] that has agreed well with previous experiments, and is used here to analyze the data.

The theory of PNS is developed by adding the effects of externally generated electric fields, present during gradient switching, to the standard physiological cable theory of action potential initiation and propagation along electrically excitable cell membranes [15] [16] [17] [18].

From the hyperbolic model, the magnitude (E_{stim}) of the induced electric field at the stimulation threshold is related to the duration τ of that field as Equation 3.1:

$$E_{stim} = E_r \cdot (1 + \frac{\tau}{\tau_c}) \qquad (3.1)$$

In Equation 3.1 the nerve rheobase, E_r, is the minimum electric field required to cause stimulation and the nerve chronaxie time, τ_c, describes the shape of the stimulation threshold curve. For a pulse duration $\tau = \tau_c$, the stimulation threshold is twice the rheobase.

Although this model is theoretically independent of the effects of gradient wire pattern, it can be difficult to implement a prediction of stimulation thresholds during gradient operation because of the difficulty in determining the electric field produced

by the combination of gradient wire pattern and subject geometry, as was shown in the last chapter.

Following from the electric field model, a linear stimulation threshold, [17], can be derived that describes the gradient change required to produce nerve stimulation, ΔG_{stim}, in terms of MRI pulse sequence parameters. Equation 3.2 describes this model.

$$\Delta G_{stim} = \Delta G_{min} + SR_{min} \cdot \tau \tag{3.2}$$

The time over which the gradient is varied is τ. SR_{min} is the slope of the linear threshold curve and is the minimum change in gradient per unit time required to cause stimulation. The intercept (ΔG_{min}) is the minimum change in gradient strength required to cause stimulation, regardless of the slew rate. This simple model has been verified experimentally in several studies [19] [20] [21].

3.1.2 Equivalence of Nerve Stimulation Models

The linear (gradient) model and the hyperbolic (electric field) model, are directly related. An estimate of the electric field rheobase is difficult because it would require a complex calculation of the field cause by the changing magnetic field and the interaction with the conducting matter inside the field. However, to estimate the chronaxie time from experimental data, a conversion from the pulse sequence parameters can be done. It can be shown [17] that the chronaxie time is the ratio of the two pulse sequence parameters ΔG_{min} and SR_{min}.

$$\tau_c = \frac{\Delta G_{min}}{SR_{min}} \tag{3.3}$$

Chronaxie times are expected to be similar across different gradient coil PNS experiments, to the extent that similar nerve populations are experiencing stimulation [22]. For that reason, it is important to compare chronaxie time values obtained in planar gradient coil experiments to those reported in different coil configurations.

The experimentally determined values of ΔG_{min} and SR_{min} are expected to vary significantly for different gradient coil designs [18] [23] [19] [20] [21] [24]. Because the stimulation threshold curve described by Equation 3.2 defines the limits of safe gradient coil operation, the experimental determination of this curve is important for all new gradient coil designs. To have an accurate picture of the range within which a gradient can be safely operated, thresholds need to be determined experimentally for each new design. While there are several reports of PNS thresholds for large, whole-body gradient systems [24] [25] [26], there are few studies of PNS thresholds for customized gradient coils [24] [27], and none have addressed these thresholds for planar gradient configurations.

3.2 Methods

All experiments were conducted using a planar gradient system powered with a switching amplifier capable of providing 320A and 1500V. The performance parameters for the gradient set, as reported in [9], are summarized in Table 3.1. The field of view (FOV) quoted in Table 3.1 is the range through which a 2D-unwarping algorithm can be applied and corresponds to a gradient change of about 50%. Each axis was constructed on a plane totaling 42 cm wide (x-direction) and 60 cm long (z-direction). Further details regarding the imaging performance of this gradient system are given in a previous publication [9].

The experiments were conducted with the gradient coil outside the bore of the scanner, in Earth's ambient magnetic field. This greatly reduced noise produced by

	x-axis	y-axis	z-axis
ΔG_{max} [mT/m] at 5 cm from surface	170	230	325
η Gradient Efficiency [mT/m/A]	0.53	0.72	1.02
L [μH]	472	858	922
Minimum rise time [μs]	90	160	170
FOV [cm]	30	20	30

Table 3.1: Parameters for prototype planar gradient system.

the operation of the gradient system such that subjects typically could not hear them at all during operation. However, subjects could hear the gradient amplifiers and from that deduce the timing of the current waveform. For this reason, all subjects wore hearing protection to limit auditory feedback during the experiment.

Experiments were conducted in two different sessions, approximately 10 months apart. In the first session, PNS thresholds were measured for the z-axis only. In the second session, PNS thresholds were measured for the x- and y- axes. These experiments are described separately in the paragraphs below.

3.2.1 z-axis experiments

Fourteen healthy normal human subjects were recruited to participate in the evaluation of the z-axis. The gender, height, and weight of subjects are listed in Table 3.2. All subjects were employees of General Electric and displayed no obvious anxiety regarding the experiment. Institutional ethics approval and subject consent were obtained in all cases.

The first stage in the experiment was to identify a location of maximum stimulation (i.e. minimum threshold) for the subject. Individual subjects were positioned supine over the gradient set, knees slightly bent, as pictured in Figure 3.1. Initial subject placement was with waistline approximately at the origin of the z-axis. An oscillating

	z-axis			x-axis and y-axis		
	Male	Female	All	Male	Female	All
# of Subjects	11	3	14	15	3	18
Weight Range [kg]	70-104	54-73	54-104	63-102	59-70	59-102
Average Weight [kg]	78	64	76	78	67	76
Std. Dev. [kg]	11	6	13	11	6	12
Height Range [cm]	160-168	157-168	157-198	170-193	167-170	167-193
Average Height [cm]	183	163	180	180	169	178
Std. Dev. [cm]	10	5	13	8	2	8

Table 3.2: Summary of subjects included in the determination of the z-axis planar gradient peripheral nerve stimulation threshold.

trapezoidal pulse train of 256 lobes, with rise time of 170 μs and flat-top duration of 1000 μs was applied once every second. The initial gradient strength was set at 160 mT/m, or 50% maximum. If the subject failed to experience stimulation under these conditions, the amplitude of the pulse train was adjusted by increasing the magnitude of the gradient amplitude in steps of 25 mT/m, until PNS was experienced. The pulse train was then applied continuously at that strength and the subject was asked to adjust his position along the z-direction until the sensation was maximized. The subject was asked to describe the nature and anatomical location of stimulation. A photograph was taken documenting the position of the subject and the location of stimulation. The subject was asked to remain in this position for the duration of the experiment.

The pulse sequence for the threshold curve experiment used the same train of 256 oscillating trapezoids with a fixed rise time as was used for the localization phase, but with variable amplitude. Specifically, the gradient amplitude was stepped from zero to maximum in 32 steps. The pulse train was applied 4 times at each step with a repetition time of 1 second between applications. The subjects were instructed to report stimulation when they considered it to be definite. The sequence was then stopped immediately, and the gradient amplitude for that rise-time was recorded.
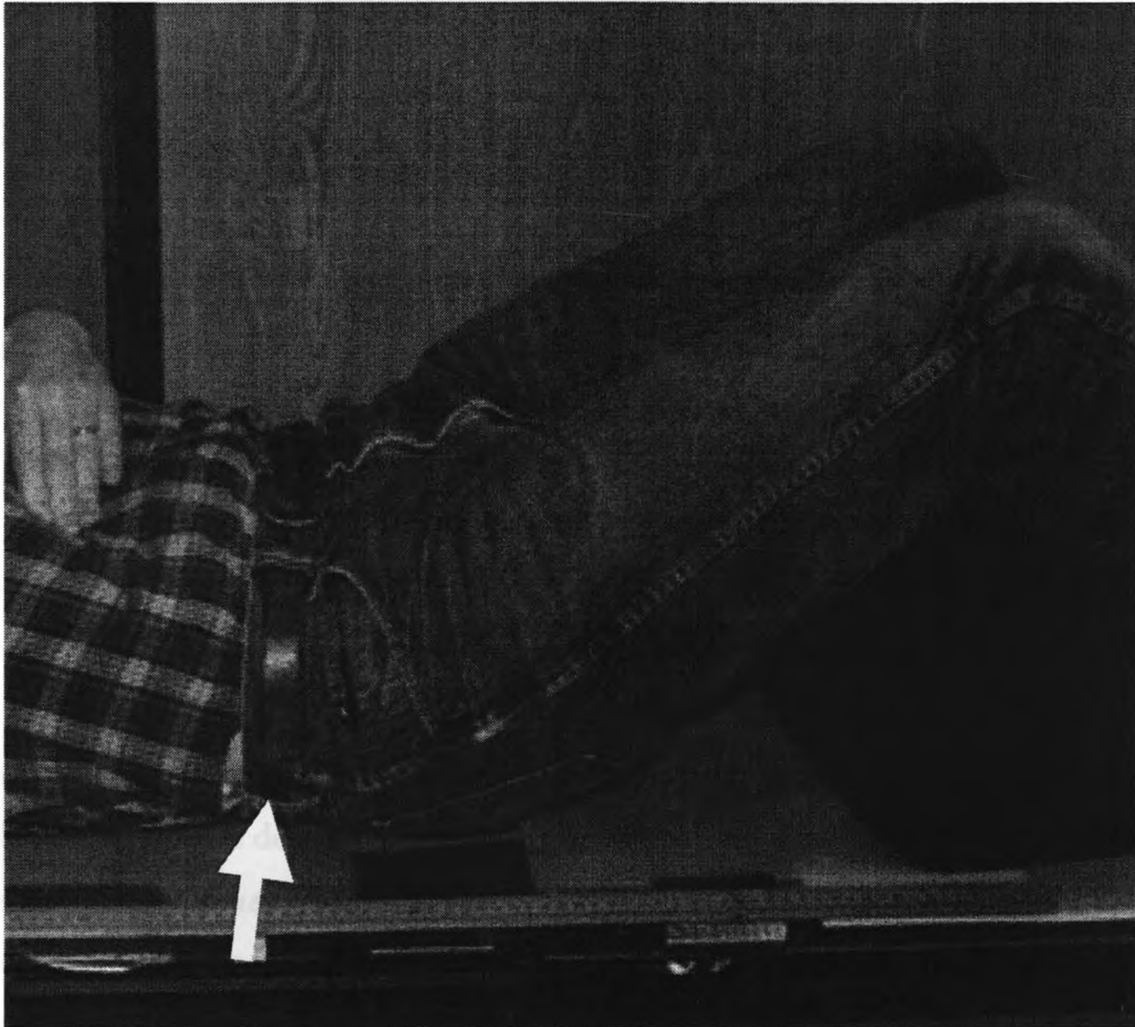
Fig. 3.1: Subjects were asked to lie on the planar gradient coil with their belt approximately at the centre of the coil (white arrow), and knees bent. They then adjusted their position to maximize the perceived stimulation

This process was repeated for a selection of rise-times ranging in random order from 20 μs to 1400 μs. Between 10 and 18 threshold points were recorded. Thresholds for rise-times at the edges of the detectable range were tested multiple times for consistency. The entire procedure for a single subject required between 45 minutes and 1 hour.

3.2.2   x- and y- axis experiments

The x- and y- axis experiments were performed 10 months after the z- axis experiments. A different set of subjects was used. 18 subjects participated in the testing of the x- and y- axis, and 8 of those subjects were common to both experimental sessions. The localization and threshold determination procedures were identical to the z-axis experiments with the following modifications.

The localization procedures were performed using x- and y-axes simultaneously with a net gradient strength of 146 mT/m. If an increase in strength was required, the increment size was 17 mT/m. This procedure was performed once and the position was maintained for both the x- and y- axis threshold determinations. The threshold curves were determined for trapezoidal pulse trains with rise-times sampled between 50 and 700 μs. There were 15 trials per axis with between 3 and 9 rise times investigated for each curve. Some repetition in rise-time values occurred so that an experimental determination of variability in threshold perception could be made. The entire procedure required between 45 minutes and 1 hour.

3.2.3   Variations in individual threshold determinations

To gauge the variability in threshold reporting for individual subjects, the first 6 subjects in the x- and y- axis experiments were exposed to a limited number of distinct rise times, with more repetitions at each point. These 6 subjects were exposed to 5 repetitions of pulse sequences with rise times of 170 μs, 300 μs, and either 250 μs

(x-axis), or 600 μs (y-axis). The standard deviation in the 5 measurements at each rise-time allowed the estimation of uncertainty for the threshold measurements. The assumption was made that this uncertainty estimate was applicable to all experiments. The remaining 12 subjects were exposed to pulse sequences with rise times of 50 μs (3 repetitions), 100 μs, 170 μs, 250 μs (3 repetitions), 300 μs, 400 μs, 500 μs, 600 μs, and 700 μs. The longest rise time in the series causing stimulation was repeated an additional 2 times.

3.2.4 Curve Fitting

Two methods were used to analyze the data points and produce a mean threshold. The first method was the calculation of an average from the individual fits. The second method determined a curve based on the population average stimulation threshold, calculated by logistic regression [28] where necessary, for each rise time.

Individual threshold curves of the form of Equation 3.2 were fit to each subject's dataset to characterize individual threshold curves. For each subject, both the slope and the intercept were extracted from the fit. These values were also used to calculate a chronaxie time via Equation 3.3 for each subject. A reduced chi-squared value was calculated for each fit. If multiple measurements were obtained for any give rise time, the uncertainty was taken to be the calculated standard deviation of those measurements. If multiple measurements were not made for a rise time, the average standard deviation obtained from the first 6 subjects in the x- and y- axis experiments was used.

An aggregate stimulation threshold curve was constructed using data from all the subjects. Uncertainty for each rise-time was taken to be the standard deviation of the subject thresholds at that rise-time. Not all subjects stimulated prior to reaching the machine limits for longer rise-times, so logistic regression [28] was used for the

analysis of these time points to determine a mean and standard deviation. A 50% inclusion standard was applied to the data, such that for any given rise-time, if fewer than 7 of the 14 subjects (z-axis) or fewer than 9 of the 18 subjects (x- and y-axis) reported stimulation, the data for that rise-time would not be included in the calculation of the aggregate threshold curve. From the aggregate threshold curve data, the population average SR_{min} and ΔG_{min} were extracted using logistic regression, along with uncertainties in these parameters. The ratio of the parameters extracted from the fit was used to calculate an estimate chronaxie time and uncertainty.

3.3   Results

3.3.1   Qualitative Description of Peripheral Nerve Stimulation

Stimulation during z-axis operation was reported on the surface of the lower back and tailbone, or deeper in the abdomen and near the base of the ribcage. One subject reported stimulation as a twitch in the shoulder. Three subjects reported stimulation as tingling or pin pricks, 4 reported the sensation as pressure, a throb, pulse or tap, and 7 reported the stimulation as a muscle contraction or twitch. During z-axis operation, the most common manifestation of stimulation was reported as a twitch in the abdomen, below the ribcage (6 subjects).

Stimulation during x-axis and y-axis operation was typically reported in the lower-to-mid back or abdomen. One subject reported stimulation in the thigh during y-axis operation. For all other subjects, stimulation was mostly centered in the middle of the back or experienced simultaneously on both the right and left side, and was described as: a tingle (x-axis:11 subjects, y-axis:8 subjects), pressure (x-axis:4 subjects, y-axis:3 subjects), or twitch (x-axis:3 subjects, y-axis:5 subjects). The most common mode

of stimulation was a tingle in the middle of the lower back.

3.3.2 Nerve Stimuluation Thresholds

The first 6 subjects of the x- and y- axis experiment demonstrated an average variability in the reporting of stimulation thresholds of 16 ± 2 mT/m on the x- axis and 15 ± 2 mT/m on the y- axis. The remaining subjects demonstrated an average variability in the reporting of stimulation thresholds of 18 ± 4 mT/m on the x-axis and 14 ± 4 on the y-axis.

Every subject reported stimulation for multiple rise-times, so a threshold curve was obtained for all subjects on all axes. The reduced chi-squared for the stimulation thresholds of the y-gradient axis fell between 0.54 and 2.55 with an average value of 0.71. There was a single exception on the y-axis of a fit with a reduced chi-squared value of 17.72. On the x-axis, there were two abnormally high chi-squared values (18.5 and 8.3). The remaining fits produced values between 0.50 and 2.71 with a mean of 1.18. The z-axis produced 3 abnormally high chi-squared calculations (381.55, 30.07, and 12.56) with the remaining falling between 0.46 and 1.76 with a mean of 1.34.

Figure 3.2 is a graph of ΔG_{stim} ($+G_{max} - (-G_{max}$)) versus switching time τ (time required to move from $-G_{max}$ to $+G_{max}$)for two example subjects, for switching times between 100 and 1400 μs. The straight line through each data set is the linear best fit of a stimulation threshold based on those individual threshold points. Figure 3.3 is a plot of the ΔG_{min} values for all subjects calculated from the individually fit threshold curves. The median and mean ΔG_{min} were: 201 mT/m and 213 ± 13 mT/m, respectively, for the z-axis, 121 mT/m and 118 ± 4 mT/m for the x-axis, and 115 mT/m and 114 ± 3 mT/m for the y-axis. There was a significant difference between the z-axis ΔG_{min} and the intercept values calculated for both the x- and y-axes. Figure 3.4 is a plot of the SR_{min} calculated from the individual threshold curves.
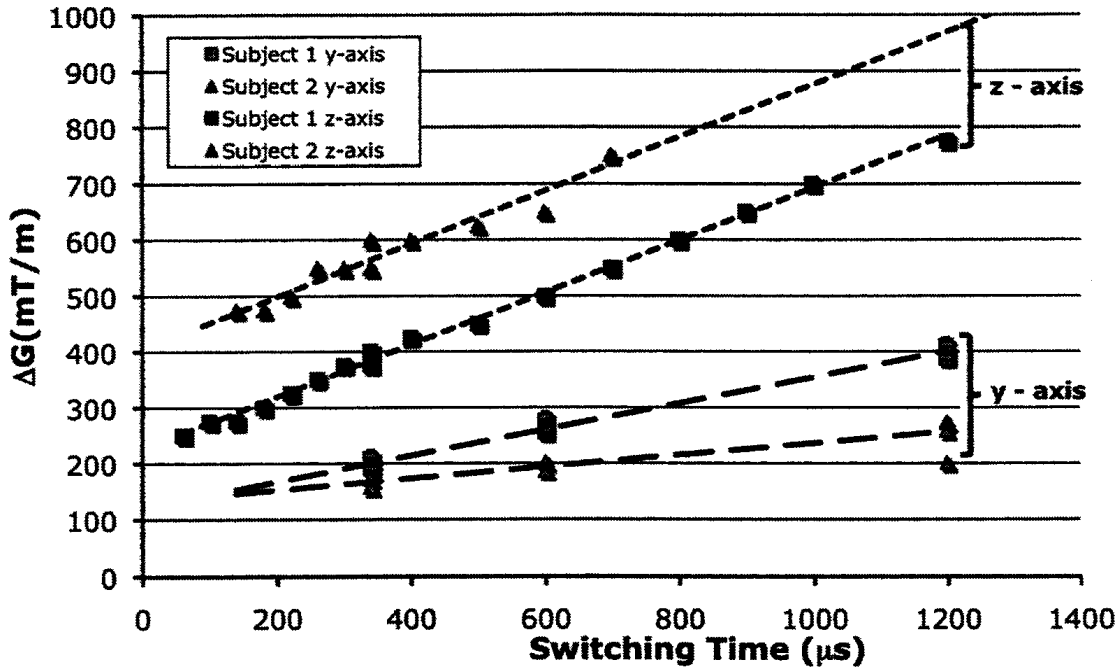
Fig. 3.2: For each subject the threshold of stimulation was plotted against the rise time for 2 gradient axes. The graph shows the results for 2 subjects for both the y- and z- axis. A straight line was fit to each data set. Subject 1 (square markers) reported threshold higher than subject 2 (triangular markers) on the y-axis, but lower than subject 2 on the z-axis. This demonstrates that high thresholds are not necessarily a function of the individual subject along, but a combination of the subject and applied gradient.

The median and mean SR_{min} values were: 303 mT/m/ms and 250 ± 32 mT/m/ms, respectively, for the z-axis, 189 mT/m/ms and 195 ± 16 mT/m/ms for the x-axis, and 180 mT/m/ms and 169 ± 14 mT/m/ms for the y-axis. There were no significant differences between the mean slopes reported for each axis.

The same analysis was repeated after removing subjects with reduced chi-squared fits greater than 7. The resulting mean ΔG_{min} and SR_{min} were 204 ± 4 mT/m and 284 ± 10 mT/m/A, respectively, for the z-axis, 116 ± 1 mT/m and 209 ± 4 mT/m/A for the x-axis, and 115 ± 1 mT/m and 176 ± 3 mT/m/A for the y-axis. These values
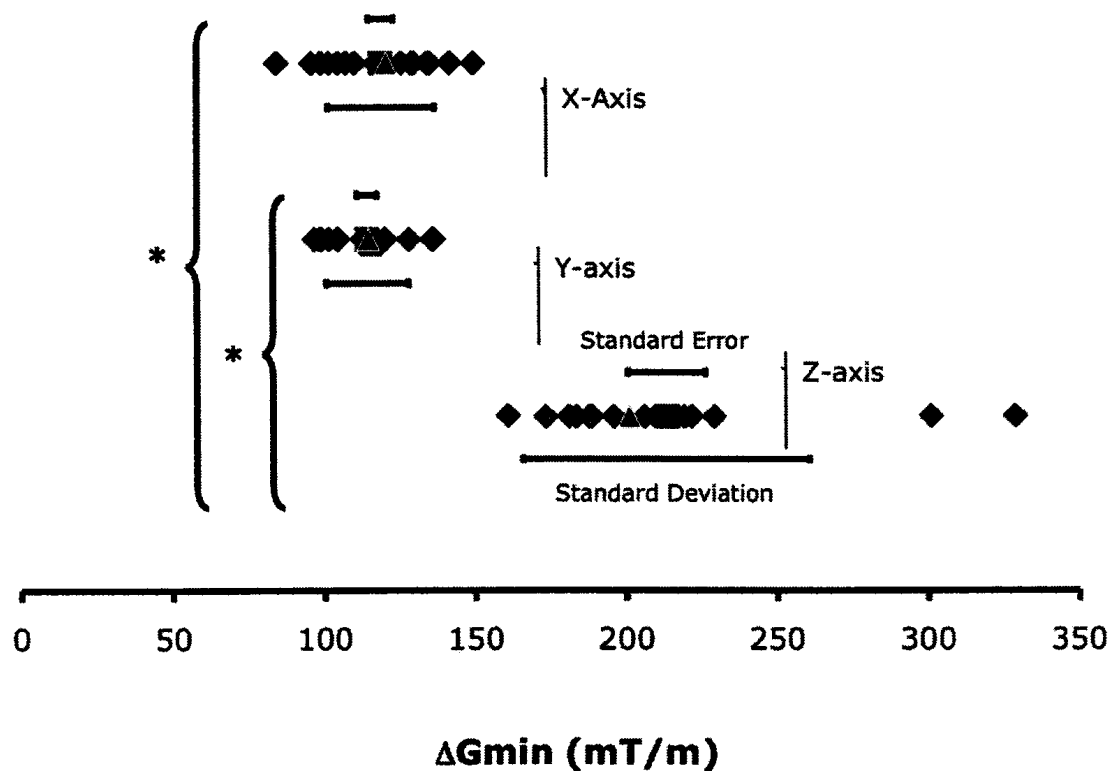
Fig. 3.3: The distribution of the minimum change in gradient strength for all three axes. The top set represents the data from the x-axis, the middle set represents the data from the y-axis and the bottom set represents the data from the z-axis. The top bar in each set represents the standard error, and the bottom bar represents the standard deviation. The square represents the average and the triangle the median value. Sets marked with an asterix (*) highlight a significant difference between the grouped axes (P≤ 0.01).

Fig. 3.4: The distribution of the minimum slew rate for all three axes. The top set represents the data from the x-axis, the middle set represents the data from the y-axis and the bottom set represents the data from the z-axis. The top bar in each set represents the standard error, and the bottom bar represents the standard deviation. The square represents the average and the triangle the median value. There was no significant difference between the axes.

were not significantly different than those obtained without exclusion of the outliers. However, removing the outliers reduced the size of the error bars and this resulted in the calculation of a significant difference in SR_{min} between all 3 axes (P $\leq$ 0.001) as well as maintaining the significant difference in ΔG_{min} between the x- and z- axes and the y- and z- axes.

Figure 3.5 shows the distribution of calculated chronaxie times. Chronaxie times were only computed for subjects with sufficiently good fits (i.e. with reduced chi-squared values of less than 7 as described above). The median and mean chronaxie times were 589 μs and 713 $\pm$ 27 μs, respectively, for the z-axis (N = 11), 560 μs and 575 $\pm$ 7 μs for the x-axis (N = 16), and 658 μs and 697 $\pm$ 11 μs for the y-axis (N = 17).

Figure 3.6 shows the aggregate stimulation threshold curve calculated by logistic regression. The aggregate ΔG_{min} and SR_{min} values were: 218 $\pm$ 22 mT/m and 252 $\pm$ 26 mT/m/ms, respectively, for the z-axis, 147$\pm$17 mT/m and 222 $\pm$ 24 mT/m/ms for the x-axis, and 133 $\pm$ 13 mT/m and 210 $\pm$ 18 mT/m/ms for the y-axis. Given the standard error in the logistic regression calculation, the linear fits produced reduced chi-squared values of 0.85, 0.28, and 0.58, for the x-, y-, and z- gradient axes respectively. The aggregate stimulation thresholds for a customized head gradient coil and a full body gradient coil [27] are also shown on Figure 3.6 for comparison. The stimulation thresholds measured for the planar coils in the present experiment are significantly higher than those reported for these other coil designs.

3.4 Discussion

To the best of our knowledge, this work represents the first experimental PNS threshold measurements for any non-cylindrical gradient system. At comparable gradient switching times, the PNS thresholds of the planar gradient system are sig-
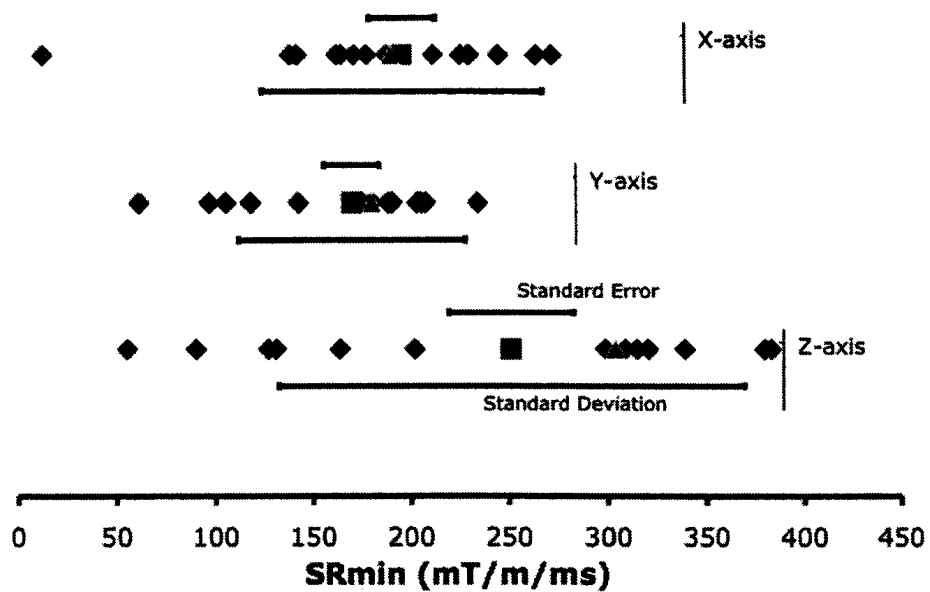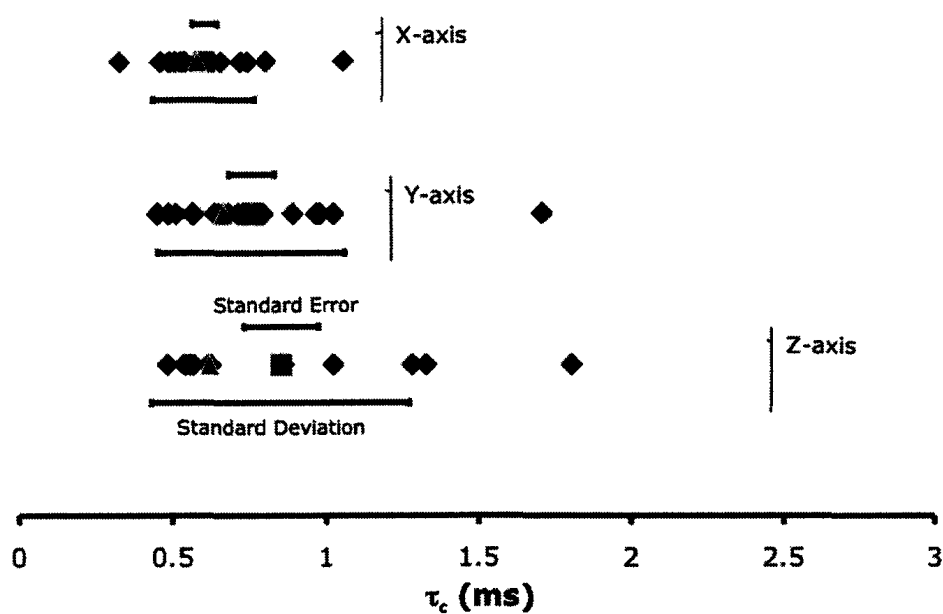
Fig. 3.5: The distribution of chronaxie time for all three axis. The top set represents the data from the x-axis, the middle set represents the data from the y-axis and the bottom set represents the data from the z-axis. The top bar in each set represents the standard error, and the bottom bar represents the standard deviation. The square represents the average and the triangle the median value. There was no significant difference between the axes.
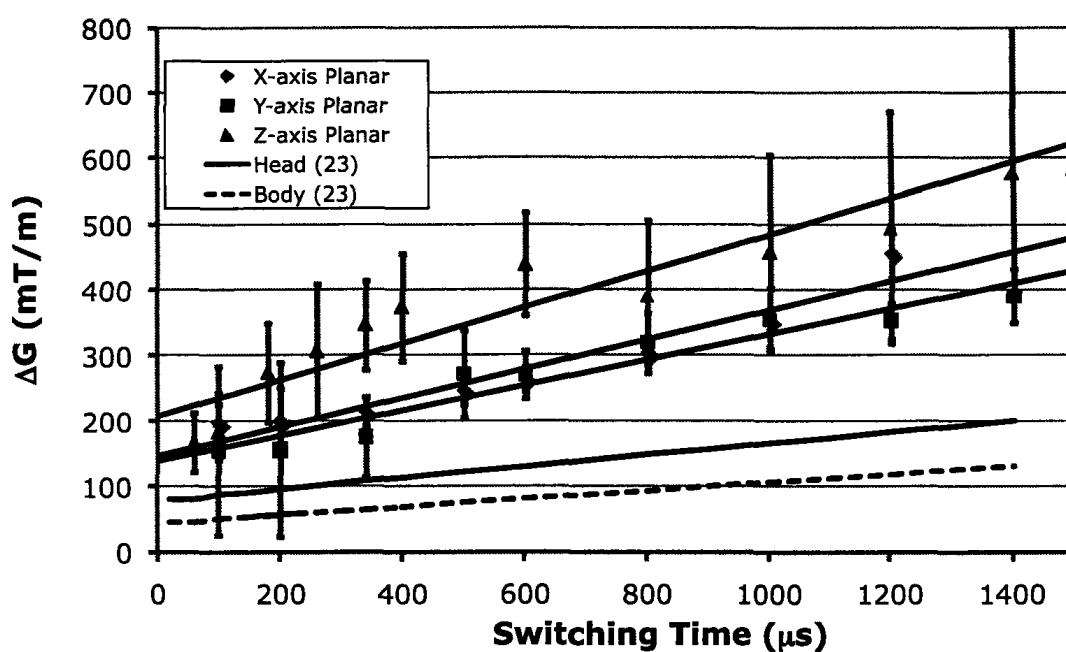
Fig. 3.6: A mean threshold was calculated for each time point. For rise times where not all subjects stimulated, logistic regression was used to calculate the mean. Error bars are the standard deviation about the mean and represent the standard deviation of the population stimulation threshold at that rise time. Head and body comparison data has been previously published by Zhang et. al.

nificantly higher than those of either a standard whole-body or a customized head gradient coil for all measured axes and rise-times [27]. Although the head gradient coil [24] has a FOV of 21 cm which is comparable to the FOV of the planar coils used in this experiment, typical whole-body gradient systems have uniform FOVs that are much larger (typically 40 to 50 cm). In order to make a fair comparison, the improved threshold performance of the planar system must be balanced by the reduced imaging region size and increased non-uniformity of the gradient field. Methods for dealing with the performance issues of this planar gradient system have been discussed previously [9].

Individuals exhibit different stimulation thresholds as illustrated in Figure 3.2. These differences exist not only from subject to subject, but also across axes. A subject with a high stimulation threshold, relative to the subject population, on the z-axis may not have a correspondingly high threshold on the y-axis. Previous work has shown stimulation thresholds do not seem to correlate with any simple anatomical measurements [20], and the rough, self-reported, accounting of height and weight used in this study seems to confirm that finding. It is possible that the stimulation threshold differences may be accounted for by the interaction of the electric fields with the interface between the subject and the surrounding air, however that possibility has not yet been fully explored.

When the data from the subject groups is combined there are significant differences between the aggregate stimulation thresholds of the different axes of the planar gradient coil as summarized in Table 3.3. Overall, the z-axis demonstrated the highest thresholds and the y-axis demonstrated the lowest. This result is not surprising given that the planar y-gradient must be designed such that the entire surface area of the back is exposed to the strongest magnetic fields, thus the strongest induced electric fields. The observed differences between the axes of the planar gradient system could

	Average of all linear fits		Average of linear fits (w/o outliers)			Linear fit through average thresholds (linear regression)		
	ΔG_{min} [mT/m]	SR_{min} [mT/m /ms]	ΔG_{min} [mT/m]	SR_{min} [mT/m /ms]	τ_c [ms]	ΔG_{min} [mT/m]	SR_{min} [mT/m /ms]	τ_c [ms]
x-axis mean $\pm$SE	118 $\pm$4	195 $\pm$16	116 $\pm$1	209 $\pm$4	575 $\pm$7	147 $\pm$17	222 $\pm$24	659 $\pm$104
y-axis mean $\pm$SE	114 $\pm$3	169 $\pm$14	115 $\pm$1	176 $\pm$3	697 $\pm$11	133 $\pm$13	210 $\pm$18	632 $\pm$193
z-axis mean $\pm$SE	213 $\pm$13	250 $\pm$32	204 $\pm$4	284 $\pm$10	713 $\pm$27	218 $\pm$22	252 $\pm$26	866 $\pm$125

Table 3.3: Summary of PNS threshold parameters

be taken into account when optimizing pulse sequences used with the system. For example, consider an EPI pulse sequence utilizing a zero to maximum rise time of 250 μs (switching time of 500 μs). Stimulation would be expected to occur on average for a maximum gradient strength of 172 ± 18 mT/m on the z-axis of the planar gradient, which corresponds to a slew rate of 688 T/m/s. For the x-axis stimulation would occur for a maximum gradient strength of 129 ± 15 mT/m and slew rate of 516 T/m/s, while using the y-gradient axis would permit a maximum gradient of 119 ± 11 mT/m and slew rate of 476 T/m/s. These values, in particular the slew rates, are substantially higher than what is typically possible for use with whole-body systems [24] [27].

Although the experimental PNS threshold curves were found to be higher for the planar gradient than for other types of gradient coils, the calculated nerve parameters compare well to literature values. The chronaxie time estimates, based on the aggregate x-, y-, and z- gradient thresholds, were 659 ± 104 μs, 632 ± 193 μs, and $866 \pm$

125 μs respectively. All three of these values fall within the range of chronaxie times obtained in other gradient PNS experiments, where values ranging between 400 μs and 1100 μs have been reported [22] [24] [26] [5] [29] [30] [31]. This result is generally expected given that the chronaxie time is a nerve-specific parameter, and therefore should be independent of the gradient coil design.

Zhang et. al. [24] discussed the possibility of an inverse linear relationship between the imaging region and slew rate, ΔG_{min}, and chronaxie time. Thus a smaller FOV would result in a higher stimulation threshold. This experiment demonstrated an elevated threshold that corresponded with the decreased maximum FOV. However, the stimulation threshold measured in this experiment is higher than what would have been deduced from the inverse linear relationship suggested by Zhang. This is most likely due to the planar design of this gradient set. Further studies are necessary in order to be better able to compare thresholds between gradient coils of very different geometry.

The average subject sensitivity to reporting peripheral nerve stimulation (16.5 mT/m) was approximately the size of the step used in between one level of gradient amplitude and the next (15.6 mT/m). For the repeated switching-time measurements, 2 subjects displayed no variability in the reported threshold data, repeatedly reporting at the same level, regardless of the rise time tested. The majority of subjects reported thresholds that varied by no more than 2 steps. In one case a subject showed a variability of 5 steps on repeated tests. This suggests that, for at least some of the subjects, improved fits could have been obtained by reducing the step size, and decreasing the reading error in the measurement. However, that level of precision in the experiment would come at the expense of the number of threshold determinations that could be made since each threshold determination would require more time. The experiment as performed was sufficient to demonstrate the threshold

differences between the planar design and other coils, as well as to differentiate mean thresholds between individual axes of the planar coil system.

In experiments similar to this one [20] [24] [27], between 5 and 10% of subjects exhibited a PNS threshold curve with a very large amount of variability and were not well described by Equation 3.1. In the present work, the x- and y-axis experiments resulted in approximately this same fraction of subjects with poorly defined threshold curves; however, the z-axis experiment resulted in a higher fraction (3 of 14). None of these 3 z-axis subjects participated in the x- and y-axis experiments conducted later. The single subject from the y-axis experiment with highly variable threshold data was also one of the two x-axis subjects with highly variable threshold data. It is not known whether this is due to subject confusion, or if these subjects are actually experiencing stimulation at a wide variety of thresholds. Further work is required to understand this small section of the sample population.

Although peripheral nerve stimulation limits gradient coil operation in many applications, these show that new gradient coil designs do have the potential to significantly extend the operational limits in specific cases. The planar gradient coil used in this study can produce a localized gradient field that can safely operate at levels 2-3 times stronger than those possible with standard whole-body gradient coils. These results indicate that, although much more work is necessary to understand PNS thresholds as a function of gradient coil design, there is good reason to extend these experiments to an even larger range of gradient system configurations.

References

[1] Nishimura DG. *Principles of Magnetic Resonance Imaging.* Stanford University, 1996.

[2] Plonsey R; Heppner DB. Considerations of quasi-stationarity in electrophysico-logical systems. *Bulletin of Mathematical Biophysics,* 29:657–664, 1967.

[3] Roth BJ; Cohen LG; Hallett M. The electric field induced during magnetic stim-ulation. *Magnetic Motor Stimulation: Basic Principles and Clinical Experience,* 43:268–278, 1991.

[4] Hoffmann A; Faber SC; Werhahn KJ; Jåger L; Reiser M. Electromyography in mri – first recordings of peripheral nerve activation caused by fast magnetic field gradients. *Magnetic Resonance in Medicine,* 43(4):534–539, 2000.

[5] Ham CLG; Engels JML; van de Wiel GT; Machielsen A. Peripheral nerve stimu-lation during mri: effects of high gradient amplitudes and switching rates. *Jour-nal of Magnetic Resonance Imaging,* 7(5):933–937, 1997.

[6] Rushton WAH. The effect upon the threshold for nervous excitation of the length of the nerve exposed and the angle between current and nerve. *Journal of Physiology,* 63:357–377, 1927.

[7] Jr Brinley FJ. *Medical Physiology,* chapter Excitation and conduction in nerve fibers, pages 34–76. Mosby, Saint Louis, 13 edition, 1974.

[8] Bean CP. Stimulation of excitable tissue by rapidly changing magnetic fields. *Society for Neuroscience, 9th Annual Meeting Book of Abstracts,* 5:957, 1979.

[9] Aksel B; Marinelli L; Collick BD; Von Morze C; Bottomley PA; Hardy CJ. Local planar gradients with order-of-magnitude strength and speed advantage. *Mag-netic Resonance in Medicine,* 58(1):134–143, 2007.

[10] Marinelli L; Aksel B; Hardy CJ. Rapid cardiac mri using local planar gradients. *Proceedings of the 15th Annual Meeting of ISMRM*, 926, 2007.

[11] Budinger T. Thresholds for physiological effects due to rf and magnetic fields used in nmr imaging. *IEEE Transactions in Nuclear Science NS*, 26(2821-2825), 1979.

[12] Fischer H. Physiological effects by fast oscillating magnetic field gradients. *Proceedings of the Radiological Society of Northern America (RSNA), 75th Annual Meeting Scientific Program*, page 1189, 1989.

[13] Federal Register of the United States of America. Medical devices: Draft guidance for premarket notification submissions for magnetic resonance diagnostic devices, 1989.

[14] International Radiation Protection Association. Health physics protection of the patient undergoing a magnetic resonance examination, 1991.

[15] Reilly P. Electrical model of neural excitation studies. *APL Technical Digest*, 9:44–59, 1988.

[16] Schmitt F; Irnich W; Fischer H. *Physiological side effects of fast gradient switching*, volume Echo planar imaging theory, technique, and application of *215-233*. Springer –Verlag, 1998.

[17] Chronik BA; Rutt BK. A simple linear formulation for magnetostimulation specific to mri gradient coils. *Magnetic Resonance in Medicine*, 45(5):916–919, 2001.

[18] Budinger TF; Fischer H; Hentschel D; Reinfelder H; Schmitt F. Physiological effects of fast oscillating magnetic field gradients. *J Comput Assist Tomogr*, 15:909–914, 1991.

[19] Schaefer DJ. Safety aspects of switched gradient fields. *Magn Reson Imaging Clin N Am*, 6:731–747, 1998.

[20] Chronik BA; Ramachandran M. Simple anatomical measurements do not correlate significantly to individual peripheral nerve stimulation thresholds as measured in mri gradient coils. *Journal of Magnetic Resonance Imaging*, 17(6):716–721, 2003.

[21] Bourland JD; Nyenhuis JA; Schaefer DJ. Physiologic effects of intense mr imaging gradient coils. *Neuroimaging Clin N Am*, 9:363–377, 1999.

[22] Geddes LA. Accuracy limitations of chronaxie values. *IEEE Transactions in Biomedical Engineering*, 51(1):176–181, 2004.

[23] While PT; Forbes LK. Electromagnetic fields in the human body due to switched transverse gradient coils in mri. *Phys Med Bio*, 49:2779–2798, 2004.

[24] Zhang B; Yen YF; Chronik BA; McKinnon GC; Schaefer DJ; Rutt BK. Peripheral nerve stimulation properties of head and body gradient coils of different sizes. *Magnetic Resonance in Medicine*, 50(50-58), 2003.

[25] Schaefer DJ; Bourland JD; Nyenhuis JA. Review of patient safety in time-varying gradient fields. *Journal of Magnetic Resonance Imaging*, 12(1):20–29, 2000.

[26] King KF; Schaefer DJ. Spiral scan peripheral nerve stimulation. *Journal of Magnetic Resonance Imaging*, 12(1):164–170, 2000.

[27] Chronik BA; Rutt BK. A comparison between human magnetostimulation thresholds in whole-body and head/neck gradient coils. *Magnetic Resonance in Medicine*, 46:386–394, 2001.

[28] Weisberg S. *Applied linear regression*, pages 267–271. Applied linear regression, New York, 1980.

[29] Hebrank FX; Gebhardt M. Safe-model – a new method for predicting peripheral nerve stimulations in mri. *Proceedings of the 8th Annual Meeting of ISMRM, Denver*, page 2007, 2000.

[30] Den Boer JA; Bourland JD; Nyenhuis JA; Ham CLG; Engels JML; Hebrank FX; Frese G; Shaefer DJ. Comparison of the thresholds for peripheral nerve stimulation during gradient switching in whole body mr systems. *J Magn Reson Imaging*, 15:520–525, 2002.

[31] Reilly JP. *Applied bioelectricity*. Springer-Verlag, New-York, 1998.

Chapter 4

Insert Gradient Optimization

4.1 Introduction

In magnetic resonance imaging (MRI), contrast can be made to be a function of a number of parameters. The most basic contrast mechanisms include T_1, T_2, and proton density. Imaging protocols that include these weightings link the signal intensity to spin-lattice relaxation, spin-spin relaxation, and the concentration of excitable protons in the sample. These contrast mechanisms report on the properties of static tissues and substances. Movement within the imaging region causes signal loss [1]. Diffusion weighted imaging (DWI), takes advantage of this property to allow the proton movement and resulting signal loss to be imaged.

$$V_s \propto f(\vec{r}, \rho, G, B_o, B_1, T, \gamma, T_1)e^{-bD}e^{\frac{-t}{T_2*}} \qquad (4.1)$$

Equation 4.1 is a representation of the received MR signal [2]. The voltage in the receive coils (V_s) is some function (f) of a large number of factors, including the position ($\vec{r}$), proton density (ρ), the linear magnetic gradients (G), the main magnetic field (B_o), the radio frequency (RF) coils magnetic profile (B_1), the temperature (T), the gyromagnetic ratio for the proton (γ), and spin-lattice relaxation rate (T_1). The

signal intensity is also exponentially dependent on the spin-spin relaxation rate (T_2). All of these parameters play an important part in MRI image acquisition. In this discussion, the terms e^{-bD} and $e^{-t/T2}$ are separated from f in Equation 4.1 because they highlight how selective application of the gradients allow us to make the received voltage dependent on time, the materials diffusion coefficient (D), and strength and duration of the gradient application (b) [3].

Diffusion-weighted contrast can be used in classifying atherosclerotic plaques [4] [5], analyzing cartilage in joints [6] [7], or investigating other areas of the body [8] [9]. As well, diffusion tensor techniques are used to map neural connections in the brain [10] [11]. However, DWI is extremely sensitive to subject motion, and low signal to noise ratios (SNR) can limit the usefulness of this imagining technique as numerous repetitions and long scan times may be required. One study resorted to a five day scan in order to obtain images of sufficient detail [11].

Equation 4.1 suggests that diffusion-weighted images might be enhanced in two ways. It might be possible to increase the signal, for any image, by maximizing the term e^{-t/T_2}. That could be done by shortening t. Decreasing t, the time at which the data is acquired is a general motivation for implementing stronger gradients in MRI. In DWI, this is only possible by decreasing the time devoted to preparing the diffusion contrast (TE).

The other option suggested by Equation 4.1 is enhancing the diffusion-weighting itself, the e^{-bD} term. This could be accomplished through manipulation of the b-value. The b-value is dependent on the pulse sequence, but the calculations have common parameters. The b-value for a spin echo-diffusion sequence is shown in Equation 4.2 [12].

$$b = \gamma^2 G^2 \delta^2 |\Delta - \frac{\delta}{3}| \tag{4.2}$$

In Equation 4.2, the b-value (b) is the parameter from Equation 4.1; γ is the gyromagnetic ratio; G is the magnitude of the gradient applied. Diffusion-weighting is obtained by applying two gradient pulses of magnitude G and duration δ. These pulses are separated by some time interval during which the magnetization is flipped 180 degrees [3]. The interval between the centre of the diffusion pulses is the variable Δ.

Equation 4.2 suggests two possibilities for achieving the desired b-value, escalating the magnitude of G or altering the value of δ or Δ. An increase to δ or Δ would be a simple method of significantly affecting b. For example, doubling both δ and Δ would result in a factor of 8 increase in the b-value. However, both δ and Δ are durations and manipulating these values also affect the time, t, at which data is acquired.

Since the contrast is dependent on eliminating signal from regions of diffusion, increased b-values provide better contrast only up to a point. When the SNR of the diffusion-weighted image becomes too degraded by the high b-value, the information is lost. Since an increase in t would lead to a decrease in the magnitude of the signal (regardless of the reduction due to diffusion), lengthening δ and Δ would result in an overall loss in signal. Manipulation of G, however, can be done without losing time. The gradient strength can be expressed as the product of the coils efficiency (η) and the current produced by the amplifier (i) as shown in Equation 4.3.

$$G = \eta i \qquad (4.3)$$

Although amplifiers may be capable of very large current output to a conventional gradient system, pulse sequences are additionally constrained. For human subjects, the maximum gradient performance of existing gradient systems are limited by the peripheral nerve stimulation threshold [13]. The higher the stimulation threshold, the harder the system can be run.

In the last chapter, a planar system was demonstrated to have a high stimulation threshold and localized, or non-traditional gradient systems, have been shown to elicit stimulation at higher gradient thresholds [14] [15]. This opens up the possibility of designing a magnet to produce a gradient for use as a supplement to the traditional imaging gradients of a whole body. This gradient would function as an insert, in addition to the normal three imaging gradients, and be controlled as a fourth channel. The insert gradient would exclusively provide diffusion contrast, and because it would not be used during the image acquisition phase, constraints on the linear region for such a coil could be relaxed. In small areas, such as an atherosclerotic plaque or tumor, these magnets would be required to provide the enhanced gradient strength to only a small region of interest, allowing the rest of the image, over a larger field of view, to be acquired with conventional gradients to prevent imaging artifacts.

By relaxing field of view and geometry requirements it should be possible to design a gradient coil for diffusion weighted imaging of significantly improved gradient strength over current designs. This chapter describes the optimization of gradient coils with an increased emphasis on gradient strength.

4.2   Method

Although it is possible to design an electromagnet to produce a linear magnetic gradient on almost any shape [16], four simple non-cylindrical designs were selected for investigation and comparison. These designs were chosen for investigation because they were symmetrical, torque balanced, and easy to construct. The four base shapes, along with a conventional cylindrical design are illustrated in Figure 4.1. The first shape was a butterfly coil. This design was motivated by the coil used for transcranial magnetic stimulation, and produced a strong localized magnetic field at the centre as well as relatively strong regions of x- and z- gradients to either side of the centre.
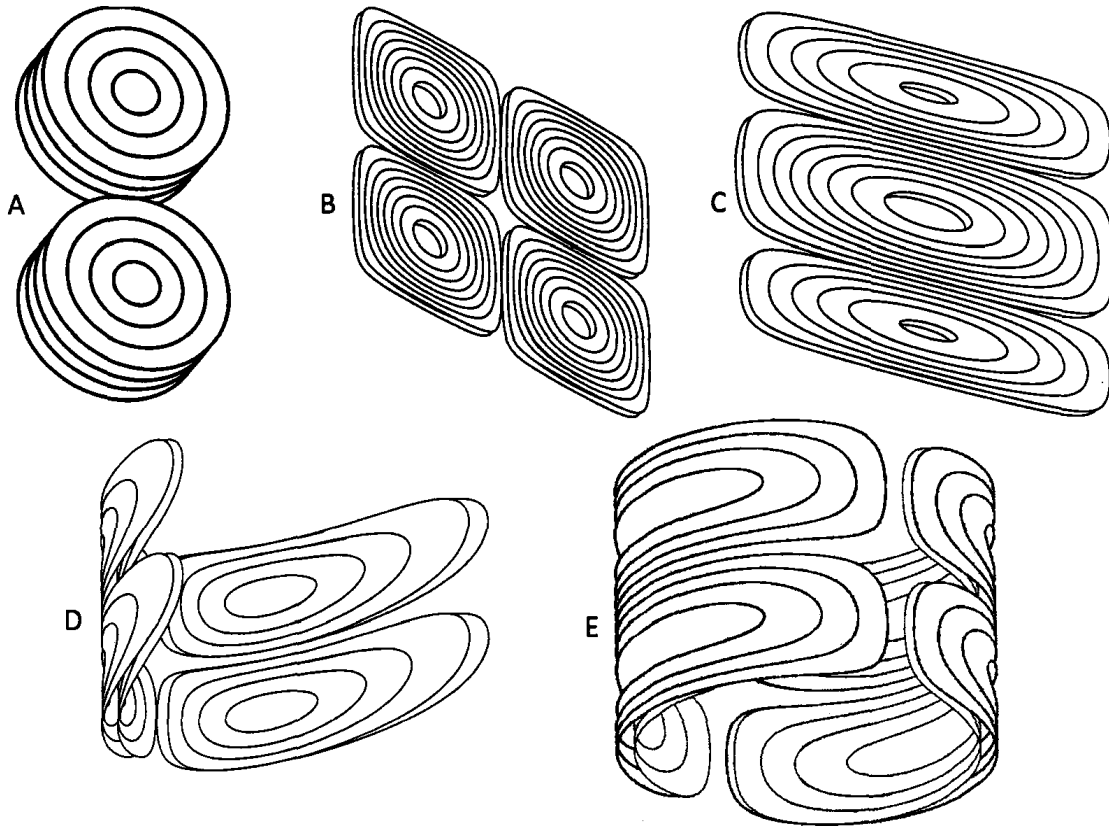
Fig. 4.1: a) butterfly, b) x-flat, c) z-flat, d) half-cylindrical, and e) cylindrical.

The planar x-gradient wire pattern, the second shape, had four loops and looked similar to an unwrapped conventional fingerprint design. The third shape was a planar z-gradient magnet. This produced a linear gradient at the centre of the sheet. Finally the half-cylindrical design also produced an x-gradient but was curved around a half-circle. For comparison, a fully wrapped cylindrical finger-print gradient was also simulated.

During the optimization, the gradient designs were evaluated with respect to the gradient produced at the focus, F, a location some specified distance above the coil. These designs were investigated in abstraction, with the dimensions scaled to (F). The design spaces for the coils were investigated in terms of 2 out of 3 potential parameters: α which was the total length of the coil divided by the focus; β, which

was the width (or diameter) of the coil divided by the focus; and ζ, which was the thickness of the coil divided by F. For each point in a given design space, a resistive (Equation 4.4) and inductive merit (Equation 4.5) was calculated.

$$M_R = \frac{\eta}{\sqrt{R}} \qquad (4.4)$$

$$M_L = \frac{\eta}{\sqrt{L}} \qquad (4.5)$$

In Equation 4.4, M_R is resistive merit and R is resistance. In Equation 4.5, M_L is inductive merit and L inductance. For both Equations 4.4 and 4.5, η is gradient efficiency at the designated focus (F) for the coil. The design space investigated varied somewhat by base shape. Each shape was investigated assuming 5 layers of close-packed windings and 8 contours.

The over-all scale of the gradients was not considered during optimization because the merit used for evaluating designs remained consistent with scaling. Once the best designs were selected, reasonable values were used to produce example coils and determine the gradient efficiencies achievable by each design. The relative dimensions of each design were investigated using software developed in C++ .

4.2.1 Butterfly coil

The butterfly coil was simulated as two circular solenoids, of close packed wire arranged as in Figure 4.1A. The internal radius was set as $F/10$. α was varied between 0.4 and 10 and ζ was varied from between 0 and 3.

4.2.2 Planar x-gradient

The wire pattern for the planar x-gradient was found by the stream function method [17]. The desired profile in the x-direction is represented in Equation 4.6 and the assumed current density in the z-direction in Equation 4.7. This design is similar the planar x-axis tested in the previous chapter.

$$J_x = sin(\frac{2\pi x}{\beta}) \quad [\frac{-\beta}{2} \le x \le \frac{\beta}{2}] \tag{4.6}$$

$$J_z = cos(\frac{2\pi z}{\alpha}) \quad [\frac{-\alpha}{2} \le z \le \frac{\alpha}{2}] \tag{4.7}$$

In Equation 4.6, J_x is the assumed profile and x is the position along the x-axis. Similarly, in Equation 4.7, J_z is the current density in the z-direction and z is position along the z-axis.

The stream function, $\psi(x, z)$, was found by integrating the product of J_x and J_z along the z-direction (Equation 4.9).

$$\psi(x, z) = \int J_x J_z dz \tag{4.8}$$

$$= \frac{\alpha}{2\pi} sin(\frac{2\pi x}{\beta}) sin(\frac{2\pi z}{\alpha})$$

The stream function was normalized to a maximum amplitude of 1, then contoured for equally spaced values of $\psi(x, z)$. The location of the contours represented the position of the wires for the gradient design.

For the planar x-gradient, ζ was set to 0.5. α was varied between 0 and 10 and β was varied between 0 and 5.

4.2.3 Planar z-gradient

The wire pattern for the planar z-gradient was, again, found by stream function method. The desired profile in the z-direction is represented in Equation 4.9 and the assumed current density in the x-direction is Equation 4.10. This design is similar the planar z-axis tested in the previous chapter.

$$J_z = sin(\frac{3\pi z}{\alpha}) \quad [\frac{-\alpha}{2} \leq z \leq \frac{\alpha}{2}] \tag{4.9}$$

$$J_x = sin(\frac{4\pi x}{\beta}) \quad [\frac{-\beta}{2} \leq x \leq \frac{\beta}{2}] \tag{4.10}$$

In Equation 4.9, J_z is the assumed gradient profile and z is the position along the z-axis. Similarly, in Equation 4.10, J_x is the current density in the x-direction and x is position along the x-axis.

The stream function, $\psi(x, z)$, was found by integrating the product of J_z and J_x along the x-direction (Equation 4.12).

$$
\begin{aligned}
\psi(x, z) &= \int J_z J_x dx \\
&= -\frac{\beta}{4\pi} sin(\frac{3\pi z}{\alpha}) cos(\frac{4\pi x}{\beta})
\end{aligned}
\tag{4.11}
$$

The stream function normalized to a maximum amplitude of 1, then contoured for equally spaced values of $\psi(x, z)$. The location of the contours represented the position of the wires for the gradient design.

For the planar x-gradient, ζ was set to 0.5. α was varied between 0 and 10 and β was varied from between 0 and 5.

4.2.4   Half-cylinder

Next, the wire pattern for the half-cylinder was found. The desired profile in ϕ is represented in Equation 4.12 and the assumed current density is Equation 4.13.

$$J_\phi = sin(2\phi) \quad [\frac{-\pi}{2} \le \phi \le \frac{\pi}{2}] \tag{4.12}$$

$$J_z = cos(\frac{2\pi z}{\alpha}) \quad [\frac{-\alpha}{2} \le z \le \frac{\alpha}{2}] \tag{4.13}$$

In Equation 4.12, J_ϕ is the assumed gradient profile and ϕ is the angle.

The stream function was found by integrating the product of J_ϕ and J_z along the z-direction (Equation 4.15).

$$\begin{aligned} \psi(\phi, z) &= \int J_\phi J_z dz \\ &= \frac{\alpha}{2\pi} sin(2\phi) sin(\frac{2\pi z}{\alpha}) \end{aligned} \tag{4.14}$$

The stream function was normalized to a maximum amplitude of 1, then contoured for equally spaced values of $\psi(\phi, z)$. The location of the contours represented the ϕ- and z- positions of the wires for the gradient design.

For the half-cylindrical gradient, β was set to 2, α was varied between 0 and 10 and ζ was varied between 0 and 2.

4.2.5   Cylindrical

For the cylindrical gradient, the desired profile in ϕ is represented in Equation 4.15 and the assumed current density is Equation 4.15.

$$J_\phi = sin(\phi) \quad [-\pi \le \phi \le \pi] \tag{4.15}$$

$$J_z = cos(\frac{2\pi z}{\alpha}) \quad [\frac{-\alpha}{2} \leq z \leq \frac{\alpha}{2}] \tag{4.16}$$

In Equation 4.15, J_ϕ is the assumed gradient profile and ϕ is the angle.

The stream function was found by integrating the product of J_ϕ and J_z along the z-direction (Equation 4.18).

$$\begin{aligned}
\psi(\phi, z) &= \int J_\phi J_z dz \\
&= \frac{\alpha}{2\pi} sin(\phi) sin(\frac{2\pi z}{\alpha})
\end{aligned} \tag{4.17}$$

The stream function was normalized to a maximum amplitude of 1, then contoured for equally spaced values of $\psi(\phi, z)$. The location of the contours represented the ϕ- and z- positions of the wires for the gradient design.

For the cylindrical gradient, β was set to 2, α was varied between 0 and 10 and ζ was varied between 0 and 2.

4.2.6 Scaling the gradient designs

Two designs were selected from each base shape for further investigation. Four designs were selected from the butterfly coil base shape to optimize for the gradient in both the $x-$ and $z-$ directions. The first was the optimized design based on resistive merit and the second was optimized design from the inductive merit study. A total of 12 designs were considered. Each design was simulated using reasonable dimensions. The focus was assigned a distance of 10 cm. This resulted in coils scaled such that they fit within a 60 cm diameter. The number of wire windings was adjusted in the simulation to ensure a reasonable inductance, near to 800 μH, while maintaining a minimum wire spacing of 3 mm. The wire connections required to power the gradient

systems were not considered in evaluating the electrical and magnetic properties of each design.

These designs were then profiled. The final inductance and resistance were calculated based on the selected number of windings. The gradient regions were mapped (Figure 4.2) and the extent of the imaging region was calculated in the x-z plane, as well as determined along the y-axis. The surrounding magnetic fields were mapped (Figure 4.3) and the magnitude of the field impinging on the main magnet was calculated. Finally, the magnitudes of the induced electric fields were determined.

Based on the projected gradient strength, the minimum pulse duration versus the achievable diffusion b-value for each design was calculated.

4.3 Results

The distribution of the z-component of the magnetic field for representative designs is shown for a single x-z slice in Figure 4.3. The approximate locations of the wires are illustrated by the solid lines, which are layered on top of the simulation. From the magnetic field, a magnetic gradient could be calculated and the electric fields could be calculated for each design. The profile of the magnetic gradients is illustrated in Figure 4.2. Figure 4.4 shows the electric field pattern that resulted from switching the gradient on and off. Any contribution due to scalar potential has been ignored.

Figures 4.5 and 4.6 show the optimization for each basic shape. Figure 4.5 shows the resistive merit for each design and Figure 4.6 is the inductive merit for each design. The results from the optimization studies are summarized in Tables 4.1 and 4.2.

For the butterfly coil, the optimal designs consistently produced stronger z-gradients than x-gradients. For the z-gradient the optimal length to F ratio (α) was 5.82±0.04;
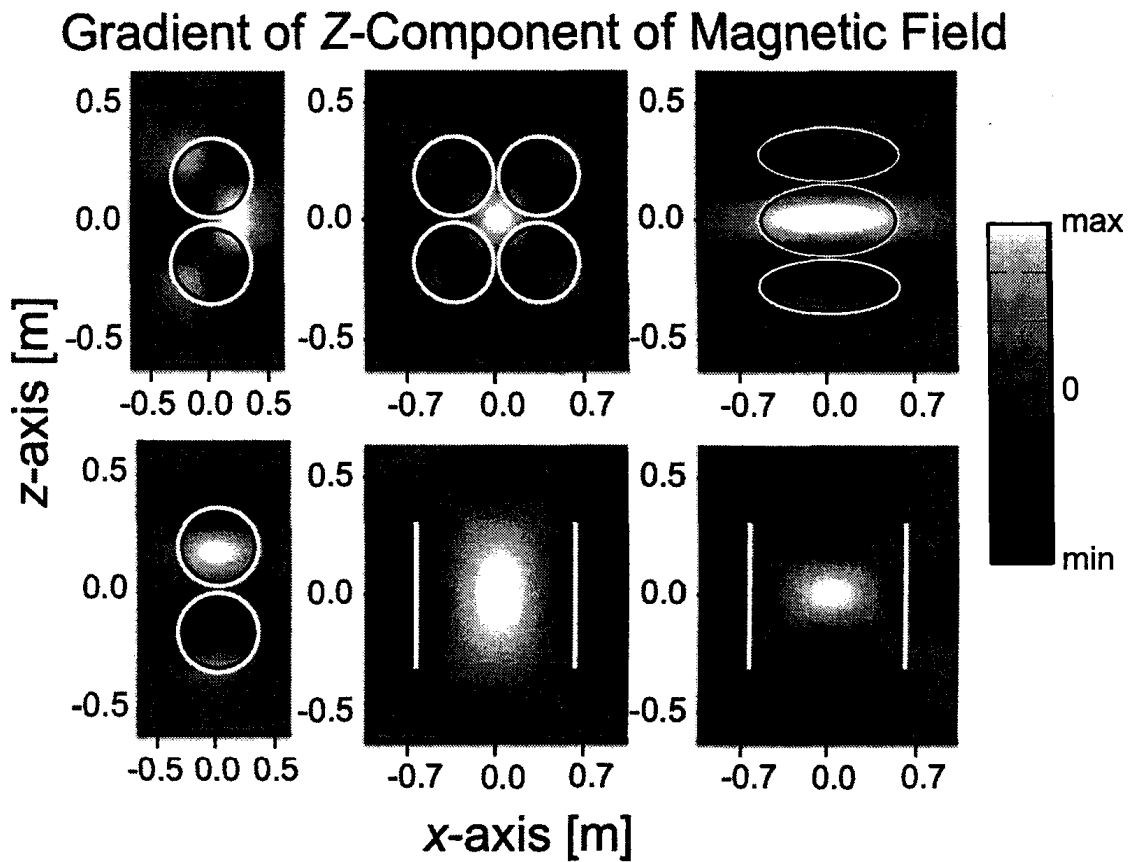
Fig. 4.2: The gradient pattern for the z-component of magnetic field for a representative design a) In the x-direction for a butterfly coil, b) in the x-direction for an x-flat coil, c) in the z-direction for a z-flat coil, d) in the z-direction for a butterfly coil, e) in the x-direction for a half-cylindrical coil, and f) in the x-direction for a cylindrical coil (centre of coil). The actual value of the magnetic field gradient is dependent on the magnitude of the current in the wire.
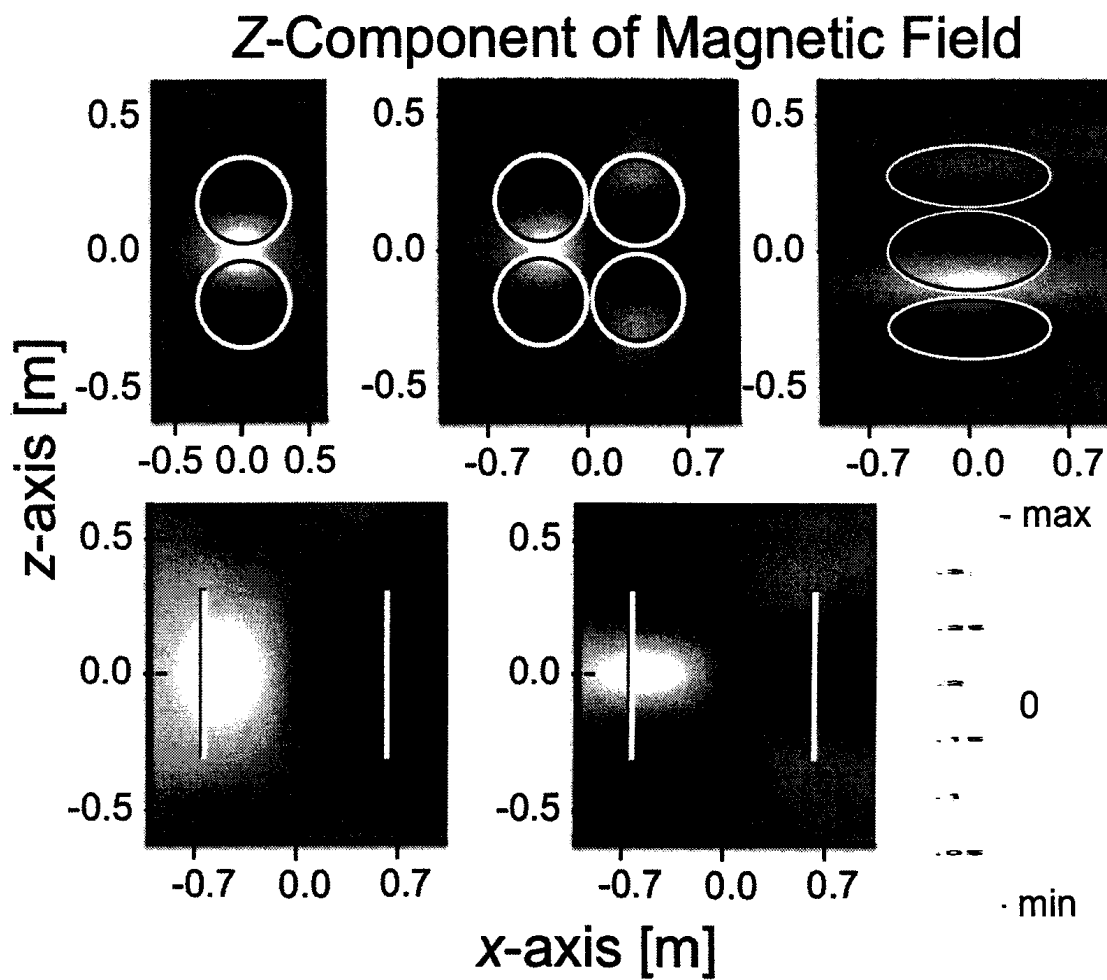
Fig. 4.3: The z-component magnetic field pattern for a representative a) butterfly coil, b) an x-flat coil, c) a z-flat coil, d) a half-cylindrical coil, and e) a cylindrical coil (centre of coil). The black and white lines represent the location of source points (wire elements). The actual value of the magnetic field is dependent on the magnitude of the current in the wire.
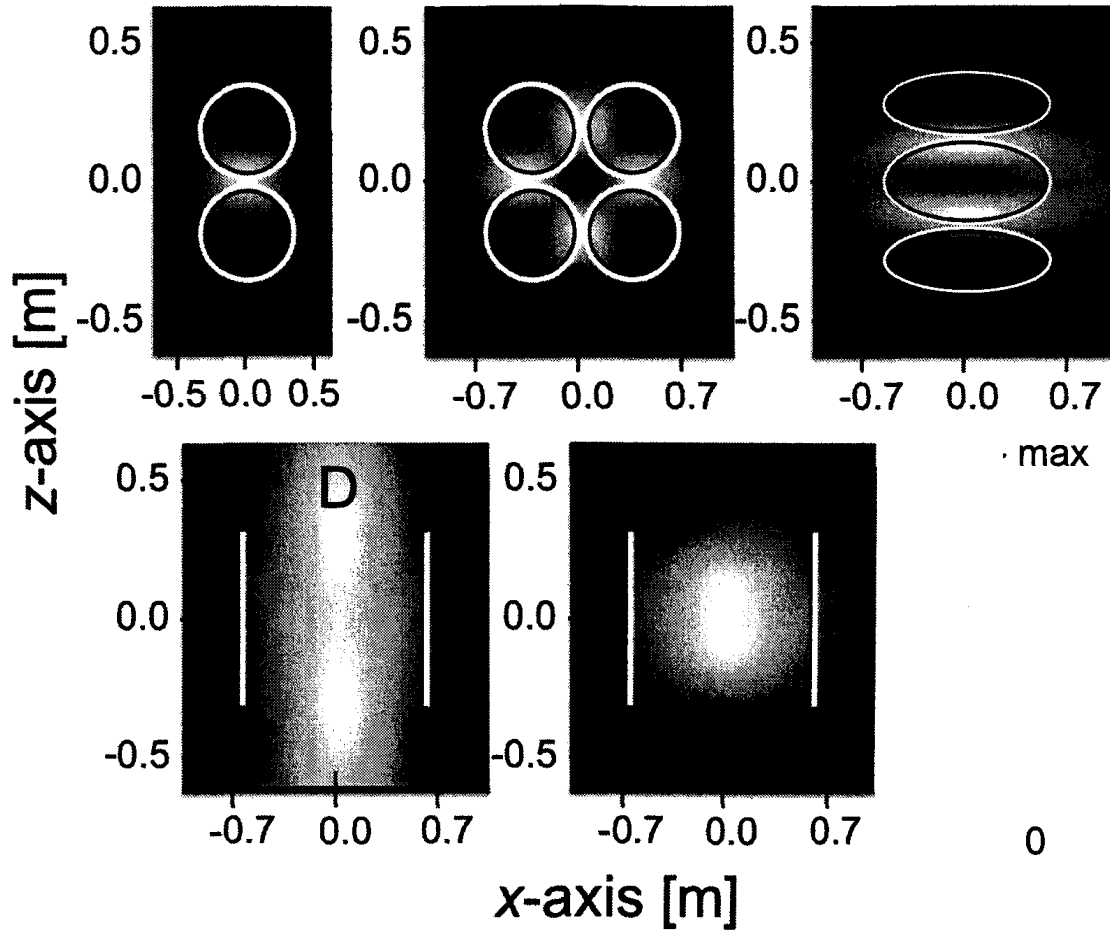
Fig. 4.4: The electric field pattern for a representative a) butterfly coil, b) x-flat coil, c) z-flat coil, d) half-cylindrical coil, and e) cylindrical coil (centre of coil). The actual value of the electric field is dependent on the rate of change of the current in the wire.

	Resistive Merit					Sample		
Configuration	Gradient	Merit	α	β	ζ	η [mT/m/A]	R [mΩ]	L [μH]
Butterfly	z	12.9	5.82	2.91	2.93	0.847	4.31	758
z-Flat	z	5.4	7.09	2.71	0.50	0.660	14.73	781
Butterfly	x	6.6	5.97	2.99	2.92	0.405	3.75	719
x-Flat	x	4.7	4.87	4.87	0.50	0.501	11.19	815
Half-cylinder	x	4.6	2.69	2.00	2.00	0.532	13.46	752
Cylindrical	x	24.4	3.99	2.00	2.00	1.56	4.13	861

Table 4.1: The result of the resistive merit investigation run on each geometry. The sample coil illustrates the gradient efficiency attainable assuming a F of 10 cm.

Optimization of Resistive Merit
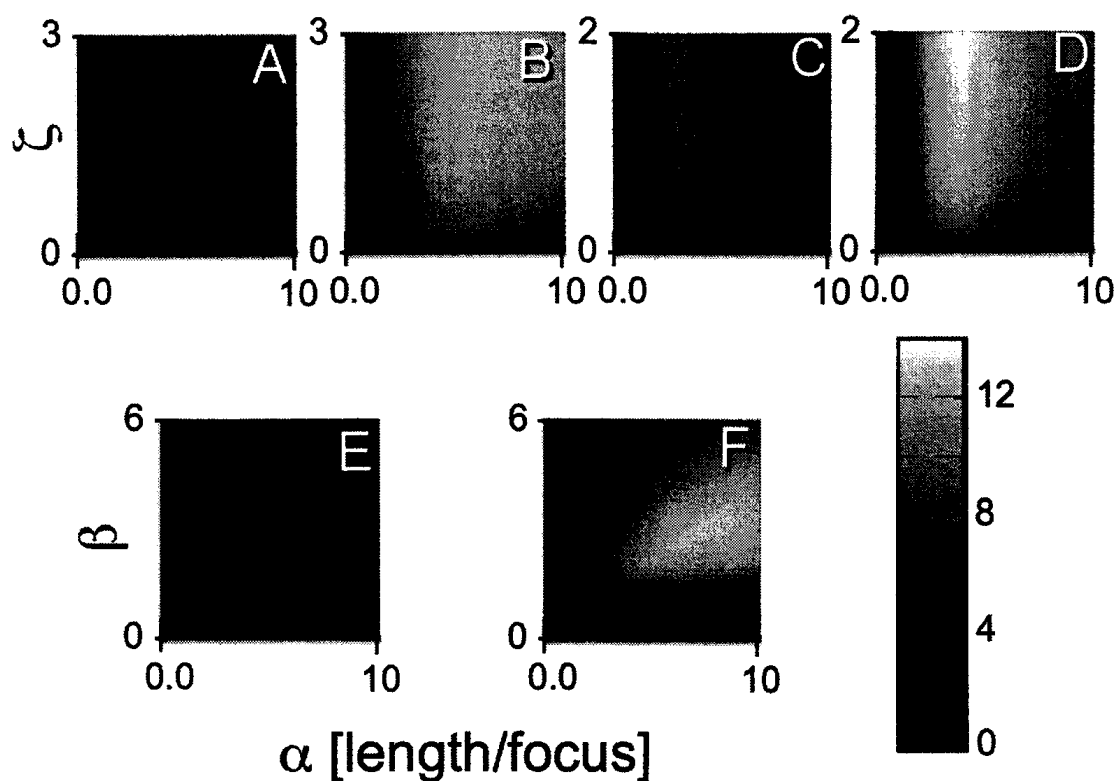

α [length/focus]

Fig. 4.5: The optimization of resistive merit across the design space. a) Butterfly x-gradient b) butterfly z-gradient c) half-cylindrical, d) cylindrical, e)x-flat, and f)z-flat geometries. The x-axis in all cases is α. The y-axis for (a), (b), (c), and (d) is ζ. For (e) and (f) the y-axis is β, the ratio of the width in the x-direction to the β.

Inductive Merit						Sample		
Configuration	Gradient	Merit	α	β	ζ	η [mT/m]	R [mΩ]	L [μH]
Butterfly	z	133	3.49	1.75	0.09	3.855	74.46	812
z-Flat	z	28.9	5.29	2.01	0.50	0.808	20.60	749
Butterfly	x	67.1	3.59	1.80	0.08	1.869	76.19	775
x-Flat	x	19.6	3.37	3.37	0.50	0.588	24.65	819
Half - cylindrical	x	43.7	2.59	2.00	0.06	1.076	182.5	608
Cylindrical	x	120	2.69	2.00	0.06	3.284	20.6	749

Table 4.2: The result of the inductive merit optimization run on each geometry. The sample coil illustrates the gradient efficiency attainable assuming a F of 10 cm.
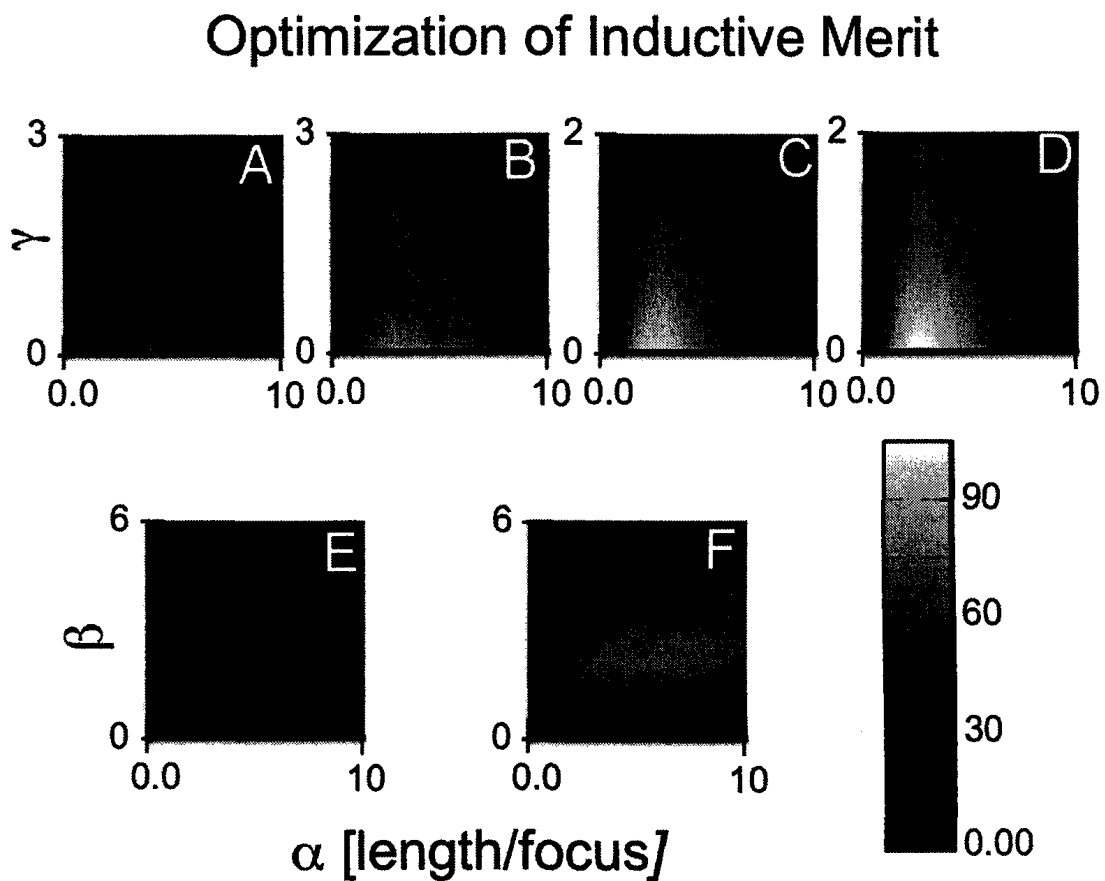
Fig. 4.6: The inductive merit investigation across the design space. a) Butterfly x-gradient b) butterfly z-gradient c) half-cylindrical, d) cylindrical, e)x-flat, and f)z-flat geometries. The x-axis in all cases is α. The y-axis for (a), (b), (c), and (d) is ζ. For (e) and (f) the y-axis is β, the ratio of the width in the x-direction to the β.

and the optimal depth to inner radius ratio (ζ) was 2.93±0.04. The width to focus ratio (β) was set by the design parameters as half of α. The resistive merit for this z-gradient design was 12.9. The inductive z-gradient design had an optimal merit of 133.3. In this case the design was a little shorter, with an α of 3.49±0.04, but it also tended towards a plate shape with a γ of 0.10±0.04.

For the planar x-gradients the optimal resistive design had an α and β ratio of 4.87±0.04. The resistive merit for this square design was 4.7. The inductive design had a merit of 19.6. As with the butterfly design, the inductive optimization resulted in a wire pattern that was a little shorter, but it was still square. This design had an α and β ratio of 3.37±0.04.

The best resistive design for the planar z-gradients had an α ratio of 7.09±0.04, and β ratio of 2.71±0.04. The resistive merit for this design was 5.4. The inductive design for the planar z-gradient had an optimized merit of 28.9. Again, it was a little shorter, with an α ratio of 5.29±0.04, and β ratio of 2.01±0.04. However, for both the inductive and resistive designs, the ratio of α/β was 2.6.

The half-cylindrical x-gradient showed no advantage in resistive merit over the flattened version, with an optimal merit of 4.6, given an α ratio of 2.69±0.01 and a thickness to inner radius ratio (ζ) of 2.00±0.01. However, the inductive merit of 43.7 was improvement over a simply planar gradient, with an α ratio of 2.59±0.04 and a ζ ratio of 0.06 ±0.04.

Finally, to compare the merit to a more traditional design, albeit with a reduced radius to maintain F across all designs, the optimal cylindrical coil had a resistive merit of 24.4 given an α ratio of 3.99±0.04 and a ζ ratio of 2.00 ±0.04. The optimal inductive design had an inductive merit of 120 given an α ratio 2.69 and a ζ ratio of 0.06.

Based on the sample geometries, simulations of gradient systems were done for the optimal designs assuming a F of 10 cm, a 3 mm minimum wire diameter and an inductance as close to 800 μH as possible.

For the M_L optimized butterfly coil, this resulted in a z-gradient efficiency of 3.8 mT/m/A, or an x-gradient efficiency of 1.9 mT/m/A. If the simulation was done closer to the surface of the coil, at 5 cm, for the same design, this efficiency was increased to 9.2 mT/m/A and 4.1 mT/m/A. For the flat coils, the x-flat design produced a gradient efficiency of 0.59 mT/m/A at 10 cm, and the z-flat design produced a efficiency strength of 0.81 mT/m/A at 10 cm. While at 5 cm these strengths jump to 1.89 mT/m/A and 2.1 mT/m/A. The half-cylindrical and cylindrical designs had a 10 cm gradient efficiency of 1.1 mT/m/A and 3.3 mT/m/A, respectively. At 5 cm the efficiencies are 5.3 mT/m/A and 4.1 mT/m/A. These gradient efficiencies are illustrated by the graph in Figure 4.7. The total height of the bar represents the gradient efficiency at 5 cm, while the internal division represents the gradient efficiency at 10 cm. For comparison, the listed gradient efficiency of a full-sized body gradient, and a smaller, specialized head-neck gradient systems are shown on the right.

The strength of the butterfly design is largely counteracted by the decreased 30% and 50% homogeneity region. Figure 4.8 shows the size of the region of homogeneity calculated for each of the M_L -optimized designed for $F = 10$ cm. For the x-gradient of the butterfly design, the region where the gradient is within 30% of maximum is 6.5±0.7 cm, 4.0±0.7 cm and 10.0±0.7 cm in the x-, y-, and z-axis respectively. For the z-gradient butterfly axis, this region is 9.8±0.7 cm, 3.8±0.7 cm, and 6.3±0.7 cm; for the x-flat design it is 9.4±0.7 cm, 2.0±0.7 cm and 9.4±0.7 cm; for the z-flat design this region is 14.4±0.7 cm, 3.0±0.7 cm and 10.1±0.7 cm; for the semi-cylindrical design this region is 7.2±0.7 cm, 1.7±0.7 cm, and 7.3±0.7 cm. Finally, for the full-
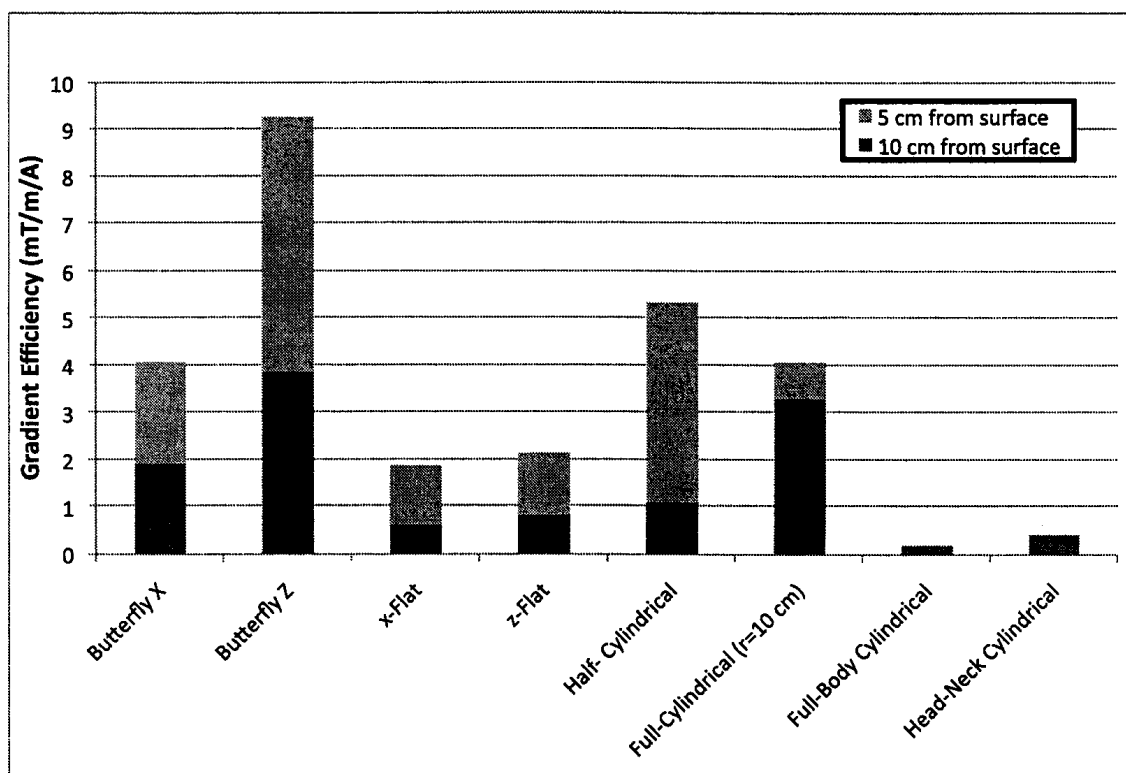
Fig. 4.7: The gradient efficiency at five and 10 cm from the surface of the coil for butterfly x-gradient, butterfly z-gradient, half-cylindrical, cylindrical, x-flat, and z-flat geometries.
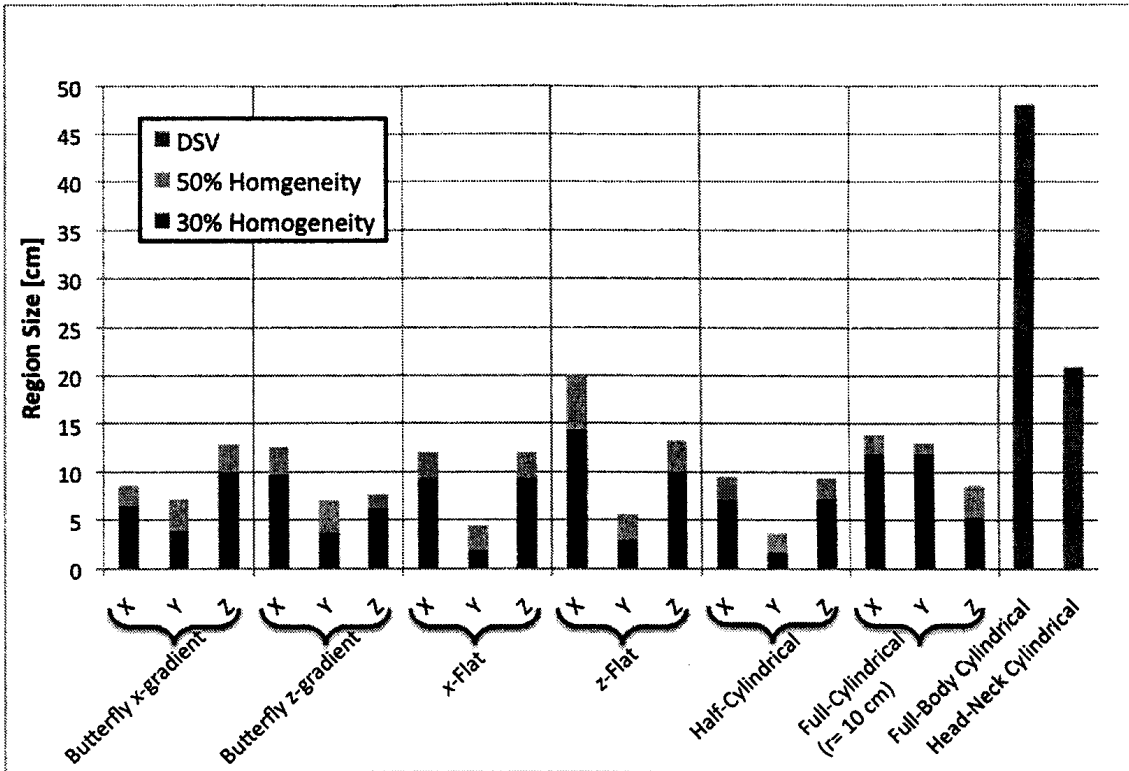
Fig. 4.8: Effective gradient region size. Regions of 30% and 50% linear gradients. The graph illustrates the dimensions of the area of linear gradient along each axis for each design optimized for inductive merit. Each coil was designed with $F = 10$ cm

cylindrical design, this region is the largest at 12.0±0.7 cm, 12.0±0.7 cm, and 5.4 ±0.7 cm.

4.4 Discussion

Gradient patterns optimized for inductive merit were consistently shorter and thinner than the gradient patterns optimized for resistive merit. This is probably due to two effects. The first is the contribution of wire area to resistance as illustrated in Equation 4.18.

$$R_c = \frac{\rho_c l}{A}$$ (4.18)

For a copper wire of set resistivity (ρ_c), the larger the wire area (A) is, the smaller the resistance (R_c). This would cause gradient systems designed for resistive merit to favour wire patterns with thick wires and thick layers. Combined, this results in an overall increase in length and thickness for a given number of windings. Competing with a drive to minimize resistance is the importance of proximity to the strength of a magnetic field and the resulting gradient. Equation 4.19 is the Biot-Savart law, illustrating that the strength of the magnetic field ($\vec{B}$) is inversely proportional to the square of the distance from the source point or wire element ($d\vec{l}$).

$$\vec{B} = \oint \frac{\mu_o}{4\pi} \frac{I d\vec{l} \times \hat{r}}{R^2} \tag{4.19}$$

In Equation 4.19, I is the current; μ_o is the permeability of free space; $\hat{r}$ is the unit vector describing the vector from the source point or wire element to the field point, and R is the distance between the source point and the field point. The relationship between distance and field strength in Equation 4.19 was a counter for the trend to increased area and pushed towards slim plates and cylinders. For this set of simulations, when resistive merit was calculated, the benefit from the increase in wire area overcame the minor improvements of proximity to result in thick coils. For inductive merit, the benefit of increased wire area was completely removed, and the optimal coils tended towards thin plates.

The x-flat gradient design was essentially similar to the half-cylindrical design, and the resulting optimized resistive merits are essentially identical (4.7 for the x-flat and 4.6 for the half-cylindrical). However, the 180 degree curve in the wire pattern for the half-cylindrical design resulted in a significant effect on the optimized inductive merit. The x-flat design was capable of achieving a gradient efficiency of 0.590 mT/m/A with an inductance of 819 μH (merit = 19.6.) The semi-cylindrical design, however achieved a gradient efficiency of 1.076 mT/m/A with an inductance

of only 608 μH. The semi-cylindrical design was simulated with a low inductance because it was impossible to continue to add windings to the structure and maintain the minimum physical wire spacing of 3 mm. For all other gradient design systems (including the cylindrical design) the target inductance was achieved prior to reaching the wire-spacing constraint.

The gradients for these designs, calculated at 10 cm from the surface of the coil range from good (0.59 mT/m/A for the x-flat gradient) to excellent (3.9 mT/m/A for butterfly coil). However, at 5 cm, slightly closer to the surface of a coil, but still at a reasonable depth for regions like the neck, knee, or elbow joints, the efficiency jumped significantly for all designs. For example, η=1.9 mT/m/A for the x-flat gradient and 9 mT/m/A for the z-gradient butterfly coil. Figure 4.7 illustrates the effect of this proximity for all coils.

Although not optimized for, the imaging region size also has some importance. The effective imaging regions for the x- and z-flat gradient designs were consistently larger than the imaging regions for the butterfly design. This can be seen by an examination of Figure 4.8. While the planar x- and z- gradients provided a good gradient efficiency over a relatively large imaging region, the butterfly designs provide sharp improvements in efficiency over a much more limited region. In all cases the imaging region was significantly smaller than either the traditional full-body gradient or the head-neck customized gradient.

Most of the local, gradients will allow improved b-values, as is illustrated in Figure 4.9. In order to achieve a b-value of 1000 s/mm^2 for diffusion weighted imaging using a conventional whole-body gradient, assuming an optimum diffusion weighted pulse and amplifiers capable of outputting 300 A, a minimum of 39 ms of contrast-weighting is required before data can begin to be obtained. For comparison, only 5 ms of weighting is required using the z-gradient butterfly coil, or 14 ms for the z-flat
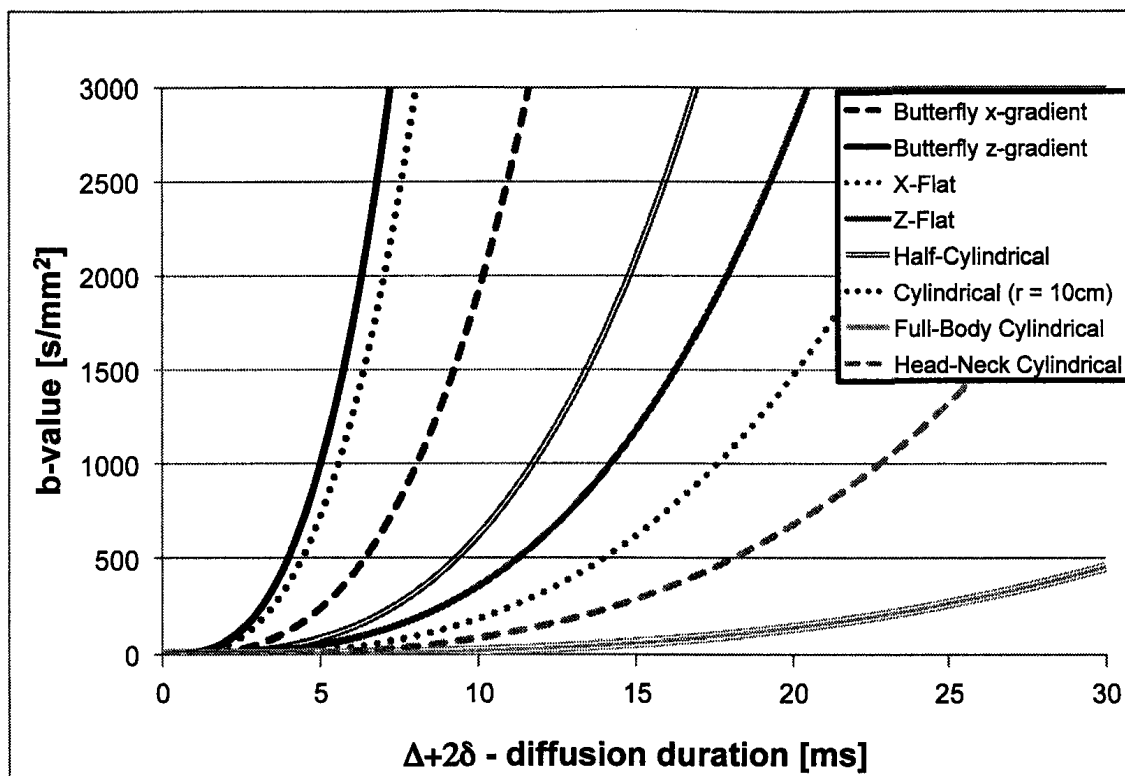
Fig. 4.9: Diffusion b-value calculated assuming a 300 A driving current. The graph illustrates the minimum contrast-preparation time required in order to achieve a particular b-value for each gradient designed for optimal inductive merit. Each coil was designed to have a F of 10 cm.

gradient coil.

The faster imaging, made possible by the localized gradients, could improve image quality. If we assume a T_2 value near 30 ms for tissue, this may result in approximately 30%, or 70%, more magnetization at the start of data collection for a diffusion image weighted with a z-flat coil or butterfly coil, respectively, over the same 1000 s/mm^2 weighting with a body coil.

4.5 Conclusion

Strong gradients can be used in magnetic resonance imaging. However, in order to prevent peripheral nerve stimulation, the field of view may need to be reduced. Localized gradient coils have the potential to provide significant improvement in gradient strength for contrast weighting for diffusion imaging.

The shape of the supplemental gradient selected would depend on the desired application. For very small regions of interest, such as a plaque no more than a few centimeters across, a butterfly coil produces the strongest magnetic gradients for surface applications. However, the planar gradient design allowed for a larger region of interest. Finally, if the opportunity exists to completely surround the area, and still maintain close proximity to the region of interest, for example a hand or foot joint, then a small radius cylindrical gradient may provide the strongest gradient, although PNS may become an issue.

The selection of the most appropriate gradient design will be application dependent, and if the control of a fourth axis for diffusion weighted imaging can be implemented successfully, localized gradients will allow significant improvements in imaging time and signal to noise ratio.

In the following chapter, we investigate the use of a representative butterfly design for obtaining diffusion-weighted images from phantoms in the bore of a 1.5T MRI scanner.

References

[1] Haacke EM; Brown RW; Thompson MR; Venkatesan R. *Magnetic Resonance Imaging: Physical Principals and Sequence Design.* Wiley-Liss, 1999.

[2] Bammer R. Basic principles of diffusion-weighted imaging. *European Journal of Radiology*, 45(3):169–184, 2003.

[3] Carr HY; Purcell EM. Effects of diffusion on free precession in nuclear magnetic resonance experiments. *Phys Rev*, 94(3):630–8, 1954.

[4] Ronen RR; Clarke SE; Hammond RR; Rutt BK. Carotid plaque classification: Defining the certainty with which plaque components can be differentiated. *Magn Reson Med*, 57(5):874–80, 2007.

[5] Clarke SE; Hammond RR; Mitchell JR; Rutt BK. Quantitative assessment of carotid plaque composition using multicontrast mri and registered histology. *Magn Reson Med*, 50(6):1199–1208, 2003.

[6] Potter HG; Black BR; Chong le R. New techniques in articular cartilage imaging. *Clin Sports Med*, 28(1):77–94, 2009.

[7] Miller KL; Hargreaves BA; Gold GE; Pauly JM. Steady–state diffusion-weighted imaging of in vivo knee cartilage. *Magn Reson Med*, 51(2):394–398, 2004.

[8] Plank C; Koller A; Mueller-Mang C; Bammer R; Thurnher MM. Diffusion-weighted mr imaging (dwi) in the evaluation of epidural spinal lesions. *Neuro-radiology*, 49(12):944–985, 2007.

[9] Balassy C; Kasprian G; Brugger PC; Csapo B; Weber M; Hormann M; Bankier A; Bammer R; Herold CJ; Prayer D. Diffusion-weighted mr imaging of the normal fetal lung. *Eur Radiol*, 18(4):700–706, 2008.

[10] Freidlin RZ; Ozarslan E; Komlosh ME; Lin-Chang C; Koay CG; Jones DK; Basser PJ. Parsimonious model selection for tissue segmentation and classification applications: a study using simulated and experimental dti data. *IEEE Trans Med Imaging*, 26(11):1576–1584, 2007.

[11] McNab JA; Jbabdi S; Deoni SC; Douaud G; Behrens TEJ; Miller KL. High resolution diffusion-weighted imaging in fixed human brain using diffusion-weighted steady state free precession. *Neuroimage*, 46(3):775–785, 2009.

[12] Stejskal EO; Tanner JE. Spin diffusion measurements: spin echoes in the presence of a time-dependent field gradient. *Journal of Chemical Physics*, 42:228–292, 1965.

[13] U.S. Department of Health and Human Services. Guidance for industry and fda staff. criteria for significant risk investigations of magnetic resonance diagnostic devices. *Food and Drug Administration, Centre for Devices and Radiological Health*, page 3, July 2003.

[14] Chronik BA; Rutt BK. A comparison between human magnetostimulation thresholds in whole-body and head/neck gradient coils. *Magnetic Resonance in Medicine*, 46:386–394, 2001.

[15] Feldman RE; Hardy CJ; Aksel B; Schenck J; Chronik BA. Experimental determination of human peripheral nerve stimulation thresholds in a 3-axis planar gradient system. *Magn Reson Med*, 62(3):763–770, 2009.

[16] Poole M; Bowtell R. Novel gradient coils designed using a boundary element method. *Concepts Magn Reson Part B*, 31B(3):162–175, 2007.

[17] De Bever JT. *Multiple-imaging-region gradient coil insert for parallel imaging of mice in MRI.* PhD thesis, University of Western Ontario, August 2007.

Chapter 5

Diffusion-Weighted Imaging with an Insert Gradient

5.1 Introduction

In this chapter a method for doing diffusion-weighted imaging using a fourth-channel to power an insert gradient separate, from the imaging gradient set, is described. The chapter begins with an introduction to diffusion-weighted imaging and discusses the motivation for separating the gradient-function for diffusion-weighting from the gradient-function for imaging. The chapter moves on to discuss the design, construction, integration, testing, and calibration of a butterfly insert gradient. Finally, the results of imaging with a fourth gradient are shown.

Diffusion-weighted imaging (DWI) in magnetic resonance imaging (MRI) can be used to gather information to try to answer a variety of questions including some regarding the composition of atherosclerotic plaques [1], joint and cartilage structure [2], and brain connectivity [3]. Diffusion-weighted contrast produces data about the composition and structure of tissues that is unique from T_1, T_2, or proton-density-weighted imaging. Unfortunately, because of the time required to encode the

diffusion-weighting in the pulse sequence, DWI is susceptible to motion artifacts [4] and suffers from a relatively low image signal to noise ratio (SNR) [5].

Diffusion-weighted imaging emphasizes the effect of the diffusion of magnetic-moments in the sample. An application of Fick's law [6], in Equation 5.1, states that the diffusion-length (∂) is a function of the square root of the diffusion co-efficient (D), and the duration of the random walk (t).

$$\partial = 2\sqrt{Dt} \tag{5.1}$$

If a linearly varying magnetic field, like the switched gradients used in image acquisition, is applied to a sample, a hydrogen nucleus (proton) diffusing through that gradient will experience a position-dependent magnetic field. At the end of the gradient application, the magnitude of the received signal from any point along the gradient will be reduced by contribution of protons that have diffused into, or out of, that region and are out-of-phase with the rest of the sample. This signal loss, due to diffusion, is the mechanism of contrast in diffusion-weighted imaging [7].

The diffusion weighted signal loss can be distinguished from signal loss due to other T_2 effects by using a particular spin echo sequence. A gradient is applied for a fixed period of time in order to cause a precise amount of dephasing; the magnetization is rotated 180 degrees; then a second, identical, gradient is applied to perfectly rephase the static components of the image [8].

The signal acquired from a diffusion-weighted pulse sequence (S) in Equation 5.2 is proportional to the T_2 weighted image of the spin echo pulse sequence, but is modified by a diffusion-weighting factor (e^{-bD}).

$$S \propto M_o e^{-bD} e^{-\frac{t}{T_2}} \tag{5.2}$$

In Equation 5.2, D $[mm^2/s]$ is the diffusion coefficient of the tissue, and b $[s/mm^2]$ is the b-value defined in Equation 5.3 for the pulse sequence in Figure 5.1 [9].

$$b = \gamma^2 G^2 \delta^2 |\Delta - \frac{\delta}{3}| \tag{5.3}$$

In Equation 5.3, G is the applied gradient $[mT/m]$, δ is the duration of the gradient pulse $[ms]$, and Δ is the separation between the gradient pulses $[ms]$. The more rapidly the signal can be acquired, the less T_2 relaxation occurs, resulting in a larger overall signal and better SNR.

The b-value weighting, on the other hand, is a balancing act. Since the contrast is dependent on eliminating signal from regions of diffusion, increased b-values provide better contrast only up to a point. When the SNR of the diffusion-weighted image becomes too degraded by the high b-value, the information is lost.

A strong gradient, pulsed rapidly, has the potential to allow b-values to be obtained with short echo-times (TE) during spin-echo-diffusion-weighted imaging, thus improving SNR and reducing motion sensitivity. However, such strong gradients run the risk of inducing peripheral nerve stimulation [9]. Some localized, and non-cylindrical gradients have been shown to have higher stimulation thresholds [10] [11], and permit rapidly switched gradient fields to be operated with larger gradient magnitude. Unfortunately, over-restricting the field of view during imaging can also cause image artifacts [12]. An ideal gradient system for diffusion-weighted imaging would provide a strong, localized gradient over a small area for the diffusion weighting, and a weaker, whole body linear gradient for image acquisition. These requirements suggest the inclusion of a fourth gradient coil dedicated to diffusion-contrast.

The inclusion of a fourth axis is an extension of current technology. Multiple-channel-radio-frequency transmit and receive systems have become common practice
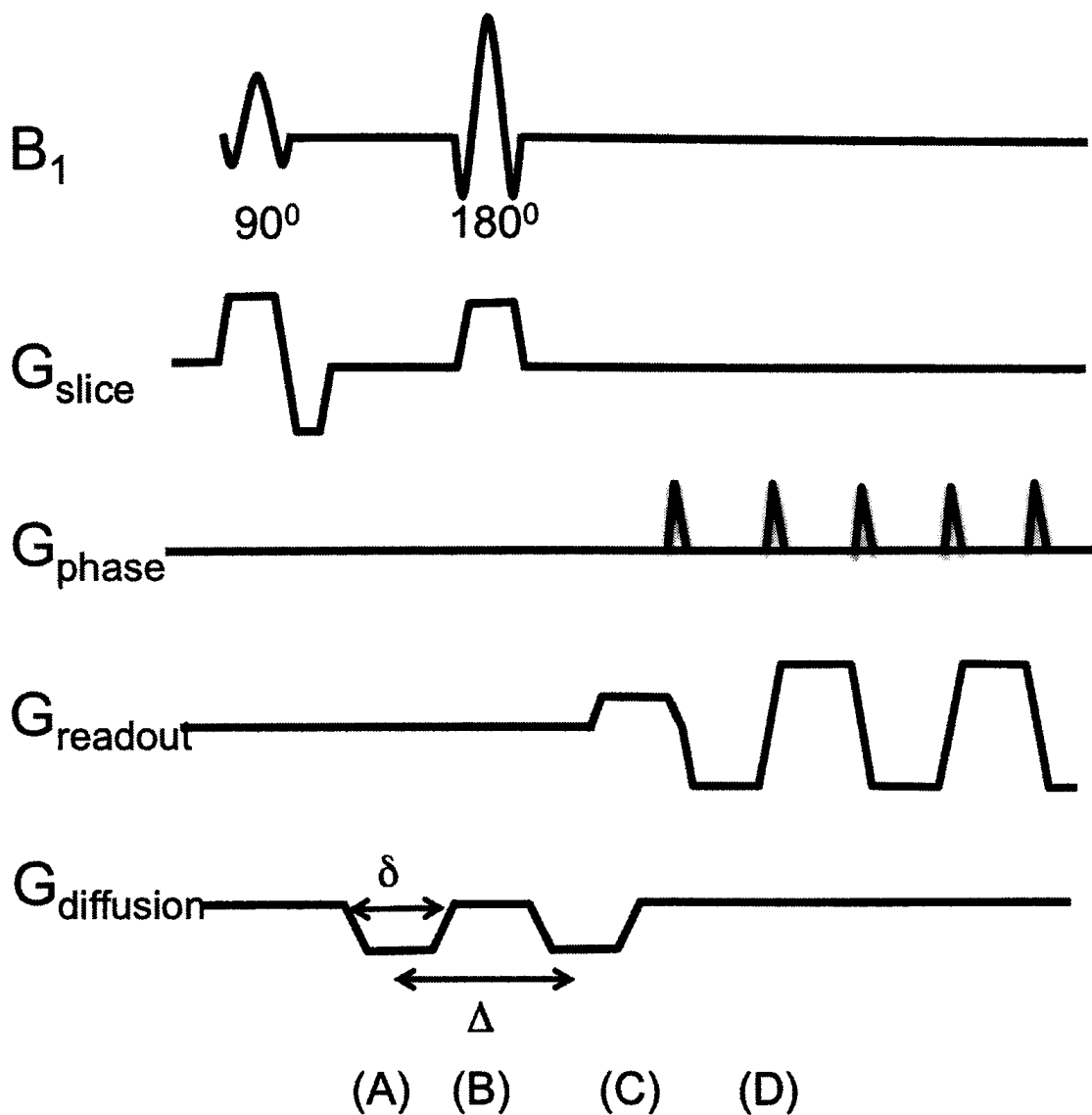
Fig. 5.1: A gradient is applied to the excited magnetization of a sample (A). The molecules are allowed to diffuse and the magnetization is rotated 180 degrees (B). A second, identical, gradient is applied to re-phase the magnetization (C), and an echo planar imaging sequence is used to obtain an image(D).

[13] [14], and recent experiments have demonstrated the feasibility of operating a constant-field electromagnet in the bore during imaging for additional, and novel contrast weightings [15].

A powerful gradient for diffusion weighted imaging that is useful over a limited field of view could assist in determining the composition of small structures in the body, such as atherosclerotic plaques in the neck, tumors in the breast or small spaces in knee or wrist joints.

To determine if a signal to noise advantage could be obtained in diffusion-weighted imaging using strong gradients, a localized insert gradient was operated in addition to traditional full-body gradients to produce apparent diffusion coefficient (ADC) maps in a phantom.

5.2 Methods

A number of steps were required to integrate the insert gradient into a diffusion pulse sequence. First the gradient was designed, using a computer simulation, and constructed. To get the insert integrated and working with the MR system, a control system had to be constructed to manage the amplifier power to the gradient and the pulse sequence for the insert had to be timed so that it lined up precisely with the timing of the spin-echo sequence used for normal T2 weighting.

With the amplifiers hooked up and the pulse sequence timing known, the insert and the system could be tested. A phantom was imaged with the amplifiers delivering no current, to asses any major susceptibility issues in the insert that might result in image distortion. Also the phantom was imaged while the insert was powered to asses amplifier bias.

Calibration of the system was required prior to attempting diffusion-weighted imaging with the insert. A homogenous phantom was imaged while the insert was powered with a diffusion-weighted sequence. From the signal loss in the diffusion-weighted image, the b-value at each point could be calculated and, based on the b-value at each point, an estimation of the gradient efficiency map at a height above the insert could be made. A gradient efficiency map based on the idealized gradient coil was also calculated from simulation.

Finally, a gelatin/water phantom was imaged, the peak of the gradient maps (both from simulation and measurement) were aligned with the location of the peak gradient in the gelatin/water phantom image. The diffusion-weighted images were processed using the gradient efficiency maps to determine the b-value at each point and calculate the ADC for the materials.

5.2.1 Design

The butterfly coil design shown in Figure 5.2a was selected for construction. While not precisely the optimal design from Chapter 4, the gradient produced by this design was sufficent to demonstrate the enhanced diffusion-weighting process. The coil consisted of two solenoids with 7 radial windings each and 5 axial windings. The selected wire pattern was simulated to generate the expected resistance, inductance, magnetic field, and magnetic field gradient. The predicted magnetic field strength is shown in Figures 5.2b. The map of the simulated gradient strength is show in Figure 5.2c. The peak gradient efficiency was calculated to be 5.67 mT/m/A at 3 cm above the surface of the coil. This efficiency was much greater than the approximately 0.18 mT/m/A efficiency of the whole body gradients. The insert efficiency map was used during the analysis of the insert-gradient-diffusion-weighted image to determine ADCs in Section 5.3.3.1.
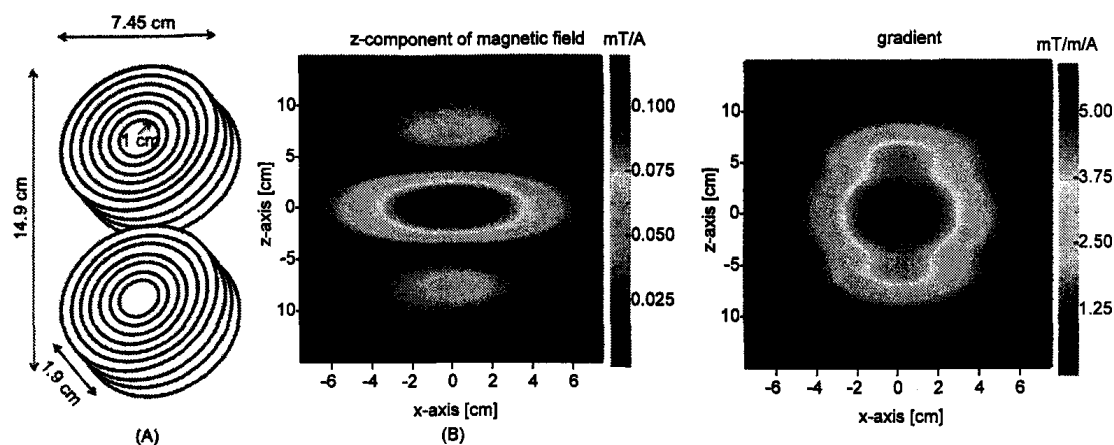
Fig. 5.2: Illustration of a butterfly coil (A). The inner radius was 1 cm; the length was 14.95 cm, the width was 7.45 cm, and the depth was 1.9 cm. (B) The profile of the z-component of magnetic field at 3 cm from the surface. Finally, (C) the B_z-gradient of a butterfly coil at 3 cm from the surface. A rectangular region of 30% uniformity at the centre has an area of 17.46 cm^2 (2.90 cm in the x-axis and 6.02 cm in the z-axis)

5.2.2 Construction

The selected coil was constructed by winding 3 mm hollow copper wire around a 1 cm radius bobbin. Additional electrical insulation was added between the layers of the copper tubing resulting in 3.91 mm wire spacing. The final dimensions of the two-solenoid butterfly coil were 14.95 cm long (z-axis), 7.47 cm wide (x-axis), and 1.96 cm deep (y-axis). Figure 5.3 is a picture of the wound coil prior to final potting.

The solenoids were potted in a thermally conductive epoxy. A cooling system and electrical connections were attached as shown in Figure 5.4a to supply water to assist in heat dissipation during gradient operation. The water was supplied in parallel to both coils while the coils were powered serially. Finally, the gradient system was attached to a press-board base designed to weight the system and allow it to slide into the bore of a 1.5 T GE system as shown in Figure 5.4b.
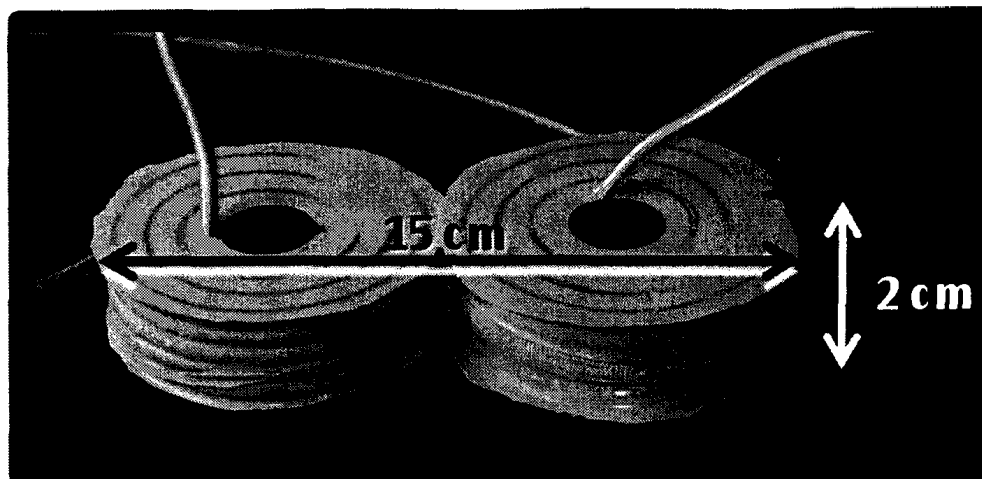
Fig. 5.3: Physical butterfly insert without electrical and cooling connections, after the epoxy used in the winding process had hardened.

5.2.3   Integration

5.2.3.1   Power

Once the construction was complete it was possible to determine the electrical properties of the system, compare them to simulation, and use the real values to set up the current feedback compensation circuit and solder it to the amplifier. Based on the documentation provided by Techron, the resistance and capacitance components required for current compensation were determined. The system was connected to a variable resistor and capacitor and the component selections for the amplifier compensation circuit were fine-tuned. The system was powered by AE Techron Model 7796 amplifiers, capable of providing up to 210 A (10 kVA peak) to the system. Extra low pass filters were installed in the filter-panel for the fourth gradient channel.

5.2.3.2   Control

The amplifiers were controlled by a LabView script, run from a Toshiba laptop. As illustrated in Figure 5.5, the LabView script was triggered by a TTL signal from the amplifiers driving the RF coil, indicating the start of the pulse-sequence. The
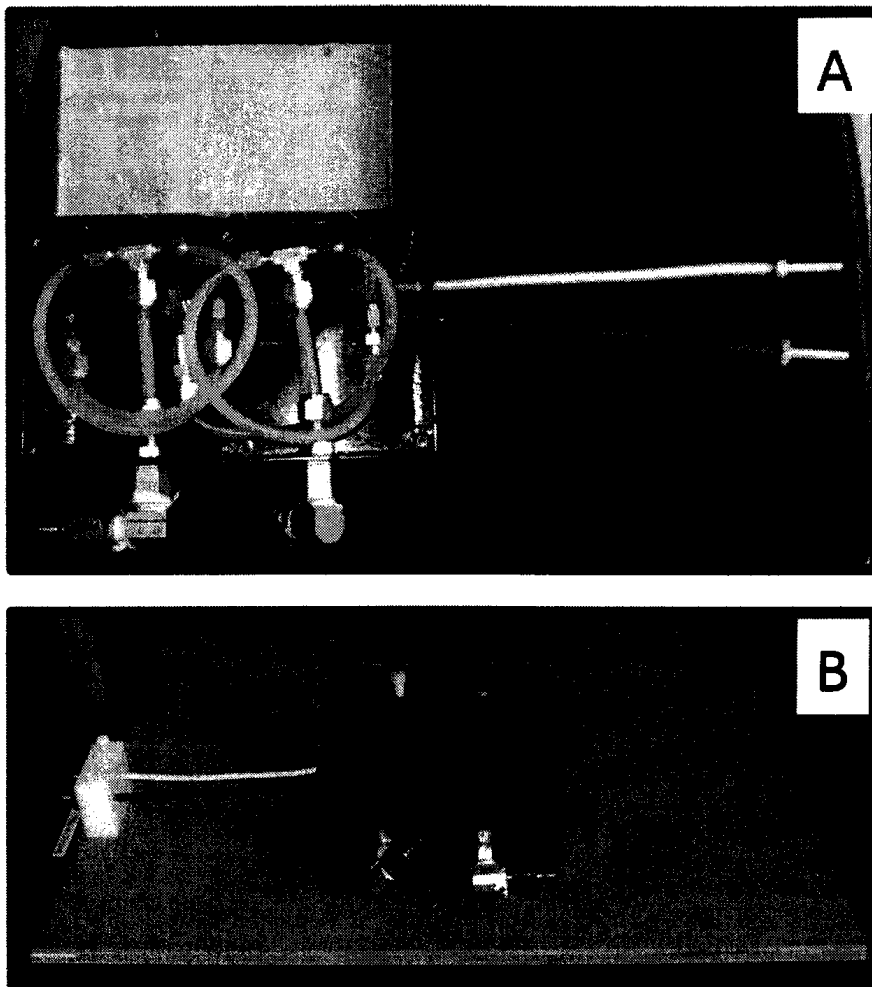
Fig. 5.4: (A) Cooling and electrical system for potted coil. (B) Press board insert and terminal block designed to fit on the patient bed of the 1.5 T MRI system.
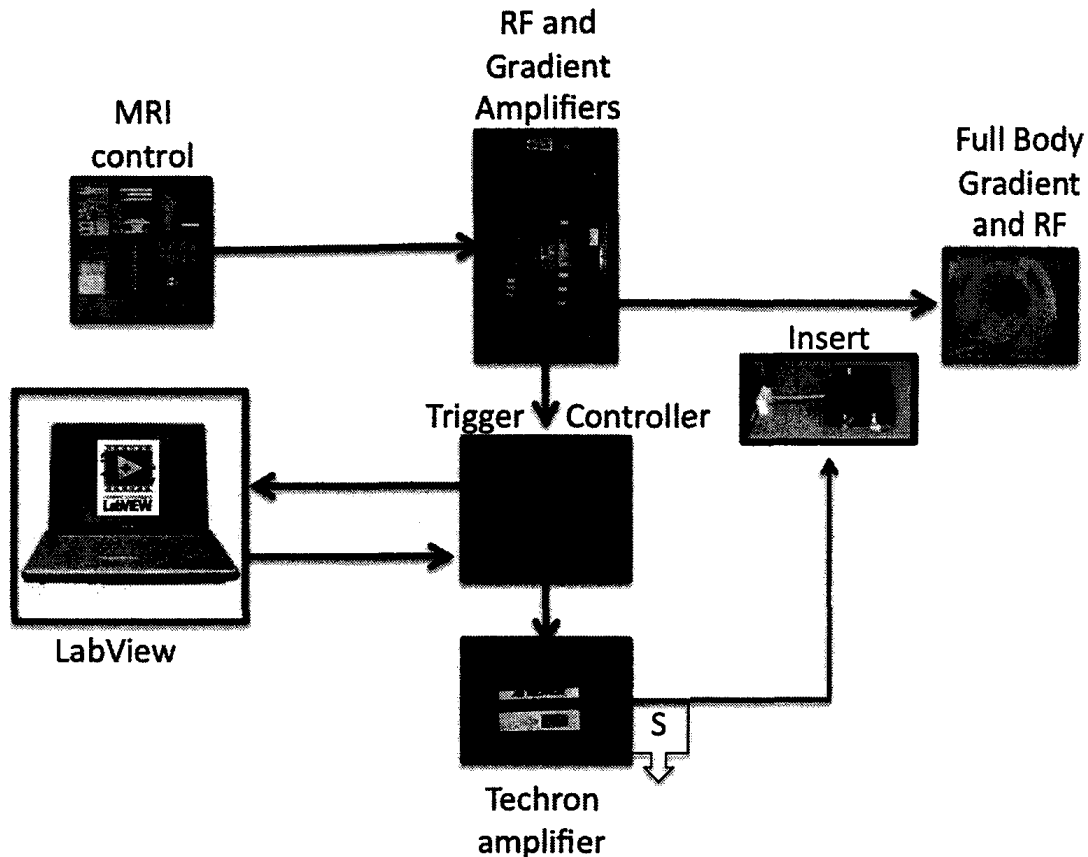
Fig. 5.5: The MRI pulse sequence was controlled by software which sent a signal to the amplifiers to drive the RF and gradient system of the MRI scanner. The amplifiers also produced a TTL pulse which triggered a LabView script enabling the control of a Techron amplifier to drive the butterfly insert.

amplifier was driven by an National Instruments card (Model 6629) that served as a waveform generator. The card was capable of a sampling frequency of 250 kHz, and an amplitude resolution of $250\mu V$ (corresponding to an amplifier-current resolution of 5 mA).

5.2.3.3 Timing

Figure 5.6 shows the pulse sequence for a diffusion-weighted sequence. When triggered by the TTL pulse the Techron amplifiers drive the butterfly coil according to the pulse sequence shown on line $G_{diffusion}$ line in Figure 5.1.
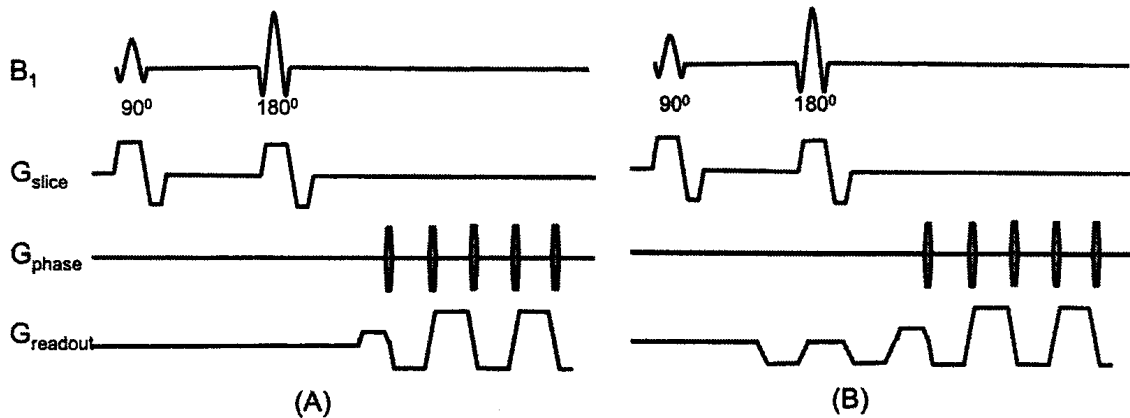
Fig. 5.6: (A) First application of the spin-echo pulse sequence produces an image with no diffusion weighting. (B) Second application of the pulse sequence produces an image with signal loss in areas where diffusion in the readout direction has occurred.

The insert-gradient pulse sequence was timed by mapping out the gradient sequence for a standard b=100 (TR/TE/BW = 10000 ms/ 49.8 ms/ 1953.12 $Hz/pixel$), x-z imaging plane. Each diffusion-weighted pulse sequence constructed using the whole body gradients consisted of two applications. An application of the spin-echo sequence without diffusion weighting (Figure 5.6A), followed immediately by an identical application of the sequence with the addition of two diffusion weighting lobes (Figure 5.6B, $\Delta = 14.9$ ms, $\delta= 9.3$ ms). This diffusion pulse-sequence produced two images, a non-weighted one to serve as a baseline for the diffusion-weighted image produced in the second application.

The insert gradient pulse sequence was adjusted to correspond with the the first acquisition (Figure 5.6A). Prior to the 180° RF flip, the insert rose to maximum gradient strength in 1 ms. The maximum gradient was held for 7 ms, and then the gradient fell to 0 in 1 ms. After the 180° flip the pulse was repeated. The duration of the second (δ) was adjusted in steps of 0.01 ms and by no more than 0.04 ms to maximize the magnitude of the diffusion-weighted signal. There was a 14.7 ms separation between the pulses.

To utilize the insert gradient, the MRI system was instructed to run the entire pulse sequence twice for each experiment. All told this resulted in 2 sets of 2 images, but the second image of the set was discarded. The first time, the diffusion-weighted pulse sequence was run without powering the insert gradients, resulting in the production of an unweighted image (from section A), as well as a weighted image (from section B) that was ignored. On the second run through the pulse sequence, the insert gradient amplifiers were synchronized to the TTL pulse, indicating the start of the pulse sequence and powered as illustrated in Figure 5.1. The image produced by section A of this run was the diffusion-weighted image and, again, the second image was discarded.

So, finally, two images were obtained: a T2-weighted image acquired using the whole-body gradient only, and a diffusion-weighted image using the insert gradients to provide diffusion pulses.

5.2.4 Testing

5.2.4.1 Susceptibility

To determine the effect of the presence of the gradient insert on imaging, and identify any susceptibility problems due to materials used in the construction of the insert, a solution of 5 g/l cupric sulphate was imaged using the whole body gradients while resting on top of the centre of the insert gradient. A gradient recalled echo sequence was run with the following imaging parameters: TR = 100 ms; matrix = 256X256; slice thickness = 10 mm; NEX = 2; FOV = 20 cm; Flip angle = 90°. Six images were taken, 2 each with the system a) plugged into energized amplifiers and held at 0 V; b) plugged into un-energized amplifiers; c) leads left open. In each case an image with a high bandwidth (122.109 $Hz/pixel$) and low bandwidth (15.625 $Hz/pixel$) was obtained, as low bandwidths tend to exacerbate any susceptibility

artifacts.

5.2.4.2 Amplifier Bias

The insert was intended to be powered only during diffusion-weighting. Any current flow during the actual image acquisition or slice selection (due to a small bias in the amplifiers) would distort the image and lead to signal loss. During imaging, the butterfly insert was placed in the magnet bore and connected to the amplifiers in 2 configurations. The homogenous phantom was imaged with a spin-echo diffusion weighted sequence (TR/TE/BW = 10000 ms/ 85.5 ms/ 1953.12 Hz.pixel) with the following parameters: matrix = 256X256; slice thickness = 2.5 mm; NEX = 16; FOV = 20 cm. The current from the amplifier to the insert was set to 40 A. Then the cables powering the butterfly were reversed, and the homogenous phantom was imaged again, with the maximum current from the amplifiers set at -40 A. Absent of amplifier bias these two images would be identical, because both the leads and the current direction were inverted, to result in no change in the pulse sequence. However, the bias in the amplifier would manifest itself as a difference in the image as the bias reversed direction when the cables were flipped.

Due to the results of the amplifier bias test, the circuit was modified by installing a switch at position S in Figure 5.5 to block amplifier current output during imaging gradient operation (and at all times other than activation of the diffusion pulses) and enable the insert gradient only when it was required. The amplifiers were carefully balanced to eliminate any remaining bias.
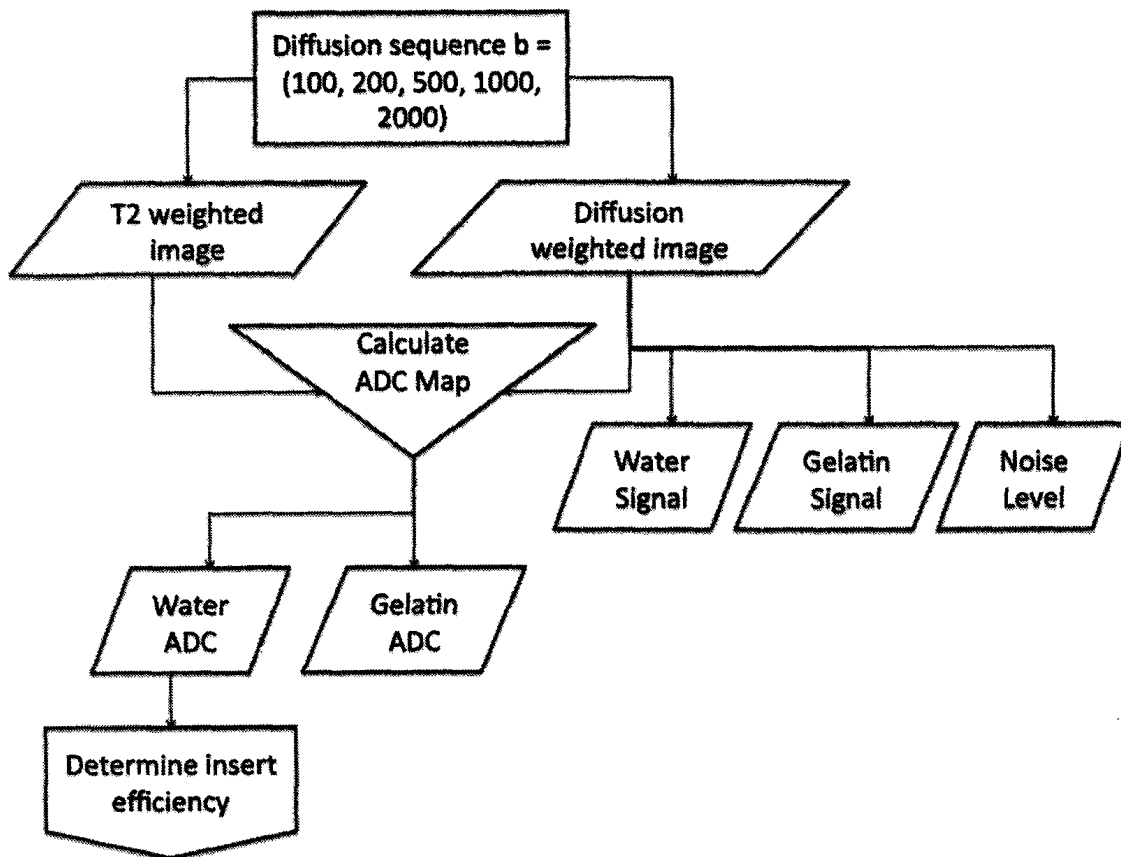
Fig. 5.7: Calculation of ADC. Using a spin-echo pulse sequence, T2 and diffusion-weighted images were collected for b = 100, 200, 500, 1000, and 2000 s/mm^2 . The SNR of the water and gelatin was calculated using the diffusion-weighted image and the combination of images was used to determine the ADC of each component of the phantom. The ADC of water was used later in the determination of the insert efficiency.

5.2.5   Preparation

5.2.5.1   Determination of ADC: whole-body diffusion-weighted imaging

The flow chart in Figure 5.7 shows the process used to determine the diffusion coefficients. A phantom with liquid and gelatin components, shown in Figure 5.8, was imaged (without the insert gradient) with a diffusion-weighted spin-echo sequence (TR/BW = 10000 ms /1953.12 $Hz/pixel$) minimum TE and a diffusion weightings of b = 100, 200, 500, 1000, and 5000 s/mm^2 (TE = 49.8, 55.2, 64.8, 74.4, and 86.5 ms). The image acquisition parameters were as follows: field of view, 20 cm; section thickness, 2.5 mm; matrix = 128x192; NEX = 16. The apparent diffusion coefficient was calculated by a taking the logarithm of a pixel by pixel ratio of the image from section A to section B. The result of that operation was then divided by the appropriate b-value.

The SNR of the diffusion-weighted image was calculated by sampling a 440 pixel ROI inside each of the gelatin, the water, and the noise background. The average signal of the water and the gelatin was then divided by the mean of the noise background and multiplied by a Rician correction factor [12].

5.2.5.2   Determination of insert gradient efficiency

The flowchart in Figure 5.9 describes how the efficiency was experimentally determined for the insert gradient. The homogenous water phantom was imaged using the butterfly insert with 22.25A, 30A, 40A, and 60A of current running through the coil during the diffusion pulse. A spin-echo diffusion-weighted sequence was used (TR /TE/ BW = 10000 ms /49.8 ms /1953.12 Hz per pixel) with the following parameters: matrix = 128X128; slice thickness = 2.5 mm; NEX = 16; FOV = 20 cm.

Knowing the ADC value from the analysis above, the image data was used to extract the effective b-value produced by the insert on a per-pixel basis, for each current level.
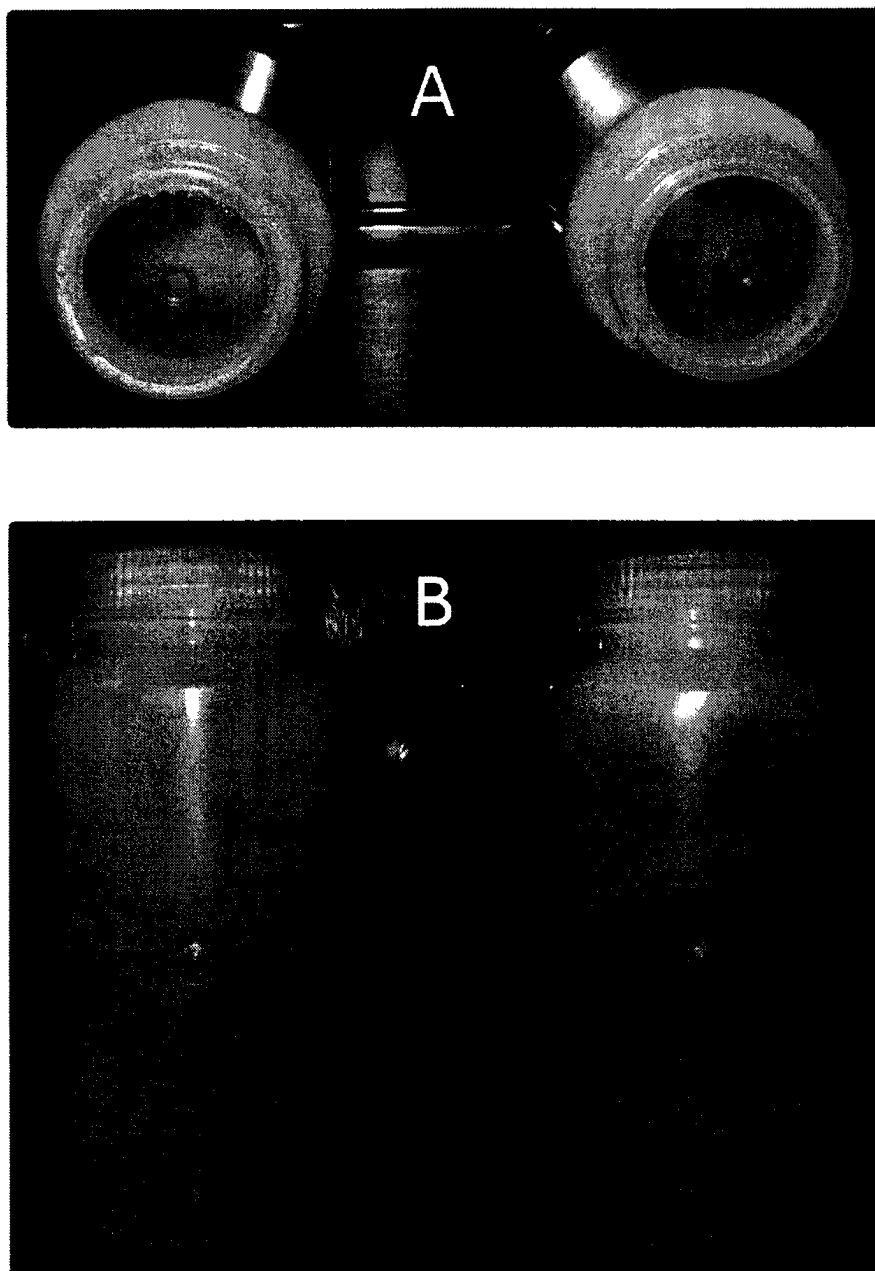
Fig. 5.8: Top view (A) and side view (B) of phantoms used during diffusion-weighted imaging. A homogenous liquid phantom is shown (left) and a water/gelatin phantom is shown (right).

The b-values were then converted into an apparent gradient. The gradient maps were smoothed by convolution with a 2D gaussian kernel with a width of three pixels and the peak gradient from each map was plotted. A linear-least-squares-fit was made to the plot of peak gradient vs. current. The slope and intercept of this plot was extracted from the fit.

The map produced by the application of 60A was used for the remaining operations. The map was normalized to a maximum of 1 and then scaled by the magnitude of the intercept to produce an intercept map. The intercept map accounts for signal loss due to inexact timing of the pulse sequences, and imperfect rephasing. The intercept map was subtracted from the 60A map, and then result was divided by 60 (the applied current) to produce an efficiency map.

5.2.6 Imaging

The gel-liquid phantom was imaged with the insert gradient driven at 20 A, 40 A, and 90 A, during diffusion-weighting in a spin-echo pulse sequence (TR / TE/ BW = 10000 ms / 49.8 ms / 1953.12 Hz per pixel). The parameters of the pulse sequence were identical to those already discussed, and the diffusion weighting was performed with two 7 ms pulses separated by 14.7 ms. Figures 5.10 and 5.11 illustrate how the efficiency maps are used to calculate the b-value at each point for a given pulse sequence.

5.2.6.1 Alignment

The first step was to appropriately position the previously calculated efficiency map for the insert. To do this the location of peak gradient must be pinpointed in the newly-aquired images. The information from the whole-body gradient diffusion-weighted sequence (b=100) was used to produce a ADC map. This ADC map is combined with the insert-gradient-diffusion-weighted current and sequence timing
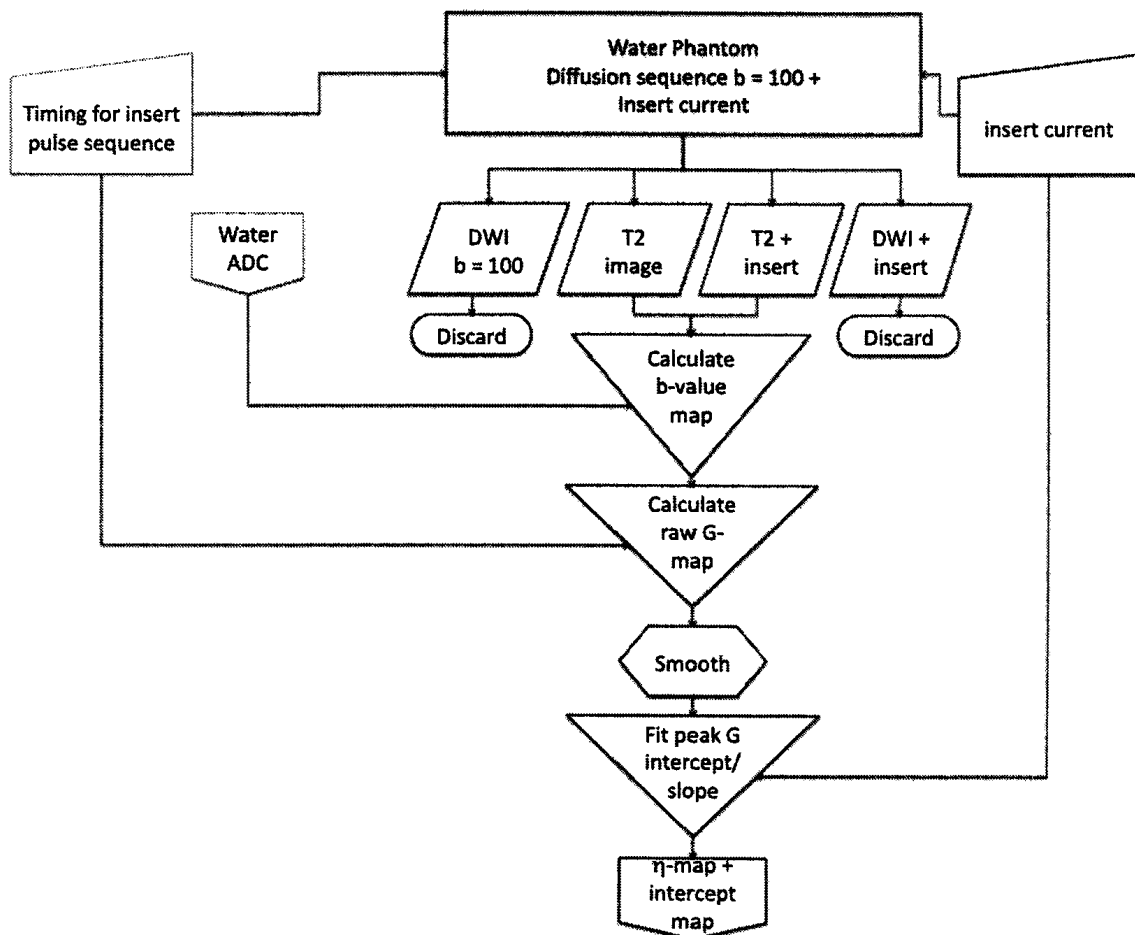
Fig. 5.9: Calculation of gradient efficiency. Using a spin-echo pulse sequence T2 and diffusion-weighted images were collected for the timing corresponding to b = 100. A map of the b-values was constructed assuming the ADC for water collected previously. The map of the b-values was converted into a map of the gradient strength using the sequence timing parameters. The map was smoothed and an efficiency map was calculated by subtracting the intercept from each gradient map and dividing by the applied current.
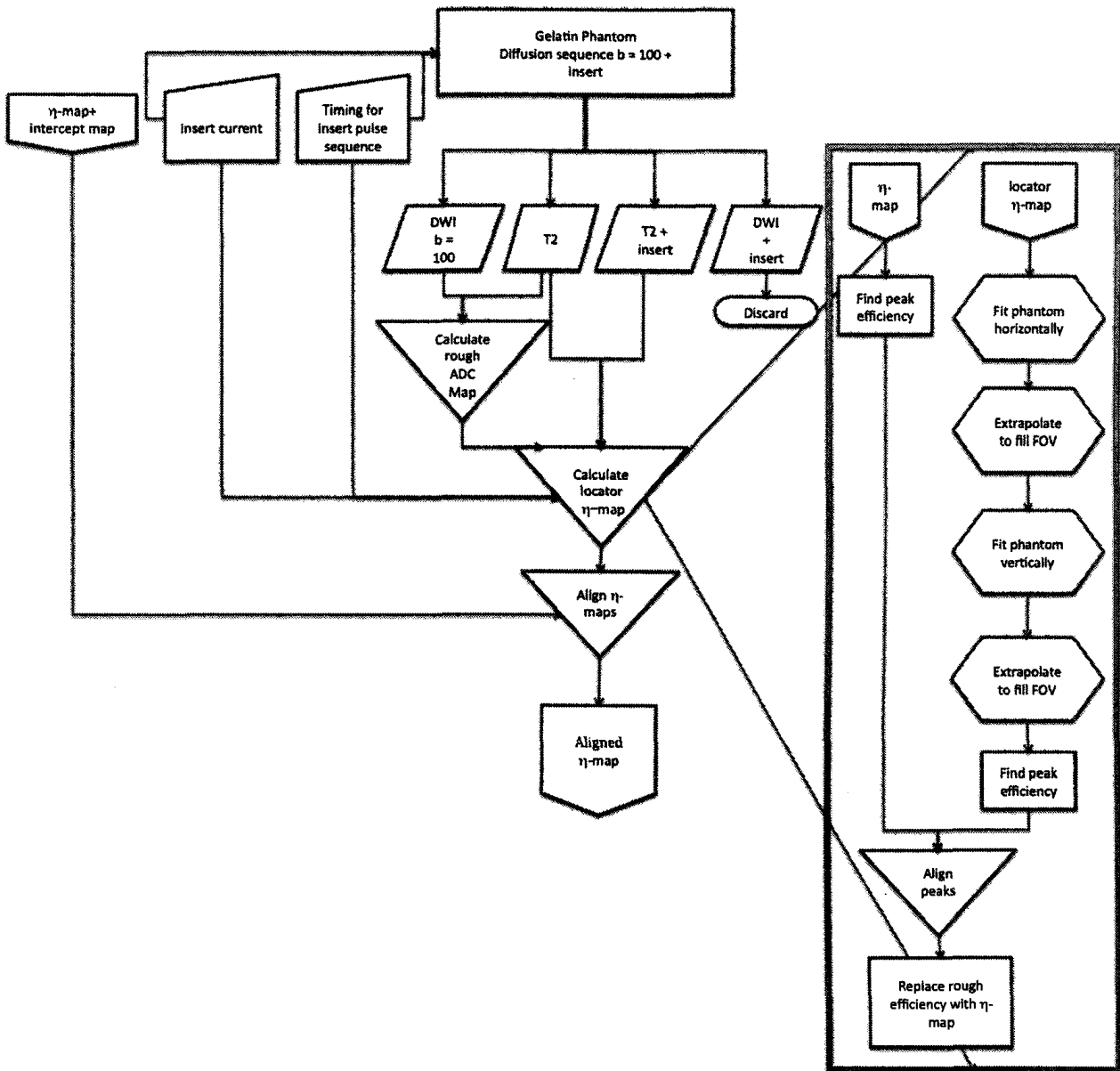
Fig. 5.10: Alignment of efficiency map. The location of the peak efficiency was determined by fitting the efficiencies (calculated from the b=100 whole-body-diffusion sequence and the insert-gradient diffusion image) with a second order polynomial. The peak was then aligned with the location maximum efficiency in the previously calculated efficiency maps.

parameters to produce a gradient map. Although this gradient map represents the effect of the insert on the image, it could only serve as a locator map due to the poor approximation of gelatin ACD that was obtained from the b=100 whole-body-gradient sequence. The peak point of the locator map was identified by fitting a second order polynomial horizontally and vertically to the efficiency, and then aligning the peak of the locator map with the peak of the previously calculated efficiency map for the insert.

5.2.6.2 ADC calculation: measured and simulated efficiency maps

Using the aligned efficiency map, intercept map, and pulse sequence timing parameters, a map of the b-values across the image was calculated. This was combined with the T2 and diffusion weighted images obtained using the insert to calculate the ADCs for the phantom. From the diffusion-weighted image the signal intensity in both the water and gelatin signal were obtained from a 440 pixel region of interest. The standard deviation of the noise level from an adjacent 440 pixel region was also aquired. This information was used to calculate the SNR for the images.

This process of determining the ADC was repeated a second time. However in the repetition, the efficiency maps calculated from the simulated gradient coil were substituted for the efficiency map determined from the experiment.

5.3   Results

5.3.1   Physical design

The insert gradient was designed to have a mutual inductance of 80 μH and a resistance of 9.9 mΩ. The electrical properties of the constructed coil were slightly different. At 1 kHz, the measured inductance was 83$\pm$5 μH, and the resistance was 17$\pm$3 mΩ.
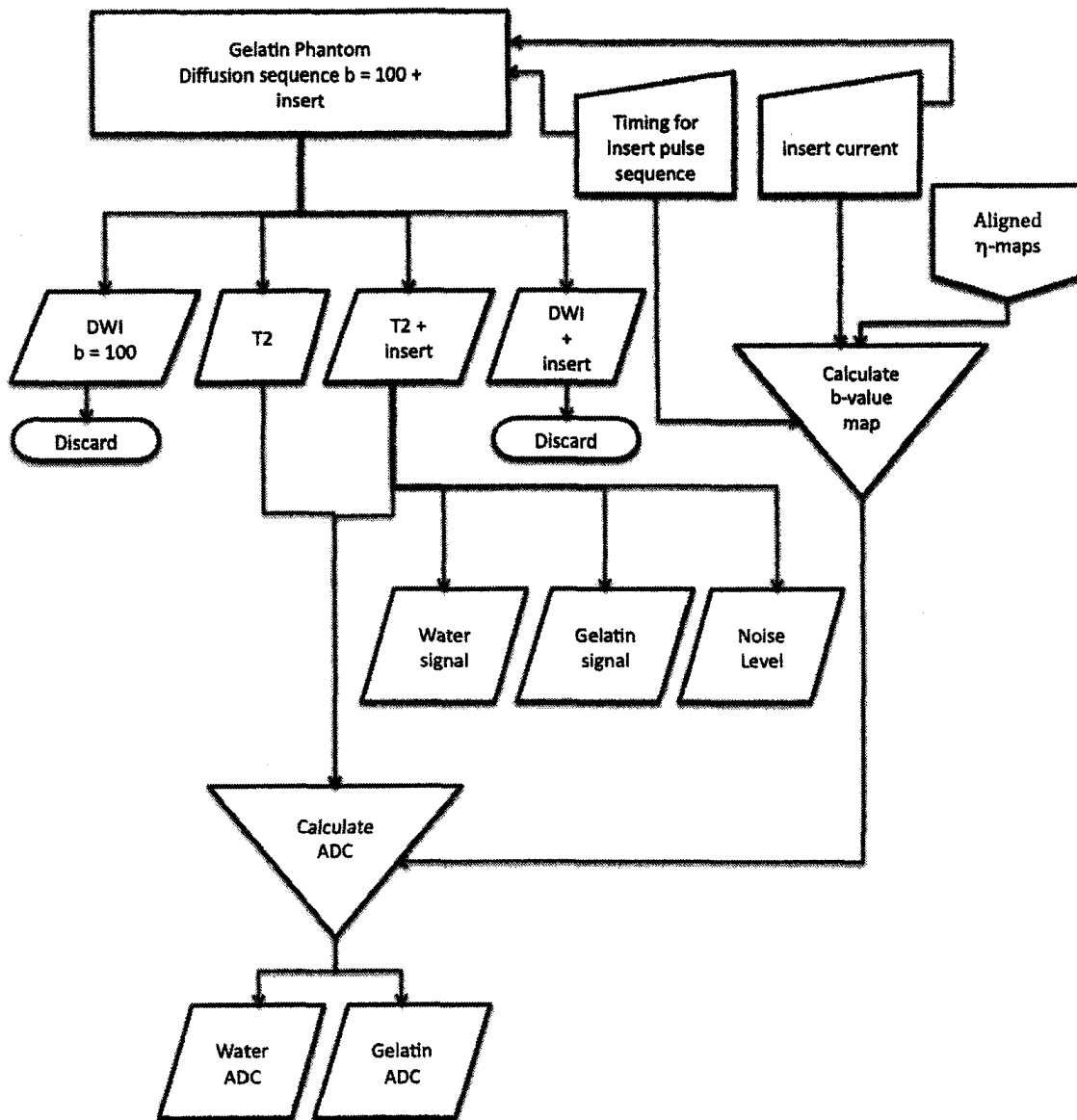
Fig. 5.11: Calculation of ADC using gradient insert. A map of the b-values is calculated from the sequence timing parameters and the aligned efficiency maps. The b-value map is combined with the T2 and gradient-insert diffusion weighted images to determine the ADC for the water and gelatin components of the phantom.
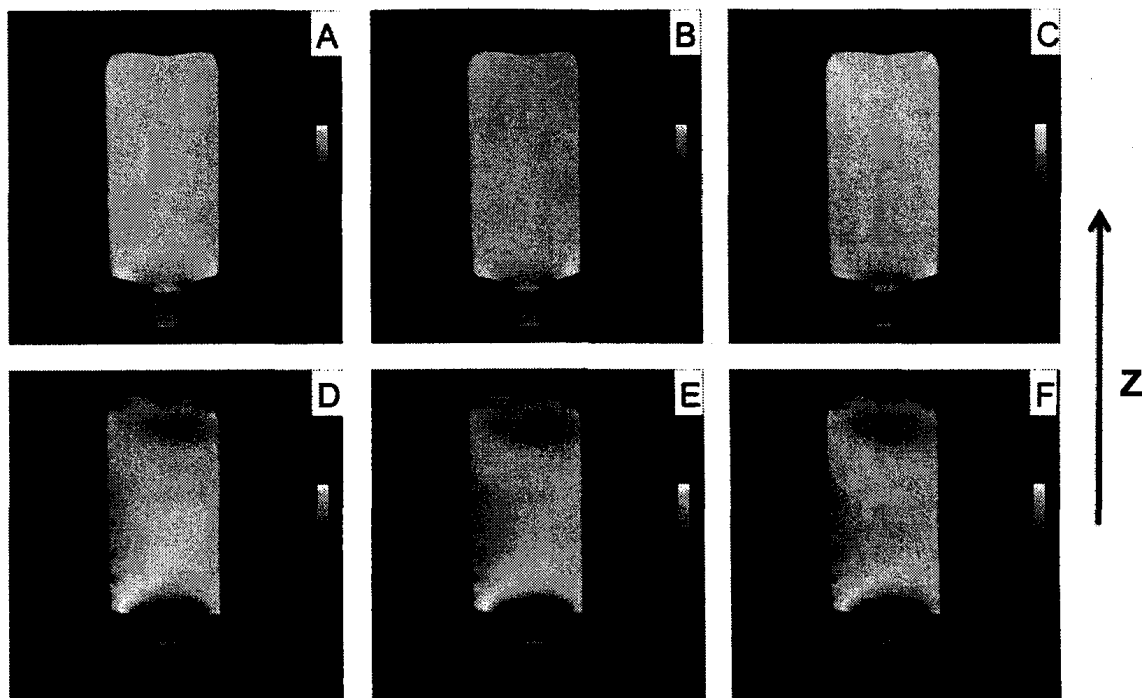
Fig. 5.12: A GRE image obtained with the unpowered gradient insert. Images (A), (B), and (C) were obtained at 122.109 Hz/pixel. Images (D), (E) and (F) were obtained at 15.625 Hz/pixel. (A) and (D) were obtained with the gradient attached to the amplifier and the amplifier energized. (B) and (E) were obtained with the gradient attached to the amplifier, and the amplifier not-energized. (C) and (F) were obtained with and open circuit. Frequency-encode direction is along the x-axis.

5.3.2 Testing

The results of imaging with the gradient insert in the bore, but not powered, are illustrated in Figure 5.12. The top row shows the images obtained at a relatively high bandwidth (122.109 Hz/pixel) and the images on the bottom are obtained at a relatively low bandwidth (15.625 Hz/pixel). Each column represents a different circuit configuration for the insert. In the first column the gradient was attached to an energized amplifier that was held at 0 A. In the second column the gradient was attached to an un-energized amplifier and in the third column the detached gradient was an open circuit.
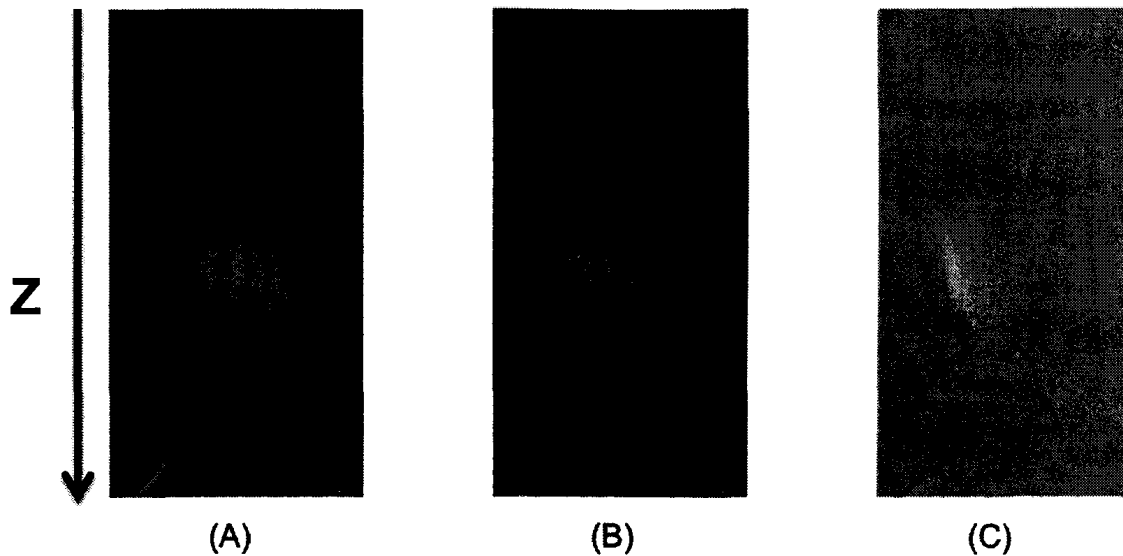
Fig. 5.13: (A) Magnitude of diffusion-weighted image with 40 A driving current. (B) Magnitude of diffusion-weighted image with -40A driving current and complementary cable configuration. (C) Difference image of A-B (C). Frequency-encode direction is along the x-axis.

Figure 5.13 shows the result of flipping the cables and inverting the amplitude of the current during the pulse sequence. The image in 5.13a and b are a homogenous phantom imaged with the cables driving the coil at 40 A and -40 A (with the cables connected in a complementary configuration). Figure 5.13c is the difference between Figures 5.13a and Figures 5.13b. The existence of a difference between 5.13a and 5.13b indicated inconsistencies in the system driving the insert that should be reduced in order to limit de-phasing and loss of the MR signal.

5.3.3   Preparation

Figure 5.14 shows the images of the water/gelatin phantom taken using conventional diffusion-weighted imaging with a whole body gradient. The first column is the T2 weighted image taken with increasing TE's. The second column is the image with diffusion-weighting (increasing b-values). The final column is a map of the apparent diffusion coefficient obtained using a pixel-by-pixel ratio of the images in the first two

Weighting	Phantom			
	Water ADC $[\times 10^{-4} mm^2/s]$	Water SNR	Gelatin ADC $[\times 10^{-4} mm^2/s]$	Gelatin SNR
b = 100	22.9±5.5 (0.30)	12.4	11±19 (1.1)	4.85
b = 200	21.3±3.3 (0.18)	10.3	15±13 (0.73)	3.7
b = 500	20.4±2.2 (0.12)	5.4	11.6±5.5 (0.30)	2.4
b =1000	18.3±2.1 (0.11)	2.6	5.9±2.9 (0.16)	2.0
b = 2000	10.3±1.0 (0.053)	1.9	2.4±1.5 (0.082)	1.9

Table 5.1: The apparent diffusion coefficient measured using the whole-body gradient only, for each region of the liquid/gel phantom at b = 100, 200, 500, 1000, and 2000 s/mm^2 ADC's are quoted as the mean ± standard deviation (standard error).

columns and prior knowledge of the b-values.

The diffusion coefficients and standard deviation for the phantom, imaged with the whole-body gradients only, are shown in Table 5.1 for a range of b-values. At b= 100 s/mm^2 the apparent diffusion coefficient (ADC) of water was 22.9± 5.5 $\times 10^{-4} mm^2/s$. This varied somewhat as the b-value of the pulse sequence changed. Similarly, the apparent diffusion coefficients for the gelatin part of the phantom are also shown in the table (11.6± 5.5 $\times 10^{-4} mm^2/s$ at b = 500 s/mm^2). Literature values place the self-diffusion coefficient for pure water at room temperature at 22 $\times 10^{-4} mm^2/s$ [16]

The top row of Figure 5.15 shows the diffusion image of the homogeneous phantom imaged with a pulsed current of 0 A, 22.25A, 30A, 40A, and 60A. The second row represents a map of the b-values, based on the apparent diffusion coefficient for the water at b=100 s/mm^2 from Table 5.1, with the curve across the image smoothed and filtered to remove high frequency noise by convolution with a gaussian kernel. At 22.25 A (pulsed at a δ of 7 ms and a Δ of 14.7 ms) the b-values were calculated from the experiment to range from 10 to 125 s/mm^2 across the image; at 30 A, the b-values were determined to range from 12 to 250 s/mm^2; at 40 A the b-values were found to range from 19 to 380 s/mm^2; finally, the 60A b-values were found to range
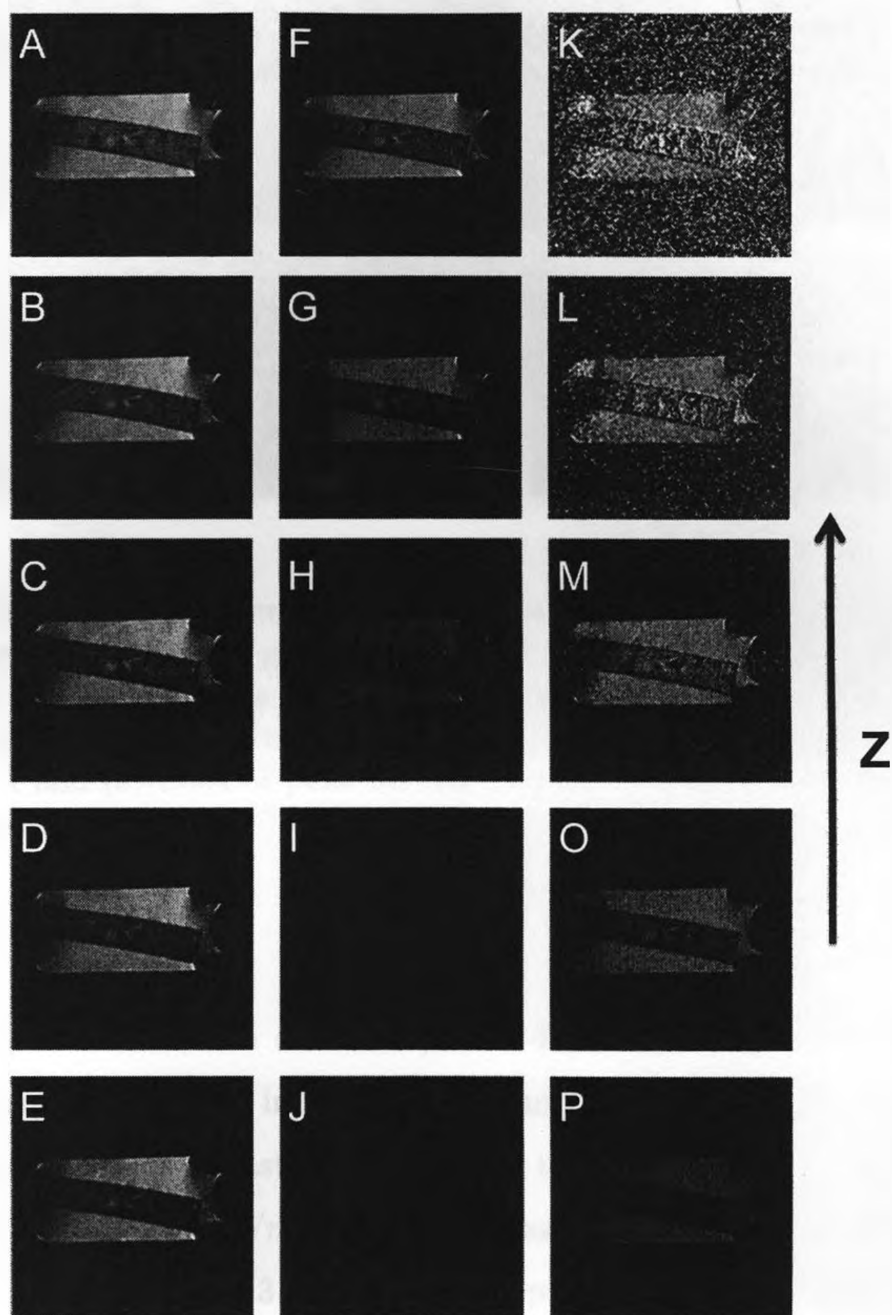
Fig. 5.14: (A-E) represent M_1, the non-diffusion-weighted images obtained in the first application of the sequence. From (A) to (E) the sequence TE's are 49.8, 55.2, 64.8, 74.4, and 86.5 ms. (F-J) represent M_2, the diffusion-weighted images obtained in the second application of the sequence. From (F) to (J) the sequence b-values are 100, 200, 500, 1000, and 2000 s/mm^2. (K-O) represents the apparent diffusion coefficient maps representing the result of the operation $log(\frac{M_1}{M_2})/b$. The images in this figure were obtained using only the whole-body gradients. Frequency-encode direction is along the x-axis.
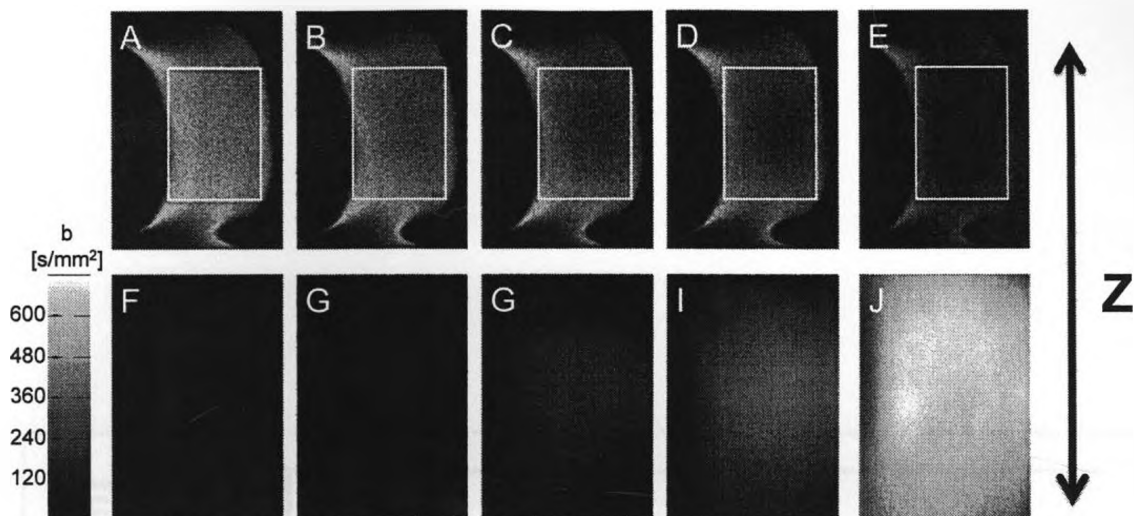
Fig. 5.15: The top row represents the diffusion weighted image of the homogeneous phantom taken with an insert gradient pulsed at (A) 0 A, (B) 22.25A, (C) 30A, (D) 40A, and (E) 60A. The b-value map in the second row was developed by smoothing and filtering the pixel-by-pixel calculation of the b-value for (F) 0 A, (G) 22.5 A, (H) 30 A, (I) 40 A and (J) 60 A of peak driving current. Frequency-encode direction is along the x-axis.

from 19 to 621 s/mm^2.

The peak gradient for each of 22.25A, 30A, 40A, and 60A was calculated from the b-value maps and plotted in a graph in Figure 5.16. The line through the data points represents the linear-least-squares fit, and the slope represents a peak gradient efficiency of 5.30 ± 0.59 $mT/m/A$, which is close to the peak simulated gradient efficiency of 5.67 mT/m/A at 3 cm. The intercept of the graph is 111± 24 mT/m

5.3.3.1 Imaging using insert gradients

Finally, Figure 5.17 shows the apparent diffusion coefficients of the gelatin/water phantom collected using the insert gradient, and processed with the b-value maps obtained using the homogenous phantom.
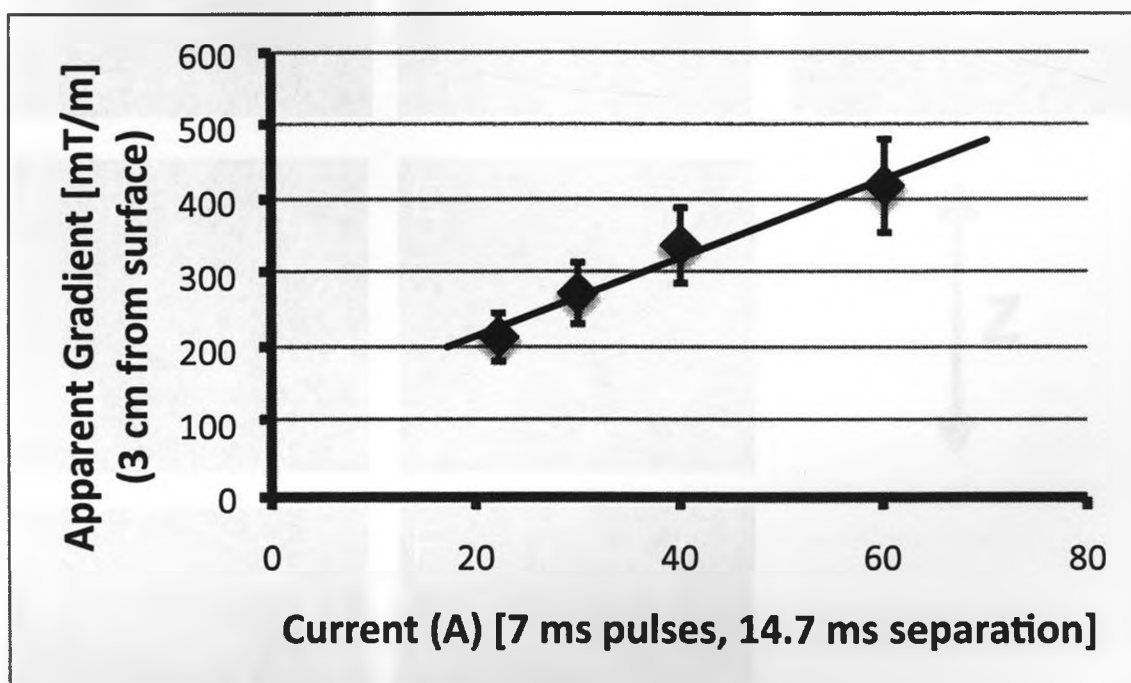
Fig. 5.16: The peak gradient strengths calculated from the b-value maps when the current is driven at 22.250A, 30A, 40A, and 60A. The slope of the fitted curve is $5.30 \pm 0.59\ mT/m/A$, the intercept is $111\pm 24\ mT/m$. Error bars are the standard deviation of the gradient values of 25 surrounding pixels
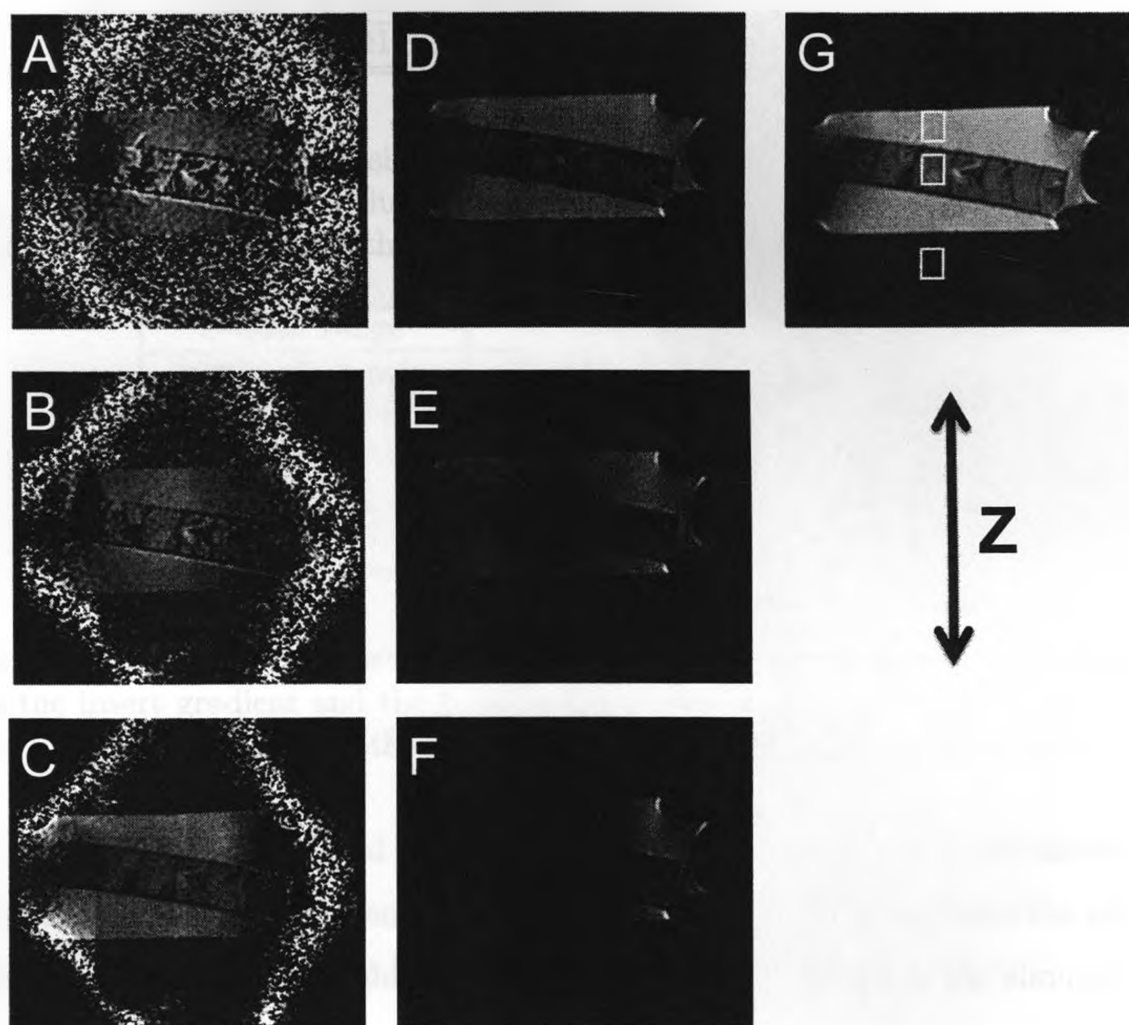
Fig. 5.17: ADC of liquid/gel phantom collected with an insert gradient producing b-values of (A) 52-99, (B)145-307, (C) 581-1332. (D), (E), and (F) are the corresponding images weighted with the diffusion-insert. (G) is the non-diffusion weighted image of for TE=49.8 ms. The white boxes represent the region where noise was measured in the diffusion image, and the region where the signal was measured for both the gelatin and the water. Frequency encoding was in the z-direction

b-value range		Phantom			
b min	b max	Water ADC	Water	Gelatin ADC	Gelatin
$[s/mm^2]$	$[s/mm^2]$	$[\times 10^{-4} mm^2/s]$	SNR	$[\times 10^{-4} mm^2/s]$	SNR
52	99	23.6±10(.55)	10.2	20.9 ±35(1.9)	3.6
145	307	25.1±8.0(.44)	4.5	13.6±12(.65)	2.4
581	1332	21.8±5.2(.29)	1.4	10.5±6.2(.34)	1.3

Table 5.2: The apparent diffusion coefficient measured in the liquid/gelatin phantom using the insert gradient. Values are quoted as the mean ± the standard deviation (standard error). SNR is for the diffusion-weighted image.

b-value range		Phantom	
b min	b max	Water ADC	Gelatin ADC
$[s/mm^2]$	$[s/mm^2]$	$[\times 10^{-4} mm^2/s]$	$[\times 10^{-4} mm^2/s]$
49.2	83	41.7±8.03(.43)	20.7±36(1.9)
152	255	29.9±2.85(.15)	15.3±11(.60)
658	1104	26.0±4.3(.24)	12.4±4.8(.26)

Table 5.3: The apparent diffusion coefficient measured in the liquid/gelatin phantom using the insert gradient and the b-value map simulated from the assumed gradient design. Values are quoted as the mean ± the standard deviation (standard error)

From the diffusion-weighted images the signal to noise ratios were calculated and the apparent diffusion coefficients were determined for both the water and the gelatin. These values are listed in Table 5.2. The ADC's calculated using the simulated b-values are listed in Table 5.3.

5.4 Discussion

5.4.1 Physical Construction

The self-inductance of the butterfly coil insert matched the simulated self-inductance, to within the errors of the measurement. However, the resistance of the constructed magnet was greater than simulated. This discrepancy was because of the electrical

connections that were required in a practical implementation that were not included in the simulation. The coil had a low initial resistance and even the minimal addition of leads and connectors significantly increase the resistance of the system.

5.4.2 Testing

The GRE imaging of the water phantom resting on top of an unpowered gradient insert demonstrated the lack of significant susceptibility differences introduced by the insert alone. This first test showed that the mere presence of the insert gradient did not significantly distort the image.

Ideally, the direction of the cable connection should not make a difference in image acquisition. However, the difference image taken during the system calibrations show that some anomalies existed. This indicated either a bias in the amplification system, or that induced currents were producing unwanted gradients during the imaging process.

Significant distortion did occur during diffusion-weighted imaging both with and without power to the gradient insert, as is evidenced in Figures 5.13, 5.14, and 5.17. The curvature in the frequency encode direction was common to the pulse sequence done both with and without the presence of the gradient insert in the bore. Further investigation into the pulse sequence is needed to correct this image distortion.

5.4.3 Apparent diffusion coefficient: whole body gradients

The diffusion coefficients of the phantom changed depending on the b-value used to measure it using the full-body gradients. The true self-diffusion coefficient of water can be obtained using other methods and is known [16]. As was shown in Table 5.1, in MRI the pulse sequence parameters can affect the ADC for water as reported from a diffusion-weighted image. For tissue a wide range of ADCs are reported in

MRI literature [17]. Often discrepancies come about as increased diffusion time allows molecules more of a chance to encounter walls, structures, or other barriers to diffusion and decrease the measured ADC as the time allowed for diffusion increases.

The calculated ADC may also decrease due to the non-zero noise floor of an MR image. From Figure 5.14 it can be seen that as the b-value increases the signal in the diffusion-weighted image decreases. The apparent diffusion coefficients are calculated by taking a ratio of the T2-weighted image (numerator) to the diffusion-weighted image (denominator). As the b-value increases, the signal from the diffusion-weighted image should decrease and approach zero. In practice the mean of the denominator approaches the mean of the noise of the image, which is something greater than zero. This results in a decrease in the calculated diffusion-coefficient as the SNR of the diffusion-weighted image degrades.

Another confounding issue in calculating ADC values is the possibility for imprecision in the applied pulse sequence. Any mis-match in the two lobes of the gradient can cause dephasing in static molecules that is not completely rephased in the second diffusion pulse. An error here would result in a perceived increase in the apparent diffusion coefficient across all elements of the image. However, in this case we see an initial value of ADC in water which is very close to that of literature, at b=100, followed by a decrease in ADC with longer b-values. So imprecise diffusion-lobe rephasing is unlikely to be the reason for the multiple values in the ADC measurement using the whole-body gradients.

5.4.4 Insert gradient efficiency

The b-value produced by the pulse sequence for a range of input currents was measured for the homogeneous phantom. Based on a pulse sequence with a TE (49.8 ms), gradient strengths were calculated from these b-values. The peak of gradient

strength calculations for each input current were plotted on a linear graph that was fit with both a slope and an intercept. The slope represents the gradient efficiency. The non-zero intercept was unexpected and required some explanation.

We hypothesize that this error is due to a mis-match in the diffusion-weighted pulses. The waveform generator driving the insert gradient had a maximum time resolution of 4 μs, the amplifiers were capable of currents of up to 210A, and the peak efficiency of the simulated coil of 5.67 mT/m/A.

If over $\Delta t = .004ms$ on one lobe of the diffusion-pulse a gradient of $G = 5.6[mT/m/A] \times 20[A] = 112mT/m$ was mis-applied across a single pixel $r = 1.6[mm]$ then the change in magnetic field B across the pixel would be:

$$
\begin{aligned}
\Delta B &= G \times r \\
&= 112[mT/m] \times 0.0016[m] \\
&= 0.18[mT].
\end{aligned}
\tag{5.4}
$$

The applied gradient would result in a maximum signal dephasing of:

$$
\begin{aligned}
\phi &= \gamma \Delta B \Delta t \\
&= 2\pi \times 42.577[kHz/mT] \times 0.18[mT/m] \times 0.004[ms] \\
&= 0.1918[rad].
\end{aligned}
\tag{5.5}
$$

The signal dephasing would appear as a loss in signal magnitude $S_{mismatch}$.

$$S_{mismatch} = \int_{-\phi/2}^{\phi/2} \frac{cos(\theta)}{\phi} d\theta \tag{5.6}$$

$$= \frac{sin(\phi/2)}{\phi/2}$$

$$= \frac{sin(0.1918/2)}{0.1918/2}$$

$$= 0.9985$$

This represents a 0.2% signal loss for every image acquisition. If the real gradient efficiency was $\eta = 5.7mT/m/A$ and a current of 20 A was applied to the gradient insert, then the expected gradient strength ($G_{calculated}$) would be:

$$G_{calculated} = \eta \times I \tag{5.7}$$

$$= 5.6[mT/m/A] \times 22.00[A]$$

$$= 112[mT/m].$$

Assuming a $\Delta = 14[ms]$ and a $\delta = 5[ms]$. This would result in a b-value of:

$$b_{calc} = \gamma^2 G_{calculated}^2 \delta^2 (\Delta - \delta/3) \tag{5.8}$$

$$= 6.99.[s/mm^2]$$

Given an apparent diffusion coefficient of $D = 22.9 \times 10^{-4} mm^2/s$ this would result in a signal reduction in the diffusion-weighted image of:

$$S_{diffusion} = e^{-b_{calc}D} \tag{5.9}$$

$$= \quad e^{-6.99 \times 22.9 \times 10^{-4}}$$

$$= \quad 0.9841.$$

However, because there is also signal loss due to the mis-matched gradient lobes, this results in a total signal reduction during diffusion-weighted imaging of:

$$
\begin{aligned}
S_{total} &= S_{mismatch} S_{diffusion} && (5.10) \\
&= 0.9841 \times 0.9985 \\
&= 0.9826.
\end{aligned}
$$

During image analysis, all signal loss was interpreted as if it had come from diffusion, thus the b-value from the experiment (b_{exp}) would be:

$$
\begin{aligned}
b_{exp} &= \frac{-ln(S_{total})}{D} && (5.11) \\
&= 7.66[s/mm^2].
\end{aligned}
$$

From the experiment b-value, an apparent gradient G_{exp} would be:

$$
\begin{aligned}
G_{exp} &= (\frac{b_{exp}}{\gamma^2} \delta^2 (\Delta - \delta/3))^{(1/2)} && (5.12) \\
&= 117[mT/m].
\end{aligned}
$$

The difference G_{diff} between the calculated gradient and the actual gradient, given 20 A of applied current would then be:

$$
G_{diff} = G_{exp} - G_{calculated} \qquad (5.13)
$$

$$= 5.2[mT/m].$$

If we found the apparent gradients for a range of driving currents, we would get a G_{diff} of 5.2 mT/m at 20.0A, 2.7 mT/m at 40A, 1.8 mT/m at 60A, and 1.3 mT/m at 80A. A linear-least-squares fit applied to the calculated gradients would result in a decreased slope (5.54 $mT/m/A$) and an intercept of $5.90mT/m$.

If the timing error on the pulse, in practice, were larger than 4 μs then the intercept would increase. For example, a timing error of 20 μs would result in an intercept of $108mT/m$. This analysis suggests an explanation for the intercept in Figure 5.16. It also suggest that future refinements of this would would include a waveform generator capable of higher-resolution timing adjustments. Because G_{diff} decreases with applied current, if this mismatch is the source of the error, then the ADC at higher b-values (higher gradient strengths), obtained with the gradient insert, may be more accurate than those obtained at low b-values (and low driving currents) when using the insert.

5.4.5 Diffusion-weighted imaging with the insert

Using the insert, we were able to image the non-homogenous phantoms at b-values that ranged from 100 -1300 s/mm^2 while maintaining the relatively short TE obtained at b = 100 for the whole body coil. The pulse duration required of the gradient inserts was less than 10 ms and the separation was less than 15 ms. The ADC showed some shift in the measured diffusion coefficient, the largest being in the measurement of the gelatin diffusion coefficient at low currents. In that case the precision of the measurement was poor, and the selection of a different region -farther from the centre of the b-value map, would have resulted in a more accurate diffusion coefficient for the gelatin. As the maximum current in the gradient insert increased, the precision of the calculated ADC measurement increase and a b-value range of 581-1332 the standard

deviation over a region of gelatin was six times less than the standard deviation for that same area at b = 52-99. The improved precision in the ADC's that were obtained at high b-values would permit differentiation between sets of tissues with similar ADCs.

5.5 Conclusion

The operation of the insert gradient at b-values greater than 200 allows for good SNR in the image when compared to diffusion-weighted images obtained by the whole-body gradients alone. Traditionally this could be parlayed into fewer averages (faster imaging). There are some complications due to pulse sequence timings for the insert gradient, and the pulse sequence needs to be carefully examined to eliminate image distortion.

A b-value range of 581-1332 can be obtained using the insert gradient with a signal to noise improvement over traditional diffusion weighted imaging. This improvement promises improved diffusion-weighted imaging with an improved SNR which might be translated into a reduced number of image averages. The inclusion of an insert for diffusion-weighted imaging will permit a finer differentiation of diffusion contrast within an image and will allow us to examine more closely how the ADC changes with the time allowed for diffusion.

References

[1] Clarke SE; Hammond RR; Mitchell JR; Rutt BK. Quantitative assessment of carotid plaque composition using multicontrast mri and registered histology. *Magn Reson Med*, 50(6):1199–1208, 2003.

[2] Miller KL; Hargreaves BA; Gold GE; Pauly JM. Steady–state diffusion-weighted imaging of in vivo knee cartilage. *Magn Reson Med*, 51(2):394–398, 2004.

[3] McNab JA; Jbabdi S; Deoni SC; Douaud G; Behrens TEJ; Miller KL. High resolution diffusion-weighted imaging in fixed human brain using diffusion-weighted steady state free precession. *Neuroimage*, 46(3):775–785, 2009.

[4] Andersson JLR; Skare S. A model-based method for retrospective correction of geometric distortions in diffusion-weighted epi. *NeuroImage*, 16:177–199, 2002.

[5] Thoeny HC; De Keyzer F; Oyen RH. Diffusion-weighted mr imaging of kidneys in healthy volunteers and patients with parenchymal disease:initial experience. *Radiology*, 235:911–917, 2005.

[6] Brogiloli D; Vailati A. Diffusive mass transfer by nonequilibrium fluctuations: Fick's law revisited. *Physical Review E*, 63:1–4, 2001.

[7] Bammer R. Basic principles of diffusion-weighted imaging. *European Journal of Radiology*, 45(3):169–184, 2003.

[8] Carr HY; Purcell EM. Effects of diffusion on free precession in nuclear magnetic resonance experiments. *Phys Rev*, 94(3):630–8, 1954.

[9] Zhang B; Yen YF; Chronik BA; McKinnon GC; Schaefer DJ; Rutt BK. Peripheral nerve stimulation properties of head and body gradient coils of different sizes. *Magnetic Resonance in Medicine*, 50(50-58), 2003.

[10] Chronik BA; Rutt BK. A comparison between human magnetostimulation thresholds in whole-body and head/neck gradient coils. *Magnetic Resonance in Medicine*, 46:386–394, 2001.

[11] Feldman RE; Hardy CJ; Aksel B; Schenck J; Chronik BA. Experimental determination of human peripheral nerve stimulation thresholds in a 3-axis planar gradient system. *Magn Reson Med*, 62(3):763–770, 2009.

[12] Haacke EM; Brown RW; Thompson MR; Venkatesan R. *Magnetic Resonance Imaging: Physical Principals and Sequence Design*. Wiley-Liss, 1999.

[13] Vaughan T; DelaBarre L; Snyder C; Tian J; Akgun C; Shrivastava D; Liu W; Olson C; Adriany G; Strupp J; Andersen P; Gopinath A; van de Moortele PF; Garwood M; Ugurbil K. 9.4t human mri: preliminary results. *Magn Reson Med*, 56(6):1274–1282, 2006.

[14] Machann J; Schlemmer HP; Schick F. Technical challenges and opportunities of whole-body magnetic resonance imaging at 3t. *Phys Med.*, 24(2):63–70, 2008.

[15] Alford JK; Rutt BK; Scholl TJ; Handler WB; Chronik BA. Delta relaxation enhanced mr: Improving activation-specificity of molecular probes through r1 dispersion imaging. *Magnetic Resonance in Medicine*, 61(4):796–802, 2009.

[16] Woolf LA; Harris KR. Pressure and temperature dependence of the self-diffusion coefficient of water and oxygen-18 water. *Journal of the Chemical Society, Faraday Transactions 1: Physical Chemistry in Condensed Phases*, (76):377–385, 1980.

[17] Thoeny HC; De Keyzer F; Boesch C; Hermans R;. Diffusion-weighted imaging of the parotid gland: Influence of the choice of b-values on the apparent diffusion coefficient value. *Journal of Magnetic Resonance Imaging*, 20(5):786–790, 2004.

Chapter 6

Thesis Summary and Future Work

6.1 Thesis Summary

This thesis has detailed the design, evaluation, and integration of a localized gradient coil in diffusion-weighted contrast magnetic resonance imaging, as well as investigated the electrical and nerve stimulation characteristics of gradient systems.

Rapidly switched gradient coils induce electric fields during magnetic resonance imaging. Those electric fields were simulated using a finite-difference algorithm [1] and the Visible Man Model [2]. The variability in the simulation was evaluated by altering the model's resolution, relative size, and position.

The most important parameter for the simulation was model resolution. Without a minimum of 3-mm isotropic resolution, fine detail in the sinuses and other air passages was lost. From scaling the size of the model, it was possible to see the variation in the magnitude of peak due to some geometry alterations. This improved the estimation of error in the nerve rheobase values calculated from the electric field calculations.

In order to perform rheobase calculations, both the experimentally determined magneto-stimulation thresholds and the exact wire pattern of the gradient need to be known. This information is available for the head/neck customized and a full-body gradient. The wire pattern for a planar system with a limited field of view was also known, and so peripheral nerve stimulation experiments were performed. These experiments showed that, when compared to either the full-body gradient set, or a localized gradient designed for the head and neck region, the planar gradient system could operate stronger gradients, and switch between maximum and minimum gradient strengths more rapidly without causing stimulation.

The electric fields induced in the Visible Man model were simulated and compared to the stimulation thresholds, and locations of stimulation reported in the experiment, and the nerve rheobase and chronaxie times were calculated. These values were similar, but not identical to, the nerve rheobase and chronaxie times calculated for the head/neck gradient system.

The high stimulation thresholds in this planar experiment suggested higher gradient strengths might be achieved by building small, localized, gradient systems. The planer geometry of the gradient system also indicated that the design space for these localized gradients was not required to be cylindrical, as many full body gradient systems are.

Five design spaces were investigated, for five different coil geometries, a cylindrical fingerprint coil, a coil wound on a half cylinder, a four loop x-flat coil, a three-loop z-flat coil, and a butterfly coil. Each of the design spaces was investigated for both resistive and inductive merit. Given eventual fabrication constraints, a limit on the inductance was more of a restriction than resistance considerations. All optimal gradient designs, for both inductive and resistive merit, reached inductance limits (or in one case wire-spacing limits) prior to reaching resistance limits. Of the non-cylindrical designs, the butterfly coil produced the strongest gradients. The largest

area of linear gradient was produced by the planar designs.

A butterfly coil was built and powered as a fourth axis during diffusion weighted imaging. This gradient was driven separately using Techron amplifiers and was controlled by LabView on a Toshiba laptop. The diffusion pulses were applied prior to an spin-echo imaging sequence. After confirming the b-values attainable using the coil, diffusion-weighted images were produced with the coil. Using the fourth axis gradient coil, diffusion-images weighted with a b-values of 100-1000 s/mm^2 were achieved in a time frame that permitted b-values of only 100 s/mm^2 using standard full body gradients. The signal to noise ratio of the image showed an improvement of nearly 100%.

6.2   Future Work

Many sections of the work in this thesis presented opportunities for future research.

6.2.1   Simulation work with additional models

Several additional human models now exist in sufficient resolution to provide useful simulation data. Repeating the simulations with female and child sized models may provide insight into the pattern of stimulation and promote the predictive value of the simulations.

The most important information for the electric field simulation is the location of the air cavities. Theoretically, it might be possible to pair stimulation nerve threshold experiments with a high-resolution, full body MRI image. If the MRI image could be segmented into conductive and non-conductive regions, a paired simulation/experiment analysis could be done.

6.2.2 Peripheral nerve stimulation experiments

Several geometries were introduced in the consideration of a localized gradient coil. While stimulation studies were performed on larger gradient and cylindrical systems, those same studies are more rare for the butterfly and half-cylindrical coils. Profiling the stimulation thresholds for these geometries, and comparing the thresholds to the simulated electric fields would be an important next step. These studies would provide information to aid in the prediction of PNS, and detail the operational limits on the gradient strengths and slew rates for these coils when used in diffusion-weighted imaging.

6.2.3 Imaging studies

The analysis in Chapter 5 indicates that improved timing resolution might produced better diffusion-weighted images. Upgrading the technology driving the current amplifiers may produce significant improvements in analysis of apparent diffusion coefficients with the insert gradient.

Clarke et.al. [3] demonstrated atherosclerotic plaque segmentation using multi-contrast MRI images. The diffusion-weighted contrast was important for identifying necrotic tissue and calcification. A diffusion-only gradient could be used in a multi-contrast protocol to shorten the time required for the diffusion-weighting. It would be important to demonstrate that the diffusion-gradient-coil did not adversely affect the SNR of the T_1- and T_2- weighted images.

The incorporation and control of an extra gradient into MRI systems is currently awkward and requires manipulation of two control stations, a console for the MRI system and a separately triggered instrument to control the fourth gradients pulse sequence. Currently, there exist multiple channels for RF signals; given the improvements in imaging possible with localized gradients, it is not inconceivable that future

iterations of MRI system designs will allow for the possibility of an inclusion of 4, independently driven, gradient coils.

References

[1] Press WH; Teukolsky SA; Vetterling SA; Flannery BP. *Numerical Recipes in C++: The Art of Scientific Computing Numerical Recipes in C++: The Art of Scientific Computing Numerical Recipes in C++: The Art of Scientific Computing Numerical Recipes in C++: The Art of Scientific Computing.* Cambridge University Press, 2002.

[2] MI Ackerman. Viewpoint: The visible human project. *Journal of Biocommunication*, 18(2):14, 1991.

[3] Clarke SE; Hammond RR; Mitchell JR; Rutt BK. Quantitative assessment of carotid plaque composition using multicontrast mri and registered histology. *Magn Reson Med*, 50(6):1199–1208, 2003.

Appendix A

Electric Field Simulation

The electric field calculations presented in this work employed a finite difference method implemented in C++ [1]. The gradient wire patterns were represented as a series of discrete current elements. Each element was represented by a set of Cartesian co-ordinates (x, y, z) and a vector describing the length $(\vec{dl})$ of the element along each of the three orthogonal axis (dx, dy, dz). This information completely specified the length, location, and direction of current flow for the source point.

The calculation of vector potential $(\vec{A})$ was performed through an implementation of Equation A.1 which is a discretisation of the integral defining vector potential in Equation A.2.

$$\vec{A}(x, y, z, t) = \frac{\mu}{4\pi} \int_{i=1}^{n} \frac{\vec{dl_i}}{|R_i|} dV' \tag{A.1}$$

$$\vec{A}(x, y, z, t) = \frac{\mu}{4\pi} \sum_V \frac{\vec{J}'(x', y', z', t')}{R_1} dV' \tag{A.2}$$

In Equation A.1, $R_i^2 = (x - x_i)^2 + (y - y_i)^2 + (z - z_i)^2$, and n is the number of current elements approximating the wire pattern.

Decomposing a gradient waveform into its Fourier spectrum, the constituent wavelengths of the signal through the wire are much longer than the length of individual gradient coil windings, so one can consider the applied current to be the same in every current element without consideration of transmission line effects. Therefore, the electric field due to vector potential ($\vec{E}_A$) can be found by multiplying the result of Equation A.1 with the applied current slew rate (dI/dt) as demonstrated in Equation A.3.

$$\vec{E}_A(x, y, z, t) = -\frac{dI(t)}{dt} \vec{A}(x, y, z) \tag{A.3}$$

The electric field at each point in space for a three dimensional solution was calculated by looping through all of the current elements and summing each elements contribution to the total field.

The scalar potential was calculated by approximating tissue as conducting material, classifying air as a homogenous non-conducting material, and solving Laplaces equation at every field point in the solution space. Lapaces equation was expressed in the algorithm by the discretized form of Equation A.4. The algorithm adjusted the value of I_n in order to minimize the residual ($resid$). Through numerous iterations the residual was eventually reduced to 0 for all field points, thus satisfying Laplace's equation.

$$resid = \Phi_{i-1} + \Phi_{j-1} + \Phi_{k-1} + \Phi_{i+1} + \Phi_{j+1} + \Phi_{k+1} - 6\Phi_n \tag{A.4}$$

In Equation A.4, In represents the nth-voxel under evaluation at position (i, j, k) and Φ_{i+1}, Φ_{i-I}, Φ_{j+1}, Φ_{j-I}, Φ_{k+1}, Φ_{k-I} represent the scalar potential in the neighboring voxels along the x-, y-, and z-axes. The minimization is accomplished by an iterative relaxation method. The value of the vector potential Φ_n assigned to each voxel is such that Equation A.4 has a residual value of 0. This, in turn, affects the residual

of the surrounding voxels. Each point is considered sequentially and adjusted to set the residual to 0. On the next iteration it is corrected to account for the effect of the voxels evaluated after it in the cycle. The simulation is considered to have converged on a solution when the magnitude of the adjustment across the entire image that was required to set the residuals of Equation A.4 to 0 was less than a threshold.

At a boundary (a tissue voxel which was adjacent to at least one air voxel), the calculation of the residual was performed with Equation A.5. This represented a discretization of the boundary condition for this system Equation A.6.

$$resid = \sum_{n=1}^{3} \hat{N}(n) X \Delta \vec{I}(n) - \vec{H}(n) \qquad (A.5)$$

$$\frac{d\Phi}{d\hat{n}} = \hat{n} \cdot \vec{E}_A \qquad (A.6)$$

$\hat{N}(n)$ in Equation A.5 is the unit vector representing the normal to the boundary described in Equation A.7.

$$\hat{N}(n) = [N_i(n), N_j(n), N_k(n)]^{-1} \qquad (A.7)$$

$\Delta \vec{I}(n)$ represents the gradient of scalar potential across the boundary and is given by Equation A.8.

$$\Delta \vec{I}(n) = [I_{i\pm1} - I_n, I_{j\pm1} - I_n, I_{k\pm1} - I_n] \qquad (A.8)$$

$\vec{H}$ was the component of the electric field perpendicular to the boundary expressed in Equation A.9.

$$\vec{H}(n) = ([E_{ai}(n), E_{aj}(n), E_{ak}(n)] \cdot \hat{N}(n)) \times \hat{N}(n) \qquad (A.9)$$

Convergence was accelerated during early iterations by using the Equation A.10.

$$\Phi_n(it+1) = \Phi_n(it) - \Omega(it) \cdot \frac{resid}{6} \qquad \text{(A.10)}$$

In Equation A.10,$\Omega(it)$ was an acceleration factor for the it_{th}" iteration. $\Omega(it)$ amplified the correction made to In early in the process so that the residual is not adjusted to precisely 0. This means that early iterations were over-corrected, but as the number of iterations increased, the size of the correction was rapidly decreased and the solution converged more quickly.

The magnitude of the adjustment required for each point was summed over the entire data set and compared against a threshold. If the total required correction was greater than the threshold, the algorithm was iterated again. Eventually, the adjustments fell below the threshold, and the scalar potential profile was considered converged.

The iterative approach to determining scalar potential depended on being able to correctly set the boundary conditions for each voxel on the surface of the conducting object. To identify these boundaries the representation of the model was simplified so that each voxel tissue type, T_n was assigned a value of 0 (for air or non-conducting material) or 1(for tissue or conducting material). To evaluate boundary status Equation A.11 was used.

$$status = 6T_n - (T_{i+1} + T_{i-1} + T_{j+1} + T_{j-1} + T_{k+1} + T_{k-1}) \qquad \text{(A.11)}$$

If the status was positive, then the voxel represented a tissue voxel on a tissue-air boundary, otherwise the voxel represented either air, or a homogenous section of tissue.

The normal to the **surface at a point was** estimated by averaging the 28 cross products calculated **from the vectors formed** between that point on the surface and the eight nearest surface **voxels. Each** cross product was multiplied by -1 if needed to ensure that it pointed **from the inside** to the outside of the object. The resulting average vector was **normalized to a magnitude** of 1.

References

[1] Press WH; Teukolsky SA; Vetterling SA; Flannery BP. *Numerical Recipes in C++: The Art of Scientific Computing Numerical Recipes in C++: The Art of Scientific Computing Numerical Recipes in C++: The Art of Scientific Computing Numerical Recipes in C++: The Art of Scientific Computing.* Cambridge University Press, 2002.

Appendix B

Permissions for Chapter 3